1-1-2010

Synthesis of Complex Plasmonic Nanostructures for Applications in Surface-Enhanced Raman Spectroscopy and Biomedicine

Claire Cobley
Washington University in St. Louis

WASHINGTON UNIVERSITY IN ST. LOUIS

School of Engineering
Department of Biomedical Engineering

Dissertation Examination Committee:
Younan Xia, Chair
Donald Elbert
Lihong Wang
Barani Raman
Da-Ren Chen
Yinjie Tang

SYNTHESIS OF COMPLEX PLASMONIC NANOSTRUCTURES FOR APPLICATIONS IN SURFACE-ENHANCED RAMAN SPECTROSCOPY AND BIOMEDICINE

By

Claire Margaret Cobley

A dissertation presented to the
Graduate School of Arts and Sciences
of Washington University in
partial fulfillment of the
requirements for the degree
of Doctor of Philosophy

December 2010

Saint Louis, Missouri

ABSTRACT OF THE DISSERTATION

Synthesis of Complex Plasmonic Nanostructures for Applications in Surface-Enhanced Raman Spectroscopy and Biomedicine

by

Claire Margaret Cobley

Doctor of Philosophy in Biomedical Engineering

Washington University in St. Louis, 2010

Professor Younan Xia, Chairperson

This research centers around techniques to engineer the properties of noble-metal nanostructures for applications in surface-enhanced Raman spectroscopy (SERS) and biomedicine. Many of these potential applications are made possible by the strong localized surface plasmon resonance (LSPR) of noble-metal nanostructures, which is heavily influenced by the particle's morphology.

The first part of this work focuses on the solution-phase synthesis of Ag nanostructures. In this section, I demonstrate the synthesis of Ag nanostructures with two different morphologies that are interesting for fundamental SERS studies: anisotropically truncated octahedrons and large, single-crystalline spheres. In both syntheses, control over etching was critical to morphological control.

The second part of this work discusses galvanic replacement reactions, which can be used to create a variety of hollow, porous nanostructures whose LSPR can be tuned into the near infrared region, a spectral range particularly interesting for biomedical

applications due to reduced light attenuation in soft tissue. In this section, I will describe how the nanostructures resulting from galvanic replacement reactions can be engineered by controlling the morphology of the Ag nanostructures used as templates or the metal salt(s) titrated during the reaction. Specifically, I will discuss how the use of template particles with non-uniform surfaces influences the final morphology and how the progression of a galvanic replacement reaction using two different precursors (e.g. $HAuCl_4$ and Na_2PdCl_4) depends strongly on the order that they are added.

In the final part of this work, I will discuss the biocompatibility of Au-Ag nanocages with different compositions and surface coatings and their use in two biomedical imaging techniques: as contrast agents in photoacoustic mapping of sentinel lymph nodes and as novel three-photon luminescence probes for *in vitro* imaging.

ACKNOWLEDGMENTS

First of all, I would like to thank my advisor, Professor Younan Xia for all his guidance and support. In particular, I'd like to thank him for many helpful discussions about research, for continually encouraging me to improve my work, and all the opportunities to share it with the scientific community. I would also like to express my appreciation to Dr. Dong Qin for her advice and support, and for all her work to develop a Nano Research Facility here at Washington University that played a key role in many of my experiments.

I have also been fortunate to have excellent collaborators and am grateful to them for making this interdisciplinary work possible: Matt Rycenga for SERS measurements, Fei Zhou and Professor Zhi-Yuan Li at the Institute of Physics, Chinese Academy of Sciences for DDA calculations, Dr. Kwang Hyun Song and Professor Lihong Wang for photoacoustic imaging, and Ling Tong and Professor Ji-Xin Cheng at Purdue University for multi-photon luminescence measurements and imaging.

Special thanks go to Dr. Leslie Au for teaching me cell culture, Dr. Pedro Camargo for teaching me how to use the HRTEM, and the numerous other former and current Xia group members who have provided me with suggestions, thought-provoking conversations, and friendship. In particular, Dr. Sara Skrabalak and Dr. Jingyi Chen have given me valuable mentorship and advice over the years – thank you.

I would also like to express my gratitude to all those who have inspired me along the path that led me to graduate school. In particular, I would like to thank Gray Rushin, my high school teacher who first introduced me to the world of chemistry and showed me

how exciting science could be.

Finally, I would like to express my deep thanks to my family, who have encouraged and supported me throughout all my academic endeavors. Thank you for everything. To Jordi Heijman – thank you for your never-ending patience, support, and love.

TABLE OF CONTENTS

LIST OF FIGURES

LIST OF TABLES

LIST OF ABBREVIATIONS

1,4-BDT	1,4-benzenedithiol
MTT	3-(4,5-dimethylthiazol-2-yl)-2,5-diphenyl tetrazolium bromide
σ_a	absorption cross section
ATO	asymmetrically truncated octahedron
DDA	discrete dipole approximation
E	electric field amplitude
EDAX	energy-dispersive X-ray spectroscopy
EF	enhancement factor
fcc	face-centered cubic
FFT	fast-fourier transform
HRTEM	high-resolution transmission electron microscopy
ICP-MS	inductively-coupled plasma mass spectrometry
LSPR	localized surface plasmon resonance
mPEG	methoxyl poly(ethylene glycol)
NIR	near-infrared
OCT	optical coherence tomography
PAT	photoacoustic tomography
PVP	poly(vinyl pyrrolidone)
SEM	scanning electron microscopy
SAM	self-assembled monolayer
SERS	surface-enhanced Raman spectroscopy
RES	reticuloendothelial system
3PL	three-photon luminescence
TEM	transmission electron microscopy
TNF	tumor necrosis factor-alpha
2PL	two-photon luminescence
UV-Vis	ultra violet-visible

Chapter 1

Introduction

Even before the beginning of recorded history, people have sought to engineer the properties of materials to better meet the challenges of their time. While great advances have been made in the past through the manipulation of bulk materials, in recent years the engineer's toolset has been greatly expanded through increasingly powerful techniques to manipulate and study materials on the nanoscale. This new direction of research has been deemed "nanotechnology", and generally refers to the study of materials with at least one dimension between 1-100 nm. Nanomaterials have been found to have a number of interesting and useful properties that are either novel or greatly enhanced when compared to their bulk counterparts.[1-3] Due to the great diversity of materials that can be engineered on the nanoscale, the mechanisms behind their size-dependent properties are also variable, and the study of nanomaterials has consequently led to new insights about the fundamental properties of materials.[1-3]

A number of the interesting phenomena observed with nanomaterials center around their interactions with light.[1-3] In particular, metal nanostructures exhibit a phenomenon known as localized surface plasmon resonance (LSPR), which is the origin of the bright colors that made their use in artistic endeavors common long before their scientific properties were understood.[2] When a metal nanostructure encounters

electromagnetic radiation of an appropriate wavelength, the delocalized conduction electrons of the metal will begin to oscillate collectively (relative to the lattice of positive nuclei) in resonance with the frequency of the incident light. Figure 1.1 illustrates this phenomenon for a metal nanosphere, which is smaller than the wavelength of light. This LSPR response can be divided into two types of interactions: scattering, in which the incident light is re-radiated at the same wavelength in all directions; and absorption, in which the light is transferred into vibrations of the lattice (i.e., phonons), typically observed as heat. Together, these processes are referred to as extinction (extinction = absorption + scattering). Typically, the relative contributions of these optical processes and the overall extinction cross section can be calculated using either Mie theory or the discrete-dipole approximation (DDA), as they will vary greatly for different structures.[4,5] Mie theory was developed by Gustav Mie in 1908 to explain the optical properties of Au nanospheres, and provides exact solutions by directly solving Maxwell's equations.[4] However, the equations used in this technique are limited to spheres, spheroids, shells, and infinite cylinders. Alternatively, the DDA method can be used to approximate the optical properties of any structure, as it models a nanostructure as an array of polarizable points, which interact with both incoming light and each other.[5] Both have been used with great success to predict the optical properties of plasmonic nanostructures.

In order to maximize the optical response of metal nanostructures for a particular application, it is important to both match the resonant wavelength of the nanostructure with the light source and ensure that the maximum amount of incoming light reaches the site of interest. For this reason, engineers have developed techniques to create plasmonic

nanostructures with specific LSPR resonances. The resonant wavelength of a plasmonic nanostructure depends on a number of variables, particularly the size, shape, and morphology of the nanostructure, as well as the dielectric environment.[2,6,7] Consequently, controlling the morphology of metal nanostructures is a powerful means for maneuvering the LSPR response. Even small changes in aspect ratio or corner sharpness can have a large impact.[6] The morphological dependence of LSPR-based properties also extends beyond simple changes in the wavelength of maximum light extinction. In addition to the strong absorption and scattering described above, LSPR results in strong electric near-fields close to the surface of the nanostructure, which also depend strongly on the specific morphology.[8] Nanostructures with sharp features have been shown to generate extremely concentrated electric fields in the regions of high curvature (e.g., the sharp corners of a cube), which can enhance spectroscopic signals from molecules located in these regions.[8,9]

While both lithographic and solution-phase techniques have been used to generate plasmonic nanostructures, solution-phase methods (i.e. the growth of nanostructures from atoms or seed crystals) have emerged as a more promising method for the large-scale production of plasmonic nanostructures.[10] In addition to the greater scalability, solution-phase methods also make it possible to study the optical properties of nanostructures in solution, as their LSPR response can be different from those on a substrate due to particle-substrate interactions.[11] The shape or morphology of metal nanostructures produced in the solution phase can be tuned by modifying the reaction conditions such as the temperature, capping agent, and the concentration of trace ions. By controlling such

relatively simple parameters, a wide variety of morphologies have been demonstrated, with a correspondingly broad range of LSPR resonances.[10]

These strong, tunable optical properties have made plasmonic nanomaterials interesting for a wide variety of biomedical applications.[12] The first general area where plasmonic nanostructures have had an impact is in sensing applications.[13-16] For example, the sensitivity of LSPR to changes in dielectric environment and aggregation has been harnessed to fabricate colorimetric sensors. A classic application of this method is the detection of a target DNA strand by conjugating Au nanospheres with the complimentary oligonucleotide.[17] When the target strand is present, the Au nanospheres will aggregate, resulting in a dramatic color change from red to blue due to coupling between the plasmons of the individual particles. Plasmonic nanostructures can also be used to enhance spectroscopic techniques, which has been demonstrated with great success for Raman spectroscopy.[18-21] In Raman spectroscopy, the amount of signal generated depends on the strength of the electromagnetic field surrounding the molecules by a factor of E^4. For this reason, if the molecule of interest is located in one of the strong electric near-fields close to the surface of an excited plasmonic nanostructure, the signal will be enhanced by many orders of magnitude – enhancement factors of 10^{14} have been reported.[20,21] This technique is known as surface-enhanced Raman spectroscopy (SERS), and has been used to detect biologically relevant molecules such as glucose and prostate specific antigen.[22,23] Due to the morphological and wavelength dependence of the LSPR near-fields, controlled synthesis of plasmonic nanostructures (particularly those of Ag) has been critical to advances in this field.

Plasmonic nanostructures have also been investigated as therapeutic and imaging agents, however for such applications the requirement that a significant amount of light is able to reach the nanostructures provides an additional challenge as blood and tissue absorb and scatter the majority of light over much of the visible spectrum.[24] However, in the near-infrared region (NIR, 650-900 nm) a window exists where light can penetrate more deeply into tissue.[24] For this reason, much research has focused on how the LSPR response of plasmonic nanostructures can be tuned to these wavelengths.[25] A typical Au nanosphere has a LSPR wavelength around 520 nm. By changing the size it is possible to shift this peak slightly, but to red-shift the peak further to the NIR region it is necessary to synthesize new morphologies with more tunable plasmonic properties. Three general strategies have been used to shift the LSPR peak into the NIR region:[25] *i*) elongating spherical nanoparticles into nanorods to generate tunable longitudinal modes,[26] *ii*) coating the surfaces of dielectric colloidal spheres with conformal shells of the desired metal,[27,28] and *iii*) empting out the interiors of nanoparticles to form hollow nanoboxes, nanocages, and nanoshells with voids in the center.[29-31]

Of these three strategies, in my work I have focused on the third due to the fact that hollow structures can be easily produced with a variety of sizes, the interior void can be used for drug delivery, and LSPR tuning is synthetically simple through the use of a galvanic replacement reaction.[29] Figure 1.2 shows how the LSPR wavelength can be tuned across the visible spectrum and into the NIR when ~40 nm Ag nanocubes are titrated with different amounts of $HAuCl_4$ in water. Due to the different electrochemical potentials between these two metals, Ag^+ ions are dissolved while Au atoms are plated on

the surface of the initial Ag nanocube as more $HAuCl_4$ is titrated into the system.[31] This leads to an increasingly hollow structure, which correlates with a red-shift in the LSPR resonance due to hybridization between the plasmons of the inner and outer surfaces.[32] This interaction is analogous to the combining of two atomic orbitals in molecular orbital theory, and generates a symmetric ("bonding") plasmon and an anti-symmetric ("anti-bonding") plasmon.[33] The symmetric plasmon with a lower energy interacts with the incident light, and determines the location of the LSPR peak. As the wall thickness of a nanostructure is reduced, the interaction between the two surface plasmons increases, resulting in increased splitting between the symmetric and anti-symmetric plasmons. This lowers the energy of the symmetric plasmon, resulting in a red-shift of the LSPR. Through this mechanism, very small changes in wall thickness can have a significant effect on the optical properties, allowing for facile tuning of the LSPR peak into the NIR region.

The Au-Ag nanocages created using the galvanic replacement reaction described above have additional favorable properties for biomedical applications beyond their straightforward LSPR tuning. For example, Au-Ag nanocages also have high absorption and/or scattering cross sections, facile surface modification through Au-thiolate bonds, hollow interiors for drug loading, and tunable sizes.[29,34,35] For this reason, they have been investigated in a wide variety of applications including photothermal tumor destruction, drug delivery, multi-photon luminescence imaging, and sentinel lymph node mapping (with photoacoustic imaging).[29,35-39] The galvanic replacement reaction used to create gold nanocages is also very versatile, and by changing the template particles or precursor

used it is possible to generate a number of different of noble-metal structures with different morphologies and compositions, which can also be useful for catalytic applications.[12]

1.1. Scope of This Work

This work will be organized into three main sections: the shape-controlled synthesis of Ag nanostructures for SERS applications, the use of galvanic replacement to form alloyed nanostructures with tunable plasmonic properties, and the biomedical applications of Au-Ag nanocages.

Chapter 2 will discuss synthetic methods I developed to generate Ag nanostructures with *i*) asymmetric shapes and *ii*) perfectly spherical profiles, as well as their SERS properties. In the first section, I will discuss the synthesis of anisotropically-truncated octahedrons.[40] When a second aliquot of $AgNO_3$ was added to a polyol synthesis, Ag nanocubes evolved into this exotic shape due to oxidative etching and overgrowth. Three adjacent faces of the nanocube grew more rapidly than the other three faces, generating a non-centrosymmetric structure that is half truncated cube, half octahedron. Both oxidative etching and rapid addition of $AgNO_3$ solution played a critical role in the mechanism. The LSPR spectra of these unusual nanostructures displayed a new peak when compared to the cubic seeds. The overall SERS enhancement measured with these unusual nanostructures was roughly the same as that measured with Ag octahedra of a similar size, despite the non-centrosymmetric morphology.

I will also present a new method based on wet etching for the production of high quality, single-crystal Ag nanospheres.[41] By rapidly mixing a suspension of uniform Ag nanocubes with a small amount of ferric nitrate or ferricyanide-based etching solution, I could either truncate the sharp corners and edges to form rounded nanocubes, or etch further to obtain nanospheres without sharp features but with roughly the same diameter

as the original cubes. Notably, this technique could be used to produce uniform Ag nanospheres with a broad range of sizes and large enhancement factors, opening up new possibilities for fundamental studies of SERS, as previous synthetic methods were unable to produce uniform spheres larger than ~35 nm.

Chapter 3 will discuss how galvanic replacement can be used to transform solid metal nanostructures (such as those discussed in Chapter 2) into more complex materials with hollow morphologies and tunable properties.[12] After a brief introduction to the previously reported synthesis of Au-Ag nanocages from Ag nanocubes, I will discuss the use of more unusual Ag nanostructures -- asymmetrically truncated octahedrons and nanobars -- characterized by a non-uniform surface. Since the surfaces of these nanostructures contain facets with a variety of different areas, shapes, and atomic arrangements, I was able to examine the roles of these parameters in the different stages of the galvanic replacement reaction with Au precursors. I will also discuss the effect that different precursors can have on the galvanic replacement reaction by examining the results of titrating Ag nanocubes with Na_2PdCl_4 and $HAuCl_4$.[42] In particular, I will focus on the combined system, where I found that the order the two precursors were added influenced the morphology, the position of the LSPR resonance, the composition, and the catalytic abilities of the resulting hybrid nanocages.

Finally, Chapter 4 will discuss the use of Au-Ag nanocages for biomedical imaging applications. I will examine the biocompatibility of Au-Ag nanocages with different compositions and different surface coatings. Next, I will discuss the novel three-photon luminescence of Au-Ag nanocages, which originates from their alloy

structure and can be used to track their locations in *in vitro* environments and tissue slices.[38] Finally, I will discuss the use of Au-Ag nanocages as contrast agents for photoacoustic imaging of sentinel lymph nodes.[39] Due to their large absorption cross sections, Au-Ag nanocages in the sentinel lymph node could be detected 33 mm deep in soft tissue.

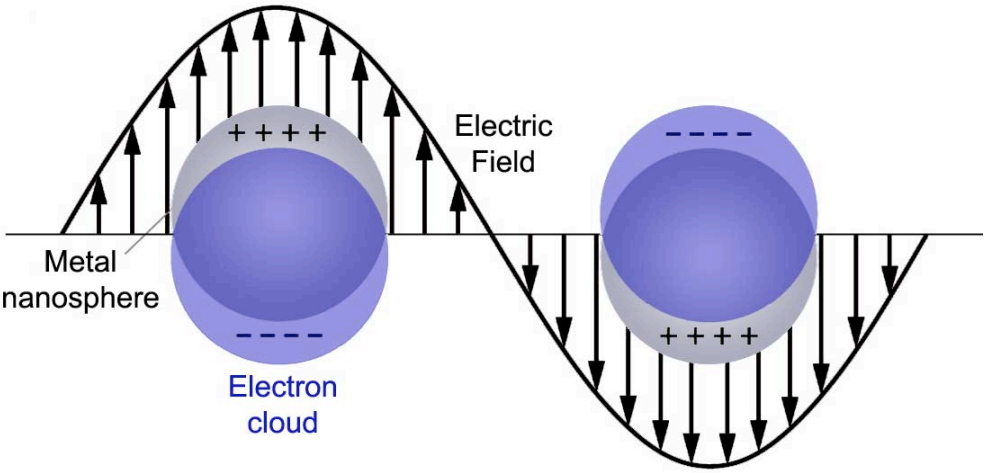

Figure 1.1. Schematic illustration of localized surface plasmon resonance (LSPR), showing the oscillation of delocalized electrons in the presence of an electromagnetic wave.

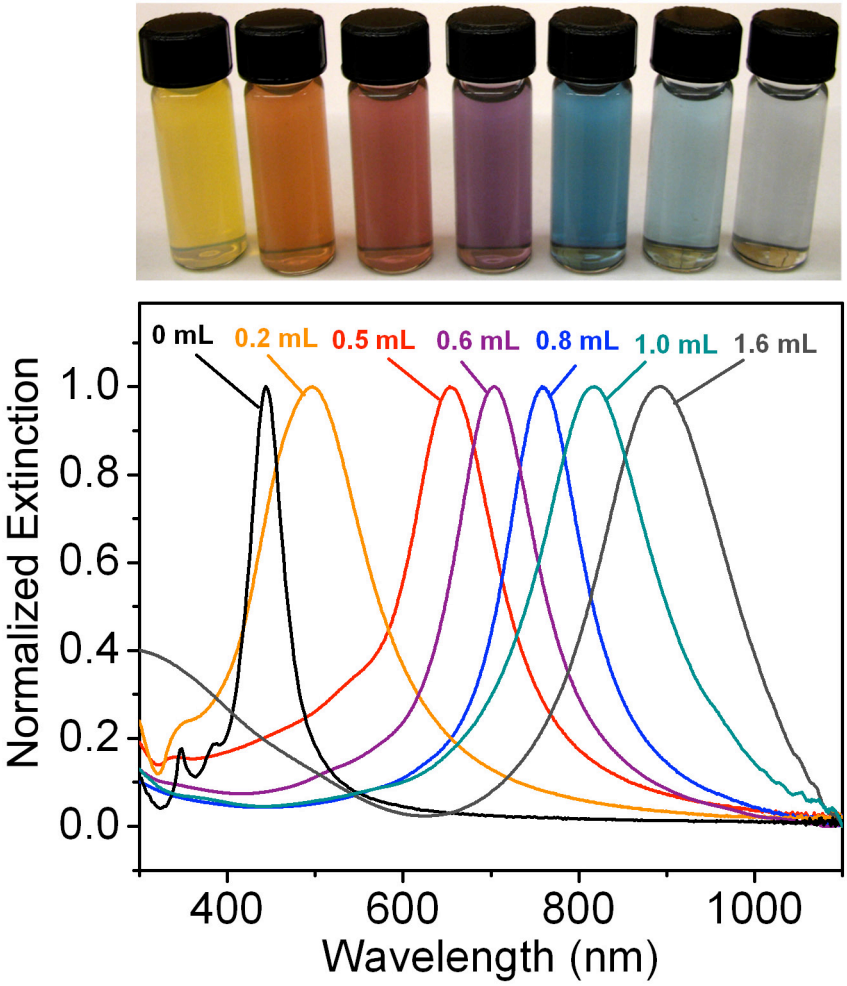

Figure 1.2. (Top panel) vials containing Au-Ag nanocages prepared by reacting 5 mL of a 0.2 nM Ag nanocube (edge length ~40 nm) suspension with different volumes of a 0.1 mM $HAuCl_4$ solution. (Lower panel) the corresponding UV-visible spectra of Ag nanocubes and Au-Ag nanocages.

1.2. References for Chapter 1

[1] Alivisatos, A. P. *Science* **1996**, *271*, 933.

[2] Kreibig, U.; Vollmer, M. *Optical Properties of Metal Clusters*; Springer: Berlin, 1995.

[3] Daniel, M.-C.; Astruc, D. *Chem. Rev.* **2004**, *104*, 293.

[4] Mie, G. *Anal. Phys.* **1908**, *25*, 376.

[5] Draine, B.; Flatau, P. *J. Opt. Soc. Am. B* **1994**, *11*, 1491.

[6] Kelly, K.; Coronado, E.; Zhao, L.; Schatz, G. C. *J. Phys. Chem. B* **2003**, *107*, 668.

[7] Wiley, B. J.; Im, S. H.; Li, Z.-Y.; McLellan, J. M.; Siekkinen, A. R.; Xia, Y. *J. Phys. Chem. B* **2006**, *110*, 15666.

[8] McLellan, J. M.; Li, Z.-Y.; Siekkinen, A. R.; Xia, Y. *Nano Lett.* **2007**, *7*, 1013.

[9] Schuller, J. A.; Barnard, E. S.; Cai, W.; Jun, Y. C.; White, J. S.; Brongersma, M. L. *Nat. Mater.* **2010**, *9*, 193.

[10] Xia, Y.; Xiong, Y.; Lim, B.; Skrabalak, S. E. *Angew. Chem. Int. Ed.* **2009**, *48*, 60.

[11] Sherry, L.; Chang, S.; Schatz, G. C.; Van Duyne, R. P.; Wiley, B. J.; Xia, Y. *Nano Lett.* **2005**, *5*, 2034.

[12] Cobley, C. M.; Xia, Y. *Mater. Sci. Eng., R* **2010**, *70*, 44-62.

[13] Rosi, N. L.; Mirkin, C. A. *Chem. Rev.* **2005**, *105*, 1547.

[14] Willets, K. A.; Van Duyne, R. P. *Ann. Rev. Phys. Chem.* **2007**, *58*, 267.

[15] Cao, Y. C.; Jin, R.; Mirkin, C. A. *Science* **2002**, *297*, 1536.

[16] Wilson, R. *Chem. Soc. Rev.* **2008**, *37*, 2028.

[17] Elghanian, R.; Storhoff, J. J.; Mucic, R. C.; Letsinger, R. L.; Mirkin, C. A. *Science* **1997**, *277*, 1078.

[18] Nie, S.; Emory, S. *Science* **1997**, *275*, 1102.

[19] Rycenga, M.; Camargo, P. H. C.; Li, W.; Moran, C. H.; Xia, Y. *J. Phys. Chem. Lett.* **2010**, *1*, 696.

[20] Haynes, C. L.; McFarland, A. D.; Van Duyne, R. P. *Anal. Chem.* **2005**, *77*, 338A.

[21] Qian, X.-M.; Nie, S. *Chem. Soc. Rev.* **2008**, *37*, 912.

[22] Haynes, C.; Yonzon, C.; Zhang, X.; Van Duyne, R. *J. Raman Spectrosc.* **2005**, *36*, 471.

[23] Grubisha, D. S.; Lipert, R. J.; Park, H.-Y.; Driskell, J.; Porter, M. D. *Anal. Chem.* **2003**, *75*, 5936.

[24] Weissleder, R. *Nat. Biotechnol.* **2001**, *19*, 316.

[25] Hu, M.; Chen, J.; Li, Z.-Y.; Au, L.; Hartland, G. V.; Li, X.; Marquez, M.; Xia, Y. *Chem. Soc. Rev.* **2006**, *35*, 1084.

[26] Murphy, C. J.; Sau, T. K.; Gole, A. M.; Orendorff, C. J.; Gao, J.; Gou, L.; Hunyadi, S. E.; Li, T. *J. Phys. Chem. B* **2005**, *109*, 13857.

[27] Oldenburg, S.; Averitt, R.; Westcott, S.; Halas, N. J. *Chem. Phys. Lett.* **1998**, *288*, 243.

[28] Rasch, M. R.; Sokolov, K. V.; Korgel, B. A. *Langmuir* **2009**, *25*, 11777.

[29] Skrabalak, S. E.; Chen, J.; Sun, Y.; Lu, X.; Au, L.; Cobley, C. M.; Xia, Y. *Acc. Chem. Res.* **2008**, *41*, 1587.

[30] Schwartzberg, A.; Olson, T.; Talley, C.; Zhang, J. *J. Phys. Chem. B* **2006**, *110*, 19935.

[31] Sun, Y.; Xia, Y. *J. Am. Chem. Soc.* **2004**, *126*, 3892.

[32] Prodan, E.; Radloff, C.; Halas, N. J.; Nordlander, P. *Science* **2003**, *302*, 419.

[33] Xia, Y.; Halas, N. *MRS Bull.* **2005**, *30*, 338.

[34] Chen, J.; Wang, D.; Xi, J.; Au, L.; Siekkinen, A.; Warsen, A.; Li, Z.-Y.; Zhang, H.; Xia, Y.; Li, X. *Nano Lett.* **2007**, *7*, 1318.

[35] Yavuz, M. S.; Cheng, Y.; Chen, J.; Cobley, C. M.; Zhang, Q.; Rycenga, M.; Xie, J.; Kim, C.; Song, K. H.; Schwartz, A. G.; Wang, L. V.; Xia, Y. *Nat. Mater.* **2009**, *8*, 935.

[36] Chen, J.; Glaus, C.; Laforest, R.; Zhang, Q.; Yang, M.; Gidding, M.; Welch, M. J.; Xia, Y. *Small* **2010**, *6*, 811.

[37] Au, L.; Zhang, Q.; Cobley, C. M.; Gidding, M.; Schwartz, A. G.; Chen, J.; Xia, Y. *ACS Nano* **2010**, *4*, 35.

[38] Tong, L.; Cobley, C. M.; Chen, J.; Xia, Y.; Cheng, J.-X. *Angew. Chem. Int. Ed.* **2010**, *49*, 3485.

[39] Song, K. H.; Kim, C.; Cobley, C. M.; Xia, Y.; Wang, L. V. *Nano Lett.* **2009**, *9*, 183.

[40] Cobley, C. M.; Rycenga, M.; Zhou, F.; Li, Z.-Y.; Xia, Y. *Angew. Chem. Int. Ed.* **2009**, *48*, 4824.

[41] Cobley, C. M.; Rycenga, M.; Zhou, F.; Li, Z.-Y.; Xia, Y. *J. Phys. Chem. C* **2009**, *113*, 16975.

[42] Cobley, C. M.; Campbell, D. J.; Xia, Y. *Adv. Mater.* **2008**, *20*, 748.

Chapter 2

Shape-Controlled Synthesis of Silver Nanostructures for Surface-Enhanced Raman Spectroscopy

2.1. Introduction

Silver nanostructures are of great interest in a number of disciplines because of their potential use as optical waveguides, near-field optical probes, chemical and biological sensors, and substrates for surface-enhanced Raman spectroscopy (SERS).[1-5] Both their use in and the enhancements that they may bring to these applications are made possible by the unique and tunable optical properties of metal nanostructures, in particular, their LSPR.[6] Silver is especially attractive for plasmonic applications due to its strong optical response, which can be an order of magnitude greater than what is possible with similar Au nanostructures for some applications.[7]

The LSPR of Ag nanostructures is characterized by their scattering and absorption of incident light (together referred to as extinction) at specific resonant wavelengths. The peaks that define the extinction spectrum of a particular nanostructure depend on a number of parameters, including the size, shape, and dielectric environment of the nanostructure.[6,8] Though changing the size of spherical Ag particles can induce small shifts in the LSPR peak position, in practice changing the shape of Ag nanostructures

provides more versatility.[6] As any change in the shape of the Ag nanostructure affects the pattern in which the free electrons are oscillating, the resonant frequency will also change.[6,7] The plasmonic response of Ag nanostructures will be the strongest when the LSPR is excited by the incident light under a resonant condition.[9] As a result, there is a strong desire to synthesize Ag nanostructures with specific morphologies to control their LSPR response.

In addition to far-field LSPR effects such as light scattering and absorption, strong near-fields are produced close to the surface of these structures.[6] These effects are particularly interesting because the enhanced electric field created around an optically excited metal nanostructure can drastically increase Raman signals of molecules near the surface, even enabling single molecule detection with some substrates.[5] This technique is known as SERS, and is one of the most interesting applications of Ag nanostructures.

Raman spectroscopy is a powerful technique that optically probes the vibrational levels of polarizable molecules, providing a unique Raman spectrum for each molecule.[10,11] Unfortunately, standard Raman spectroscopy gives very weak signals, limiting its applications. In SERS, however, the Raman signals of molecules close to the surface of a plasmonic nanostructure will be enhanced on the order of E^4 (where E is the electric field strength).[12] This high degree of enhancement enables much lower detection limits, and has made SERS a promising technique for the trace detection of important biomarkers such as glucose or prostate specific antigen.[13,14] While initial SERS studies with Ag nanostructures and nanostructured surfaces have demonstrated impressive signal enhancements, the irregularities in the substrates and the lack of reproducibility in the

measurements made it difficult to correlate the observed enhancements with specific geometries. In order to engineer SERS substrates to have extremely high enhancement factors, more controlled substrates and studies are required.

Control over the size and shape of Ag nanostructures can be achieved with lithographic methods; however, such techniques are of limited use because of their intrinsic drawbacks such as high costs, poor scalability, limited control in the z-direction and the polycrystallinity of metals deposited by physical or chemical means. On the other hand, solution-phase synthesis has proven to be a particularly robust method for producing large quantities of precisely controlled materials, and through careful tuning of synthetic parameters (e.g. temperature, surfactant, and concentration of trace ions) a wide variety of Ag nanostructures have been synthesized, including but not limited to wires, plates, cubes, bars, bipyramids, and octahedrons.[15,16]

Just as the morphology of an Ag nanostructure can have a large effect on the overall strength of near-fields, it can also have dramatic effects on the distribution of the electric fields close to the surface of the particle, and consequently the amount of SERS enhancement observed.[6,17] Figure 2.1 shows near-field distributions calculated with the discrete-dipole approximation (DDA) method for sharp Ag nanocubes and Ag nanospheres (note the different scale bars for each image).[17,18] It is clear from these calculations that the sharp corners of the nanocube create regions with strong electric fields. This phenomenon is sometimes known as the "lighting rod" effect and is closely related to the surface curvature of a nanostructure. This effect can be harnessed to concentrate light into nanosized volumes and dramatically increase the local field

intensity in these regions by up to 2000 times.[6]

The effect of sharp corners on SERS has been quantified experimentally by comparing the enhancement factors of sharp and truncated 90-nm Ag nanocubes for the detection of well-defined probe molecules adsorbed onto the surfaces of the particles (1,4-benzenedithiol, 1,4-BDT). At an excitation wavelength of 514 nm, the sharp Ag nanocubes had an enhancement factor of 1.26×10^5, while their truncated counterparts only had an enhancement factor of 7.45×10^4 (almost a 2x reduction).[17] These measurements were performed in the solution phase. SERS measurements can be performed either on nanostructures suspended in solution or on those deposited on substrates. While the presence of a substrate can change the optical properties of Ag nanostructures, requiring a more detailed analysis of SERS enhancements, it also makes it easier to study assemblies of nanostructures and laser polarization effects.[19,20,21]

Due to the strong morphological dependence of the LSPR response, a number of different Ag nanostructures have been investigated as SERS substrates including sharp and truncated cubes, bipyramids, and Au-Ag nanocages.[20,22,23] However, one fundamental Ag nanostructure that is notably lacking from this list is single-crystal spheres, due to the lack of a synthetic protocol for high-quality spheres with controllable sizes. Many procedures exist for the synthesis of polycrystalline quasi-spheres,[24,25] but these particles are not sufficiently well-defined to give accurate information in fundamental studies of the optical features that make Ag nanostructures so fascinating, as any sharp features can have a strong impact on these properties.[6] The Xia group has previously reported the synthesis of small single-crystal Ag nanospheres, but this method

could not be used to produce Ag spheres larger than ~30 nm, as additional growth would lead to the transformation of the spheres into sharp cubes or the development of a highly faceted cuboctahedral structure.[26] Though these small nanospheres can be used for solution-phase SERS measurements,[27] previous studies showed no signal from single 30-nm silver spheres on a substrate,[28] illustrating the limitations of spheres of this size for substrate-based SERS studies of controlled nanoparticle aggregates.

Substrate-based SERS studies are important because one of the most interesting areas of research for SERS is the hot-spot phenomenon, where regions of very high enhancement are observed in the small gaps between two or more particles.[29] This phenomenon has been used to record Raman spectra from single molecules, making it a promising tool for trace biomarker detection.[5] Recently, our group has published a detailed study for isolating the hot spot between two Ag nanocubes.[21] Due to the strong effect of sharp corners on SERS properties, comparing this data with that of hot spots between two spheres is an important step in understanding the fundamentals of hot-spot enhancement and enabling rational design of detection systems in the future. In initial studies with dimers made of 30 nm spheres, the signal intensity was low due to the small number of molecules in the hot-spot region and it was impossible to get a signal from similarly sized single particles for comparison.[28] Clearly, a need exists for larger nanospheres so that we can improve upon these important fundamental studies.

Another interesting type of nanostructure for SERS that is difficult to create with current synthetic techniques is asymmetric structures. The majority of nanocrystals that have been achieved thus far are highly symmetric, as confined by the face-centered cubic

lattice taken by most metals.[15,16] Of the anisotropic shapes that have been observed, the majority (e.g., bars, rods, and wires) were a result of preferential growth along a single direction.[30,31] To further increase the diversity of nanocrystal shapes and study the effect of asymmetry on SERS substrates, we needed to find new routes to break the cubic symmetry and thus force the growth process into other anisotropic modes.

In this chapter, I will discuss the synthetic methods for Ag nanostructures that I have developed to overcome these challenges. First, in Section 2.2 I will discuss the synthesis of Ag nanocubes, as this previously demonstrated morphology is the starting point for both the syntheses of the other Ag nanostructures presented in this chapter and the synthesis and applications of Au-Ag nanocages that will be discussed in Chapters 3 and 4, respectively. In Section 2.3, I will discuss the synthesis and SERS properties of asymmetrically truncated octahedrons, a non-centrosymmetric shape that is half cube, half octahedron. I found that etching was a key parameter in the development of this unusual shape. Studying this morphology also allowed us to probe the effect of asymmetry on SERS enhancements. Finally, in Section 2.4 I will discuss how carefully controlled etching can also be used to create high-quality, single-crystal spheres with a range of sizes.

2.2. Sulfide-Mediated Polyol Synthesis of Ag Nanocubes

The polyol process is a robust and versatile method for generating Ag nanostructures.[15,16] By varying the reaction conditions, such as temperature, reagent concentration, and amount of trace ions, it is possible to achieve a high degree of control over both nucleation and growth, and thus the final products. In a typical synthesis, a polyol, such as ethylene glycol, serves as both a solvent and source of reducing agent.[15,16] A capping agent and a Ag precursor are injected into a pre-heated polyol, and the reduction of Ag^+ ions results in the nucleation and growth of Ag nanostructures. Although ethylene glycol alone can reduce a typical Ag precursor at an elevated temperature, upon closer investigation the primary reducing agent was found to be glycoaldehyde.[32] This compound forms when ethylene glycol is heated in the presence of oxygen (typically from air). The relevant reaction is:

$$2HOCH_2CH_2OH + O_2 \rightarrow 2HOCH_2CHO + 2H_2O \qquad (2.1)$$

To confirm the involvement of glycoaldehyde in the reaction, previous group members used a spectroscopic method to measure the amount of this intermediate compound by converting glycoaldehyde to glyoxal bis-2,4-dinitrophenylhydrazone, which strongly absorbs light at 570 nm. When oxygen- or air-saturated ethylene glycol was heated at 150 ^oC for 1 h, a clear peak developed at this wavelength. Additionally, the amount of glycoaldehyde present decreased slightly when $AgNO_3$ was added, though the details of this reaction are complicated by the catalytic abilities of Ag nanoparticles.[32]

At the initial stage of the reduction process, Ag atoms form small clusters whose structure can fluctuate. The ease at which the structure of such small clusters can change has also been demonstrated by high-resolution transmission electron microscopy (HRTEM) imaging, where the structure was observed to change during exposure to an electron beam.[33,34] As the Ag clusters grow larger, they become more stable and emerge to one of three predominant structures: single crystalline, single twinned, and multiply twinned. Here, these larger clusters of Ag atoms are typically called seeds, from which they will ultimately grow into nanostructures with different shapes.[15] Typically, the single crystalline seeds will initially grow into cuboctahedrons. As additional Ag atoms are added, the corners start to sharpen, resulting in the formation of nanocubes enclosed by {100} side faces.[26] However, if single twin seeds are formed, the growth will lead to right bipyramids; and if multiply twinned seeds are formed, the growth will occur more rapidly at the twin defects of the seed, resulting in the formation of wires with a pentagonal cross section.[35,36] Consequently, in order to control the morphology of Ag nanostructures one must be able to control the crystallinity of the seeds.

Multiple techniques have been used to control the crystallinity of Ag seeds and to generate specific nanostructures such as Ag nanocubes in high yields.[26,37] Initial methods focused on oxidative etching, as twinned structures are more susceptible to etching than single crystalline ones.[26] For example, by adding trace amounts of Cl^- to a polyol synthesis it is possible to remove single twinned and multiply twinned seeds and selectively obtain Ag nanocubes.[26] By controlling the amount of oxidative etching through the introduction of ionic species such as Br^- or $Fe^{2+/}Fe^{3+}$, the selective growth of

bipyramids and wires has also been demonstrated.[35,36]

More recently, other categories of trace ions have also been shown to have strong influences on the polyol synthesis of Ag nanostructures. One ion that has proven exceptionally useful is hydrosulfide (HS^-).[37] This ion has been shown to dramatically increase the reduction rate of $AgNO_3$ in the polyol system, making rapid, large-scale production of Ag nanocubes considerably easier. In this reaction, Ag_2S nanocrystallites are thought to form immediately upon the introduction of $AgNO_3$ (due to the extremely low solubility of Ag_2S), which then serve as both catalysts and seeds for further growth.[37] The formation of Ag_2S seeds is difficult to monitor with TEM, but a transient purple color at the beginning of the synthesis (not typical for other Ag syntheses) and previous demonstrations of Ag_2S as a catalyst for Ag reduction support this mechanism.[39,40]

Figure 2.2 shows the experimental setup and electron microscopy analysis of the typical reaction product for this synthesis.[41] Figure 2.3 shows the morphological evolution of the reaction product through TEM analysis of small aliquots removed at different stages of the synthesis. As seen in earlier nanocube syntheses, the initial cuboctahedral seeds grow into sharp cubes due to more rapid growth on the {111} corner regions than the {100} sides. This facet-specific growth has been attributed to preferential binding of the surfactant used in the synthesis, poly(vinyl pyrrolidone) (PVP). The role of this polymer in shape control has been examined both in the synthesis of Ag nanowires via a polyol process,[42] and in the seed-mediated overgrowth of Ag spheres in an aqueous system.[43] When Ag cuboctahedrons enclosed by a mix of {100} and {111} facets were used as seeds for further Ag reduction with ascorbic acid, the final

morphology depended on which capping agent was present in the solution. When citrate was used, {111}-capped octahedrons would be the primary product, while {100}-capped cubes would become the dominant product when PVP was used instead.[43]

One critical difference between the large-scale setup shown here and the small-scale reaction in vials that was initially demonstrated is the use of argon gas.[41] By introducing a light flow of argon gas shortly before the injection of reagents, it was possible to increase the product purity and reproducibility of the reaction. Though the presence of oxygen is helpful in syntheses based on oxidative etching (such as the Cl^--mediated method discussed above), it has an adverse effect on the sulfide-mediated synthesis of Ag nanocubes. Four different gases were introduced into the system to examine the effect of oxygen: oxygen, air, nitrogen, and argon.[41] Only when nitrogen and argon were used, could we obtain nanocubes with a high yield. The most likely explanation of this observation is that the presence of oxygen disrupts the initial Ag_2S seeds, as the products obtained with oxygen present had a variety of crystal structures.

This method has made it possible to > 0.1 g of Ag nanocubes in one batch, with a total reaction time of less than 2 h. This is a critical first step for the large-scale production of Au-Ag nanocages that will be necessary for the biomedical applications discussed in later chapters. The synthesis of Ag nanocubes can also serve as a starting point for the synthesis of other Ag morphologies, which I will discuss next.

2.3. Etching and Growth: An Intertwined Pathway to Ag Nanocrystals with Exotic Shapes

Though Ag nanocrystals with a wide variety of symmetric shapes have been synthesized, new methods are necessary to create asymmetric structures.[15] Recently, seeded overgrowth has been demonstrated as a versatile route to the formation of nanocrystals with both simple and complex shapes and compositions, including bimetallic samples.[16,44-46] A typical example is the transformation of Ag nanocubes into their geometric dual, octahedrons, through preferential overgrowth at all {100} facets.[16,46] In this section, I present a new etching-induced growth mechanism by which Ag nanocubes are transformed into nanocrystals with an exotic, previously unattained shape: anisotropically-truncated octahedrons.[47] In this case, the overgrowth occurred preferentially on three adjacent faces of the six available, all of which surround a corner slightly truncated due to oxidative etching, resulting in a non-centrosymmetric shape despite the single crystal structure.

The synthesis started with a typical sulfide-mediated polyol process for Ag nanocubes, similar to that described in Section 2.2, but without argon protection.[37,38] At the end of this process, a second aliquot of silver nitrate ($AgNO_3$) solution was added and, to my surprise, the cubic nanocrystals evolved into anisotropically-truncated octahedrons, a shape of lower symmetry relative to a cube or octahedron. Figure 2.4 shows electron micrographs of the sample before and after the second aliquot of $AgNO_3$ solution was introduced. As shown in Figure 2.4A, the sulfide-mediated synthesis gave a uniform sample of Ag nanocubes 46 nm in edge length. Ten minutes after the addition of

the second aliquot of $AgNO_3$ solution, essentially all the Ag cubes had been transformed into anisotropically-truncated octahedrons (Figure 2.4B) of 68 nm in size as measured along the longest edge. Different from a regular octahedron, three adjacent corners of this new nanocrystal are snipped significantly, as illustrated in Figure 2.4c.

It has been previously shown that gradually adding $AgNO_3$ and PVP solutions to the product of a conventional polyol synthesis over the course of 2 h could facilitate the transformation of Ag cubes of 80 nm in edge length into octahedrons of 300 nm in size.[16] This shape transformation could be attributed to faster addition of Ag atoms to the {100} faces of the cube than the {111}-capped corners. In the present work, I propose that the same principle of more rapid growth on {100} faces is still valid, but in a much less symmetrical pattern. Instead of being added to all six faces of the cube evenly, the Ag atoms were added to three adjacent {100} faces more rapidly than the other three {100} faces. Figure 2.4C shows a schematic of this new growth mechanism, where white and grey signify the {111} and {100} facets, respectively. The three fast-growing {100} faces are determined by a slightly truncated corner, which is believed to be the source of the highly anisotropic growth (see below). As a result, half of the cube grows into an octahedron while the other half retains a truncated cubic morphology. When sitting on a substrate, such an exotic nanocrystal typically takes on one of two orientations. Either it sits on the large {111} facet on the "octahedron side" of the crystal, or it sits on one of the three square {100} facets. Figure 2.4d shows both of these orientations, which match well with what was observed under SEM and TEM (Figure 2.4B).

Both the formation of Ag nanocubes that serve as the seeds and the subsequent

growth into anisotropically-truncated octahedrons are rapid processes. The presence of sulfide species, in this case HS^-, results in accelerated growth of the cubes in the first step due to the generation of Ag_2S, a known catalyst for Ag reduction.[37-40] The reaction involved in the second step is also rapid; the injection of $AgNO_3$ takes less than one minute and the final product is harvested 10 min later. This rapid rate makes it possible for the final shape to be kinetically determined instead of being the thermodynamically favored one at this size, a cuboctahedron (or a truncated octahedron). To confirm the importance of this rapid growth, a similar experiment was performed except the second aliquot of $AgNO_3$ was added 15 times more slowly, at a rate of 0.05 mL/min rather than 0.75 mL/min. Instead of growing anisotropically, the Ag atoms were added uniformly to all six {100} faces, retaining the cubic morphology during overgrowth (Figure 2.5A).

Oxidative etching is also an important factor in determining the final shape of nanocrystals obtained in a solution-phase synthesis and has been proposed as a basis for the activation of specific face(s) of a nanocrystal for further growth.[15,48] In my group's previous work, both a rapid reduction rate and localized oxidative etching were shown to be critical for breaking the cubic symmetry and promoting anisotropic growth of Ag and Pd cubes into rods or bars. Adding a capping agent that prevents oxidative etching was shown to shorten Pd nanobars significantly, resulting in a cubic shape.[48] Etching may also play a role in the synthesis of Ag nanobars as increased concentrations of the etchant Br^- were necessary for their growth.[30] A similar mechanism appears to be responsible for the anisotropic growth observed in the present study as well, with a significant difference: instead of a single face being activated for further growth, the etching of one corner of

the cube promotes growth on all three adjacent faces connected by this corner. Mild etching is known to occur in the late stages of a sulfide-mediated Ag nanocube synthesis. The corners of the cubes have been shown to round irregularly if the reaction was left unquenched after all the $AgNO_3$ had been consumed.[37] As indicated by arrows in the inset of Figure 2.4A, a number of particles could be seen with uneven corner truncation. A close examination of multiple micrographs of the nanocubes in Figure 2.4A indicates that ~20% of them appear to be truncated at one corner. It is not expected to see truncation on every cube since the contrast difference can be difficult to see if the truncation is not significant enough. This uneven etching could activate one corner of the cube, and the Ag that is dissolved from this region is likely to be re-deposited in a nearby area, activating the adjacent three faces for further growth once additional $AgNO_3$ is introduced. The stirring in this reaction is mild and thus should allow for local forces to play a significant role. To confirm the importance of oxidative etching in our mechanism, the same reaction was performed with an Ar-saturated solution. In this case, no shape transformation was observed and the final product was simply Ag nanocubes (Figure 2.5B) as no face was preferentially activated.

To confirm my assignment of this unusual shape, extensive electron microscopy analysis was performed and all results were consistent with an anisotropically-truncated octahedron. Other geometries were also investigated, including bipyramids, truncated tetrahedrons, and unevenly truncated cubes, but none of them could explain all the data presented here. Figure 2.6A shows a high-magnification SEM image, allowing the faceted nanocrystals to be better resolved. This image clearly shows multiple examples of

the two most common profiles of the nanocrystals: “houses” and triangles. A typical “house” orientation is shown in Figure 2.6B at three different tilting angles, in comparison to a model. The two sets of images match closely, though the actual nanocrystals are slightly more rounded when compared with the idealized model due to corner truncation. Further tilting of this model also suggests that the seemingly non-uniform appearance of the sample is most likely caused by its highly unsymmetric nature (Figure 2.7).

High-resolution TEM analysis in Figure 2.8 validates the single crystal structure of the product, confirms the presence of both {100} and {111} facets, and verifies the fringe spacings expected from the model at different orientations. Figure 2.8, A and B, shows the analysis of a nanocrystal sitting on the large triangular face bound by a {111} plane. The fringe spacing of 1.4 Å can be indexed to the {220} reflection of Ag. The inset in Figure 2.8B shows a fast Fourier transform (FFT) of the high-resolution image, where the spots have a 6-fold symmetry and can be indexed to the {220} reflection, indicating that the nanocrystal was sitting on a {111} face. Figure 2.8, C and D, shows the analysis of a nanocrystal sitting on a square {100} face. The fringe spacing of 2.0 Å corresponds to the {200} reflection of Ag. The FFT pattern in the inset shows a square symmetry and spots for both the {200} and {220} reflections, indicating that the nanocrystal is sitting on a {100} face.

Figure 2.9A shows UV-vis spectra recorded from solutions of the two different stages depicted in Figure 2.4. After the second $AgNO_3$ aliquot was added, the primary peak redshifted by 25 nm, as would be expected from a size increase, and a new peak

developed at 380 nm between the two peaks seen in the spectrum for nanocubes. Previously, discrete-dipole approximation (DDA) calculations for 40-nm Ag cubes and octahedrons showed that the main peak for octahedrons is located between the two peaks of a similarly sized cube as we see here, supporting our claim that our structure is a hybrid between a cube and an octahedron.[6a] Additionally, we performed DDA calculation for an anisotropically-truncated octahedron that is depicted in Figure 2.10. We used 3,424 dipoles and the three sharp points of the "octahedron side" were snipped by 11.7 nm to reflect the slightly truncated nature of the particle and to match the experimental spectra more closely. As shown in Figure 2.9B, the same overall shape can be seen, with a clear shoulder at 380 nm.

These unusual nanocrystals were further investigated for SERS applications. It is well known that nanocrystals with sharp tips, such as the points of an octahedron, can concentrate the field into small volumes and thus create regions with higher enhancement.[20] However, it is still not clear if the sharp corners need to be positioned in a specific configuration in order to generate a strong, localized electric field. To investigate this, preliminary measurements were performed with 1,4-benzenedithiol (1,4-BDT) and a 514 nm laser to test the SERS capabilities of the new nanocrystals. Well-resolved spectra could be easily obtained and a typical example of the solution-phase spectrum is shown in Figure 2.9C, from which an enhancement factor of 7.5×10^3 was obtained for the 9a ring breathing vibration at 1183 cm^{-1}. Single particle SERS spectra could also be obtained and a typical example is shown in Figure 2.9D. To see if the asymmetry of this morphology affects the SERS enhancement, we compared the

enhancement factors obtained with 68 nm asymmetrically truncated octahedrons with identical SERS measurements on 50 nm Ag octahedrons (enhancement factor: 1.1×10^4). The difference between the enhancement factors is too small to be significant given the experimental error in SERS measurements (~20%).[43]

In summary, I have demonstrated anisotropic overgrowth that proceeds more quickly from three adjacent faces sharing a common, single corner of a nanocube activated by to oxidative etching. Rapid reduction was also found to be a key factor in this unique shape transformation. The final products are anisotropically-truncated octahedrons, which show a novel, non-centrosymmetric shape with interesting features for fundamental studies of SERS.

2.4. Controlled Etching as a Route to High Quality Ag Nanospheres for Optical Studies

As seen in Section 2.3, corrosive mechanisms such as etching have been found to be a powerful tool in the synthesis of complex metal nanocrystals. Etching has been used to control the crystallinity of seeds formed in the early stages of nanocrystal growth,[15,26] activate specific facets of a nanocrystal for preferential growth,[47] create hollow structures,[49,50] and truncate sharp corners/edges.[51] In order to dissolve a metal, wet etchants typically contain both an oxidant and a ligand that will coordinate with the resulting metal ions.[52] Oxygen from air can be used as an oxidant, but commonly used etching solutions usually rely on an additional oxidant such as Fe(III).[53]

By increasing the amounts of an appropriate wet etchant added to a suspension of Ag nanocubes, I have developed a new method to not only round the corners in an aqueous system at room temperature system, but also to transform the Ag nanocubes into highly uniform nanospheres. Furthermore, the reaction could be easily monitored using a UV-vis spectrometer, and additional etchant could be added in a second step if more truncation was desired. The Xia group has demonstrated a number of methods to produce Ag nanocubes, and their size can be controlled from approximately 20 to 200 nm by adjusting the reaction parameters.[37,54-57] Since the etching typically produced nanospheres with roughly the same diameter as the initial nanocubes, this method can easily synthesize nanospheres with a wide range of sizes. While there are previous studies where researchers tried to create Ag nanospheres by annealing sharp Ag nanocubes in a dilute solution of hydrochloric acid in ethylene glycol, the resulting particles had clearly

truncated corners, but the products were not uniformly truncated and the synthesis was difficult to monitor due to the fact it took place rapidly in hot ethylene glycol.[17] With the water-based etching technique, however, the product was much more uniform and the products were truly spheres, not just truncated cubes. I used this method to study both the effect of sharp corners and edges on the far-field LSPR properties (extinction spectra) and the near-field SERS properties of both large and small Ag nanospheres. The large spheres had an order of magnitude higher enhancement factor, making them promising substrates for single particle and hot-spot SERS studies.

A monodisperse sample of Ag nanocubes is a critical starting point for the synthesis of high-quality nanospheres. Figure 2.11A shows the nanocubes before any etchant was added. As increasing amounts of 0.5 mM ferric nitrate solution were added, the cubes first became more rounded (Figure 2.11B) and then transformed into spheres (Figure 2.11C). Despite the frequently anisotropic nature of wet etching for crystalline materials,[57] the resulting Ag nanocrystals displayed an almost perfectly circular profile under TEM and retained their high level of monodispersity throughout the etching process. The high uniformity can be seen in the size distributions presented in Figure 2.11D, calculated from measurements of 100 particles. The cubes had a diameter of 42.5 ± 2.7 nm and the spheres had a slightly smaller diameter of 41.6 ± 2.6 nm. Despite the distinct change in morphology, the size could be carefully controlled so that the diameter of the final spheres was roughly the same as that of the initial cubes by adjusting the amount of etchant added. If desired, it is also possible to obtain nanospheres of smaller sizes through the addition of larger amounts of etchant.

This method was extended to nanocubes of larger sizes with a small modification to the protocol. Figure 2.12 shows the same morphological transformation as Figure 2.11, but in this case the starting material was 144 nm-Ag cubes. For these larger cubes, a ferricyanide etching solution gave a higher quality result than the ferric nitrate solution (Figure 2.13). Although the product from etching with ferric nitrate is roughly spherical, the profile is slightly irregular. Previous reports have shown that the ferricyanide solution etches Ag more rapidly than 5 mM ferric nitrate solution (note that this is 10x more concentrated than the 0.5 mM solution used for the 42 nm cubes).[53] As the volume difference between the two cube samples is related to the diameters to the third power, a more powerful etching solution may be required to dissolve the significantly larger amount of Ag uniformly. A 10x diluted ferricyanide solution could also etch small cubes, but I chose to use the system based on ferric nitrate when possible due to the low toxicity, low cost, and ease of use of this etchant.

The large cubes displayed a retention of uniformity similar to the small nanocubes, as shown in Figure 2.12D. The cubes had an average size of 144.2 ± 12.6 nm and the spheres had an average size of 142.6 ± 13.5 nm. A few particles can be seen with a less spherical shape, but these are likely due to the fact that the initial sample of nanocubes contained a minority product of bipyramids due to incomplete removal of singly twinned seeds during the cube synthesis. Close examination of the SEM images of the rounded cubes in Figure 2.12B showed that etching had occurred on both the edges and corners of the nanocube. The inset of Figure 2.12B shows a nanocube oriented such that truncation of the sharp edges of the cube is clearly visible.

The etching process is illustrated in a schematic in Figure 2.14A. The edges in the second step are outlined for clarity in the schematic, but the actual particles are more rounded. Moving from left to right, more etchant is added and the resulting particles become increasingly rounded, until they finally become spheres with no flat faces or corners. This preferential elimination of sharp edges and corners could be due to the higher surface area exposed to the etchant in boundary regions when compared to flat faces and the fact that PVP has been shown to cap {100} side faces of cubes more strongly than other facets.[42] Figure 2.14, B and C, shows high-resolution TEM images of a typical nanosphere. The almost perfectly circular profile can be seen clearly at this high magnification. The 2.4 Å lattice fringes could be indexed to the {111} spacing of Ag, which extended across the entire nanosphere, showing that it retained its single crystallinity throughout the transformation.

I also investigated other common etchants as a comparison. Figure 2.15A shows the results from etching with a mixture of 3% ammonium hydroxide and 3% hydrogen peroxide and Figure 2.15B shows the results from etching with 30% ammonium hydroxide. Neither of these systems gave nearly as uniform a product as the etchants described above. A possible explanation for the uneven rounding with the etchant in Figure 2.15A is that oxygen bubbles generated by hydrogen peroxide might cause non-uniform etching across the surface of the nanocrystal.[53] The low quality of the particles etched with 30% ammonium hydroxide fits with previous reports where non-uniform etching of Au-Ag nanocrystals was attributed to the uneven dissolution and diffusion of oxygen from air in the reaction solution, as no other oxidant is present in this system.[50] It

is also possible that the stronger etchants could attack any surface of the cube while these weaker ones preferred the areas which had already been somewhat etched, resulting in products with only one or two corners being truncated (Figure 2.15A) and the overall anisotropy shown in Figure 2.15B.

Initial studies with 54-nm cubes indicated that extremely rapid mixing was necessary to obtain highly smooth spheres. Figure 2.16 shows a comparison of cubes etched with the same amount of ferric nitrate etchant, but panel A was obtained using a vortex mixer and panel B was obtained on a stir plate at 300 rpm (a typical speed used in other reactions). The surfaces of the particles etched on the stir plate were rough and uneven. Increasing the stir rate to the maximum value available (~1,000 rpm) improved the quality somewhat, but was still not equal to that obtained with a vortex mixer. Rapid mixing ensures a constant supply of reactive species to the nanocrystal surface, which is critical due to the rapid rate of etching and the strong effect of mass transport on the etching reactions.[58]

I further investigated the effect of protecting the surface of the nanocubes with SAMs of different capping agents before etching. Wet etching has been combined with microcontact printing of SAMs with great success to generate complex patterns in thin metal films.[52,53,59] In the present study, nanocubes were centrifuged and then re-suspended in ethanolic solutions of thiols with different chain lengths and functional groups. After washing away excess capping agent, these cubes were etched with the same amount of ferric nitrate solution necessary to produce spheres in the PVP-capped system (Figure 2.17). Moderate length thiols (6-mercapto-1-hexanol) were found to

completely protect the nanocubes from etching (Figure 2.17A), while thiols with short chains (2-mercaptoethanol) provided no protection and the cubes were etched completely to spheres as in the PVP-capped system (Figure 2.17B). From this observation, it appears that the long chain molecules were able to effectively exclude ions from the surface through the creation of a boundary layer, while shorter chains allowed the etchant molecules to come close enough to the surface to react. Electronic stabilization has been previously proposed as a potential mechanism for SAM protection of Ag nanostructures against anodic dissolution, but that does not appear to play a role here as the short chain thiol did not provide protection while the moderate length thiol did.[60] Cubes covered with amino- or carboxylic acid-terminated alcohols (6-amino-1-hexanol and 6-hydroxycaprioic acid, respectively) were also etched easily due to the weaker interactions between these molecules and the Ag surface, similar to previous reports.[60]

Interestingly, the morphological transformation during the etching process could be reversed; spheres generated from the truncation of 54-nm Ag cubes (cubes: Figure 2.18A, spheres: Figure 2.18B) could be re-grown into cubes through titration with a dilute solution of $AgNO_3$ in the presence of PVP. The titration was performed in pre-heated EG which served as both the solvent and reducing agent, as in a typical polyol synthesis. By adjusting the amount of $AgNO_3$ added, we could control the reverse transformation, creating truncated cubes with the addition of 1 mL of solution (Figure 2.18C) and sharp cubes with the addition of 1.5 mL of solution (Figure 2.18D).

The controlled morphological transformation (without any changes in particle concentration or uniformity) allowed us to investigate the effect of sharp corners and

edges on the LSPR properties of Ag nanostructures. Figure 2.19A shows the UV-vis spectra of the samples shown in Figure 2.11. All suspensions started with the same amount of Ag nanocubes and were diluted to a volume of 0.5 mL, so the differences in intensities are solely due to the particles themselves, not concentration differences. Theoretical spectra calculated using Mie theory (for spheres) and the DDA method (rounded and sharp cubes) are shown in Figure 2.19B for comparison.[18] Calculations were performed for Ag particles in water with a grid of 30 x 30 x 30 dipoles. The rounded cube was truncated by 8 nm at both the edges and the corners. The sharp cubes were also truncated by 1.4 nm in order to take into account the slight rounding present in real particles. The same overall trends are seen in the calculations that are seen in the UV-vis spectra, though the peaks are slightly red-shifted, likely due to further rounding of the edges of the particles when compared with the more defined truncation in the model.

As the particles become more rounded due to etching, the LSPR peak gradually blue-shifts. Structures with sharp corners have red-shifted peaks when compared to rounded structures of the same size due to the additional charge separation possible in these structures. The increased separation reduces the restoring force for the dipole oscillation, resulting in a reduced frequency and longer wavelength. The UV-vis spectrum of sharp cubes (black trace) showed a strong peak, a weak peak, and a shoulder. After partial rounding (blue trace), the shoulder disappeared, and after the cube had been completely etched into a sphere (red trace), only the strongest peak remained. The two peaks in the sharp and rounded cube spectra are visible in the DDA-calculated spectra

and have been assigned to dipole resonances through quantitative analysis based on DDA calculations.[61] The additional weak dipole peak was present for the cubes but not the spheres due to the additional resonances possible with the lower symmetry of the cubic shape.[62] The small shoulder that appeared between the two dipole peaks in the spectrum was not predicted in calculations for cubes of this size, but had been ascribed to a quadrupole resonance in calculations for cubes that were slightly larger.[61] The intensity also gradually weakened as the cube was etched into a sphere, likely due to the fact that approximately half the Ag was dissolved from each particle, so fewer electrons would be resonating with the incoming light.

Calculations were also performed for nanocubes with only corner truncation, instead of both corner and edge truncation, and the primary dipole peak red-shifted ~50 nm compared to the calculations for the cubes with both corners and edges truncated (Figure 2.20). From this data it is clear that both the sharp corners and edges of cubes are important in determining their optical properties.

With larger particles, quadrupole resonances have a more significant role. Figure 2.19, C and D, shows the UV-vis spectra and the spectra calculated with Mie theory and the DDA method for the 144-nm particles shown in Figure 2.12, respectively. Four resonances were present for the sharp cubes in both the experimental and theoretical spectra. The strong peak around 800 nm is related to the primary dipole peak in the spectra for the small cubes and the strongest peak around 550 nm is related to the weak quadrupole shoulder seen in the 42-nm cubes with sharp corners. The small peak and shoulder around 450 nm contained a mixture of both dipole and quadrupole resonance

modes.[61] All peaks were still present for the rounded cubes, though the positions were slightly blue-shifted when compared to the pristine cubes due to the decreased sharpness. In the spectra and calculations for the spheres, however, the weaker dipole/quadrupole mixed peaks had disappeared due to the higher symmetry of a sphere than a cube, as was seen in the 42 nm samples.

Finally, spheres synthesized with this etching process were investigated for their SERS properties. Due to the rapid elimination of all sharp corners and edges, the spheres produced with this method are true spheres with rounded surfaces and no defined facets, allowing for more accurate fundamental studies than previously possible. Figure 2.21 compares solution phase spectra for 25-nm and 142-nm Ag nanospheres functionalized with 1,4-BDT. Previous work has been done in the past with 25-35 nm spheres as they were the only size available, but there are no previous studies on high-quality 142-nm Ag nanospheres. The 25-nm spheres had an enhancement factor of 8.9×10^3 while the 142-nm spheres had an enhancement factor of 1.0×10^5, an order of magnitude higher. The significant difference in enhancement factors may be influenced by the fact the 142-nm spheres have a broad LSPR peak that overlaps well with numerous lasers, including the 514 nm laser used here, while the LSPR peak for the small spheres is narrowly centered around 410 nm, making it difficult to get good overlap with the available lasers. Furthermore, the quality of the plasmon resonance in nanostructures can decrease in the sub-25 nm size regime due to damping from electronic scattering processes at the particles surface, which may also be affecting the overall enhancement.[12] The ability of this method to produce spheres with a variety of sizes and significantly higher

enhancement factors opens up new possibilities for SERS studies that were not feasible with the limited methods available before, as the stronger signal will allow for substrate-based single particle and improved dimer studies.

I have demonstrated a simple and rapid route to single-crystal Ag nanospheres based on wet etching of uniform Ag nanocubes. By limiting the amount of etching solution added, I can also synthesize rounded Ag nanocubes where all sharp corners and edges are truncated. Rapid mixing and the choice of an appropriate strong etchant were both key parameters to obtaining a high-quality sample. SAMs made of alkanethiols with moderate chain lengths can protect against this etching, though short chain thiols like 2-mercaptoethanol, and amine and carboxylic acid terminated molecules could not. The morphological transformation due to etching could also be reversed: by titrating with $AgNO_3$ the sharp features of the cubes could be restored. The LSPR properties of these spherical nanocrystals were compared with theoretical spectra, and the strong effect of sharp corners and edges on extinction spectra was clearly visible. Finally, these spheres were used as substrates for SERS, and it was found that 142-nm spheres had an order of magnitude higher enhancement factor than 25-nm spheres. The ability to synthesize large spheres with high enhancement factors opens new doors for fundamental SERS studies in the future.

2.5. Experimental Section

Materials. Silver nitrate ($AgNO_3$, Sigma-Aldrich, 05621AD), sodium hydrosulfide (NaHS, 02326AH), poly(vinyl pyrrolidone) (PVP, MW ≈ 55,000), silver nitrate ($AgNO_3$, 06005KJ), hydrochloric acid (HCl, 37%), ferric nitrate ($Fe(NO_3)_3$), potassium thiosulfate ($K_2S_3O_3$), potassium ferricyanide ($K_3Fe(CN)_6$), potassium ferrocyanide ($K_4Fe(CN)_6$), ammonium hydroxide (NH_4OH, 28%), hydrogen peroxide (H_2O_2, 3%), 2-mercaptoethanol ($HS(CH_2)_2OH$), 6-mercapto-1-hexanol ($HS(CH_2)_6OH$) and 6-amino-1-hexanol ($H_2N(CH_2)_6OH$) were all obtained from Aldrich and used without further purification. Ethylene glycol (EG, J. T. Baker, Lot No. G32B27 for sulfide-mediated synthesis and Lot No. E51B18 for HCl-mediated synthesis) and 6-hydroxycaprioic acid ($HOOC(CH_2)_5OH$, Alfa Aesar) were also used without further purification. All water used was purified with a Millipore E-pure filtration system at >18 MΩ cm.

Synthesis of Ag Nanocubes: 60 mL of EG was added into a 250 mL three-neck round-bottom flask and heated in an oil bath at 150 ^oC under magnetic stirring with a large, egg-shaped Teflon-coated stir bar (VWR, Cat. No. 58949-200). After 50 min of pre-heating, a flow of argon was introduced over the top of the solution via a glass pipette at a flow rate of 1200 mL/min, as shown in Figure 2.2A. After 10 min, 0.7 mL of a NaHS solution in EG (3 mM) was quickly injected into the pre-heated EG solution, followed 8 min later by injection of 15 mL of PVP solution in EG (20 mg/mL) and 5 mL of $AgNO_3$ solution in EG (48 mg/mL). The reaction flask was capped with a septum with a small opening to allow the gaseous species to escape from the flask. Shortly after the addition

of $AgNO_3$, the reaction solution went through four distinct stages of color change in the order of golden yellow, deep red, reddish grey, and then green ocher within about 20 min. The green ocher color indicated the formation of uniform Ag nanocubes with an edge length around 45 nm. The reaction solution was then quenched by placing the reaction flask in an ice-water bath. Quenching at a slightly earlier point (while the reddish color was still visible) resulted in smaller nanocubes with an edge length of ~35 nm.

Synthesis of ATOs. In a typical synthesis, 6 mL of EG was dispensed in a 24 mL vial (VWR, 24 mL, cat. no. 66011-143) containing a Teflon-coated magnetic stir bar and loosely capped with a paper-lined lid. A small hole was drilled in the center of the lid. This vial was then heated in a 152 ^oC oil bath for 1 h after which the cap was removed, 70 μL of a 3 mM NaHS solution in EG was injected with a micropipette, and the vial was loosely capped again. Approximately 8 min later, the cap was removed and a PVP solution (30 mg in 1.5 mL EG) and a $AgNO_3$ solution (24 mg in 0.5 mL EG) were injected, after which the cap was firmly tightened. Upon addition of $AgNO_3$, the solution first turned yellow, then brown, and finally became an opalescent silver color. After 10 min, a small aliquot was taken with a glass pipette through the hole in the cap, with the vial staying sealed. At this point, an additional aliquot of $AgNO_3$ solution (24 mg in 0.5 mL EG) was added using a syringe pump at a rate of 0.75 mL/min (or 0.05 mL/min for the control experiment), also through the hole in the cap. After heating for another 10 min, the reaction was quenched in an ice bath. The contents were then washed once with acetone and twice with water through centrifugation before being dispersed in water. For argon-protected syntheses, the preheated EG and all other solutions were bubbled with

argon for 1 h and argon flow was maintained over the surface of the reaction solution as reagent solutions were added.

Etching of Ag Nanocubes. The 54-nm cubes and the 42-nm cubes were produced using the sulfide-mediated polyol synthesis described above.[41] The 144-nm cubes were synthesized using a HCl-mediated polyol synthesis that involves the oxidative etching of twinned seeds, as this method seems to be better suited for the production of large nanocubes.[54] In a typical process, a small aliquot of Ag nanocubes in water (10 μL of small cubes or 50 μL of large cubes) was added to a small centrifuge tube containing PVP solution (1 mg/mL in water). The exact volume of PVP solution was adjusted slightly for each reaction so that the total volume was 0.5 mL to allow for straightforward comparisons of UV-vis spectra. Different amounts of etching solution (as indicated in the text) were then added, and the centrifuge tube was immediately capped and transferred to a vortex mixer for 15 s, during which time the majority of the etching occurred. The products were allowed to equilibrate for 10 min, at which point a UV-vis spectrum was taken and the particles were quickly washed via centrifugation and re-dispersion in ethanol a minimum of 3 times before being re-dispersed in water for imaging. The particles were typically collected by centrifuging at 13,200 rpm for 4-7 min. It was critical that all etching solutions were made fresh daily. The 42-nm and 54-nm Ag cubes were etched with a ferric nitrate solution, typically 0.5-5 mM depending on the concentration of the cube suspension. The 144-nm Ag cubes were etched with a light-sensitive ferricyanide-based solution that contained 100 mM $K_2S_3O_3$, 10 mM $K_3Fe(CN)_6$, and 1 mM $K_4Fe(CN)_6$. This solution is referred to as the "ferricyanide

solution" throughout the chapter. Note that extra care should be taken with this solution as the photodecomposed products contain free cyanide and HCN can be released if the solution is mixed with acid. I also compared two other etching solutions, either a 1:1 mixture of 3% ammonium hydroxide and 3% hydrogen peroxide or 30% ammonium hydroxide.

Protection of Ag Nanocubes. The Ag nanocubes were protected with self-assembled monolayers (SAMs) of different capping agents by centrifuging, removing the supernatant, and re-dispersing in an ethanolic solution of 6-mercapto-1-hexanol, 2-mercaptoethanol, 6-amino-1-hexanol or 6-hydroxycaprioic acid, followed by incubation for either 1 h (thiols) or overnight (amines and carboxylic acids). The nanocubes were then washed twice with water via centrifugation and redispersed in water for the etching step.

Re-Growth of Ag Nanospheres. The spheres were generated using 54-nm cubes and the etching procedure described above, except all volumes were increased 20 times and the reaction was performed in a 20 mL glass vial. After washing, the cubes were dispersed in 200 μL of EG. A 50 μL aliquot of this solution was added to a 6 dram vial containing 2 mL of EG that had been preheated for 1 h in a 152 ^{o}C oil bath and 1 mL of a PVP solution (20 mg/mL in EG) under magnetic stirring. The vial was then sealed with a cap having a small hole drilled in the center and the desired volume of $AgNO_3$ solution (48 mg/mL in EG) was injected with a syringe pump at a rate of 0.05 mL/min through the hole. After injection was complete, the heating was continued for 20 min to ensure complete reaction. The products were then washed with acetone and water.

Instrumentation. Transmission electron microscopy (TEM) images were captured with a Tenai G2 Spirit Twin microscope operated at 120 kV (FEI, Hillsboro, OR). High-resolution TEM images were captured with a field-emission 2100F operated at 200 kV (JEOL, Tokyo, Japan). Scanning electron microscopy (SEM) images were captured with a Nova NanoSEM 230 field-emission microscope (FEI, Hillsboro, OR) operated at an accelerating voltage of 15 kV. Samples were prepared by dropping an aqueous suspension of particles onto a piece of silicon wafer (for SEM) or carbon coated copper grid (for TEM). SPR spectra were recorded using a UV-visible spectrometer (Varian, Cary 50). For the samples etched with ferric nitrate, a background with an equal concentration of ferric nitrate was used to eliminate a peak from the etchant at ~300 nm to better resolve the spectral features in this region.

Surface-Enhanced Raman Spectroscopy. The SERS spectra were recorded from a solution phase using a Renishaw inVia confocal Raman spectrophotometer coupled to a Leica microscope with an 50x objective (N.A. = 0.90) in backscattering configuration. The 514 nm wavelength was generated from an argon laser and used with a holographic notch filter based on a grating of 1200 lines per millimeter. The backscattered Raman signals were collected on a thermoelectrically cooled (-60 °C) CCD detector. Sample cells were constructed by attaching the caps of microcentrifuge tubes to glass slides. The cap acted as a vessel for the liquid sample, and glass cover slips (0.17-0.13 mm) were carefully placed on top to eliminate solvent evaporation and to act as a reference point from which the focal volume was lowered to a depth of 200 μm into the sample. SERS data was collected with λ_{ex} = 514 nm, P_{laser} = 3.1 mW, and t = 30 s.

Processing of the Raman spectra and all data analysis was done with IGOR Pro software (Portland, OR). All data was baseline corrected before normalization. For the baseline correction a fourth order polynomial was fitted to the raw Raman spectrum and subtracted. Vector normalization was done by calculating the sum of the squared intensity values of the spectrum and using the squared root of this sum as the normalization constant. The band intensities of the 1563 cm^{-1} and 1182 cm^{-1} benzene ring breathing modes of 1,4-BDT were used to calculate the average enhancement factor (EF). The average EF was calculated using equation (2.2) shown below:

$$EF = (I_{SERS} \times N_{bulk}) / (I_{bulk} \times N_{ads}) \qquad (2.2)$$

where N_{Bulk} is the number of molecules in the scattering volume for the normal Raman measurement and N_{ads} is the number of adsorbed molecules in the scattering volume for SERS. I_{SERS} is the peak intensity of a band from the SERS measurement and I_{bulk} is the peak intensity of the same band from the normal Raman measurement. N_{ads} was calculated using the surface area measured from a model particle.

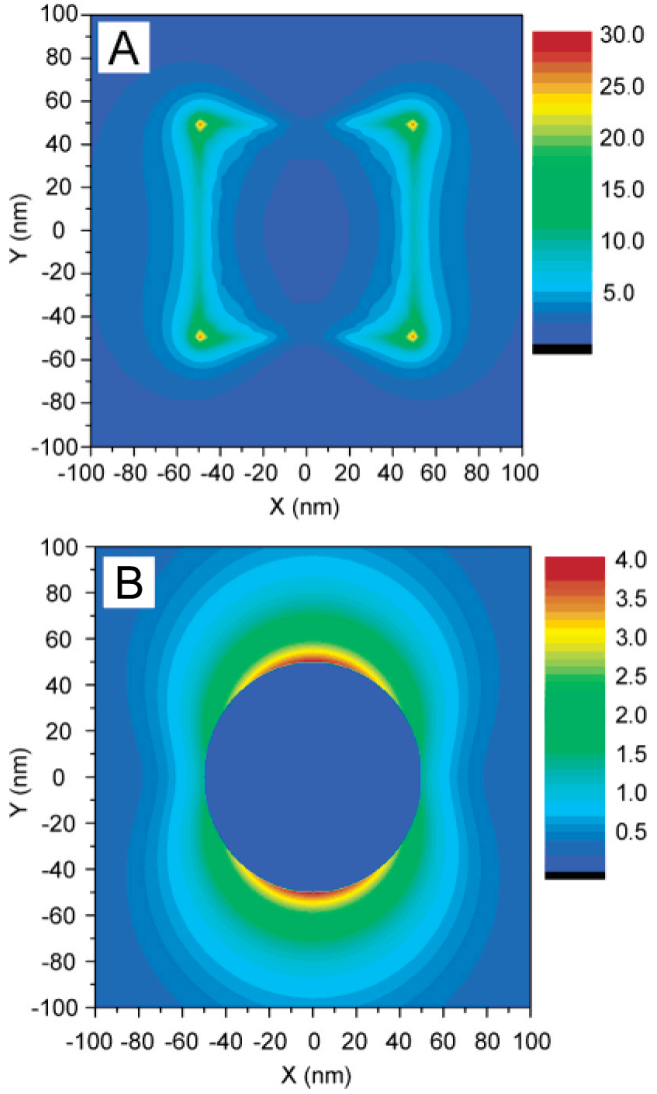

Figure 2.1. E-field amplitude (|E|) patterns for a 100-nm Ag cube and a 100-nm Ag sphere when irradiated at a wavelength of 514 nm: (A) 100-nm Ag cube, with the incident light along the z-axis and the E-field along the x-axis or [100] direction; (B) 100-nm Ag sphere, with the incident light along the z-axis and E-field along the y-axis. The incident field amplitude was assumed to be 1.

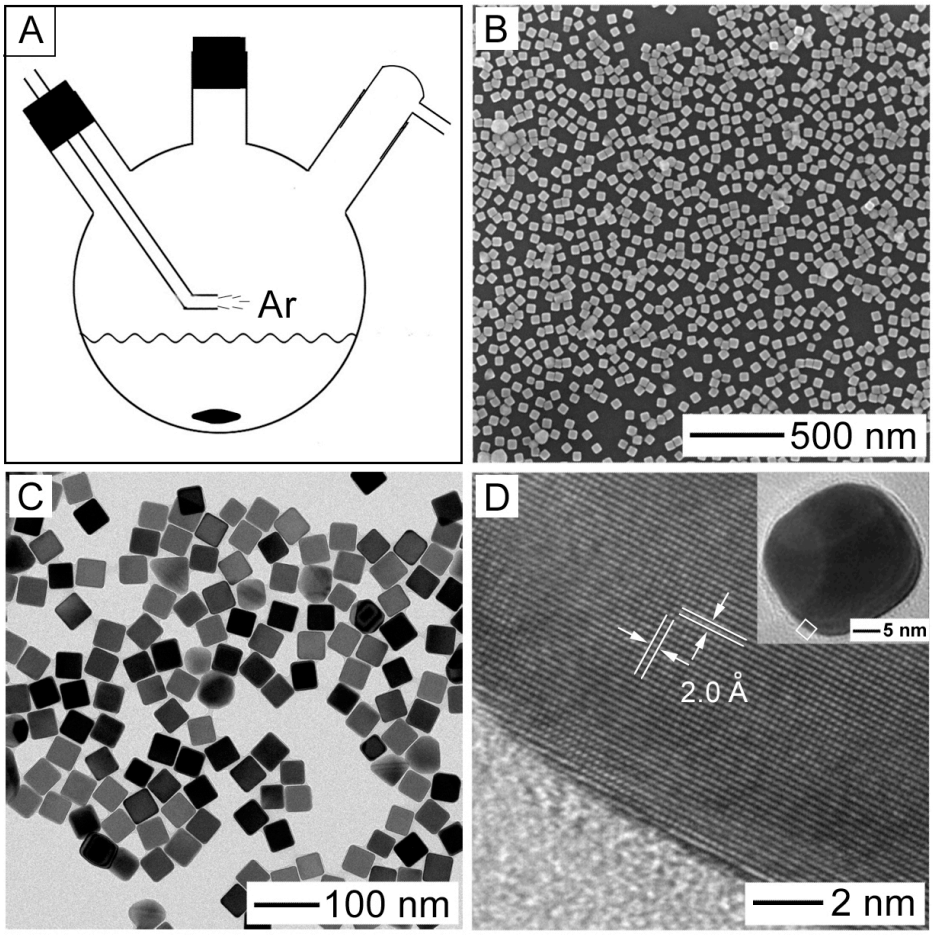

Figure 2.2. (A) Schematic illustrating the setup used for synthesizing Ag nanocubes on a scale of >0.1 g per batch. (B, C) SEM and TEM images of the as-synthesized Ag nanocubes, which were ~45 nm in edge length. (D) High-resolution TEM image of the selected area of an individual Ag nanocube shown in the inset.

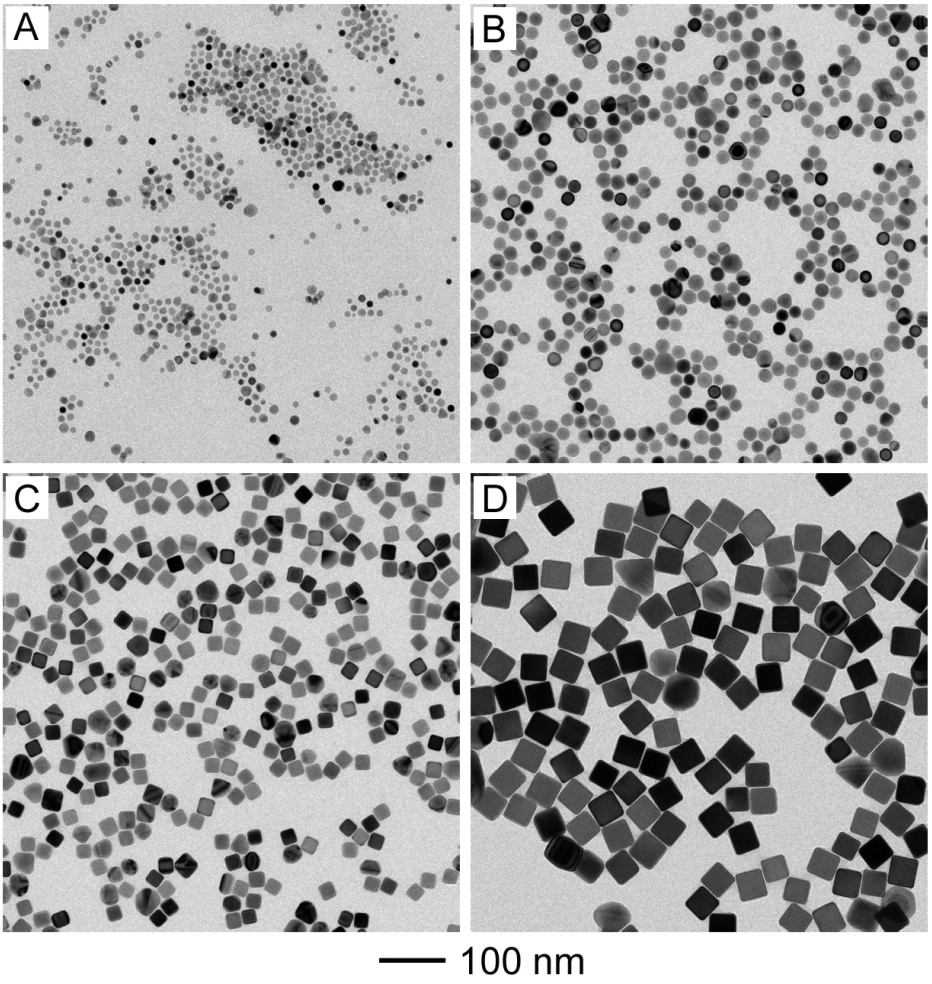

Figure 2.3. TEM images of four aliquots taken from the same synthesis (under argon) after the $AgNO_3$ solution had been added for different periods of time: (A) 5 min, (B) 10 min, (C) 15 min, and (D) 20 min.

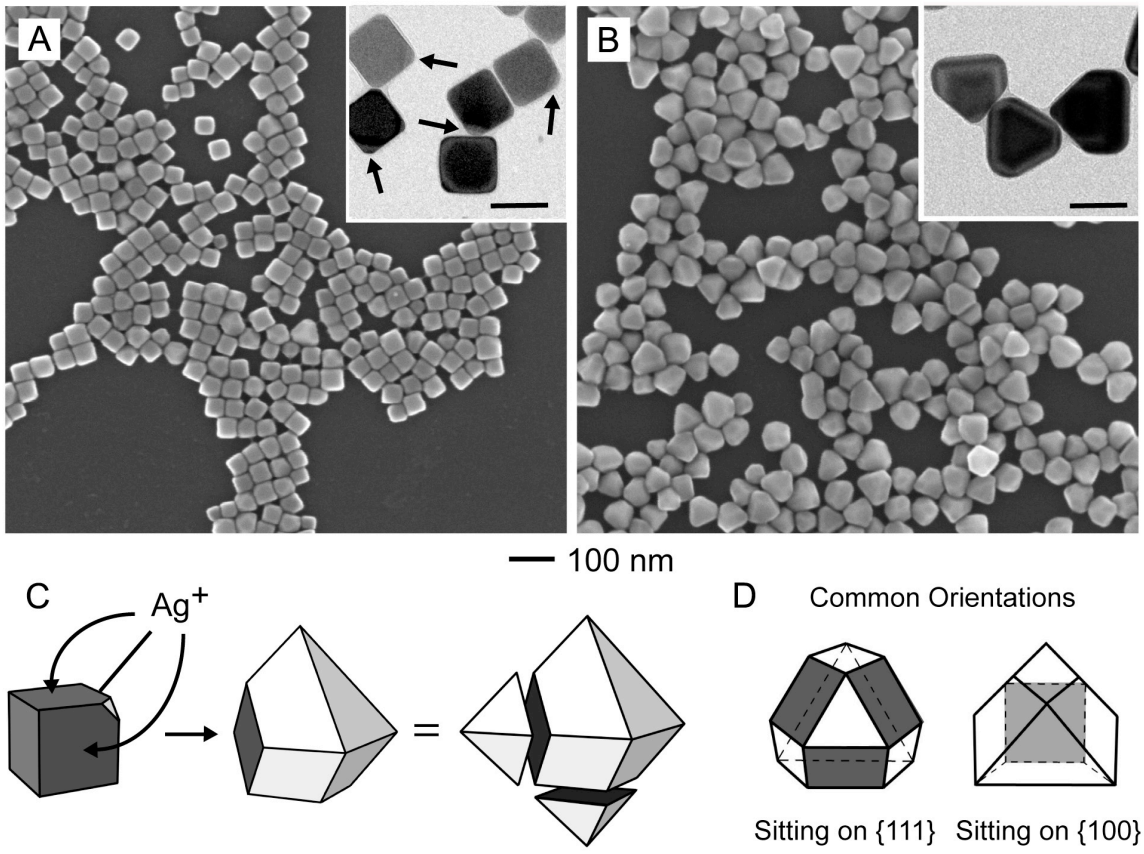

Figure 2.4. When a second aliquot of $AgNO_3$ was introduced at the end of a sulfide-mediated polyol synthesis, the Ag nanocubes evolved into a new anisotropic structure rapidly: (A, B) SEM images with TEM insets of the product (A) before and (B) 10 min after introduction of additional $AgNO_3$ (scale bars in the insets: 50 nm). The arrows indicate the corners of nanocubes that had been truncated due to oxidative etching. (C) A proposed mechanism for this transformation. Silver ions are reduced more rapidly on three {100} faces adjacent to the truncated corner, leading to the formation of an anisotropically-truncated octahedron. For comparison, an octahedron is also shown with three of the corners removed. Note that the third detached corner is not visible at this orientation. White and grey denote {111} and {100} facets, respectively. (D) The two most common orientations of the anisotropically-truncated octahedron on a flat substrate, as viewed from above.

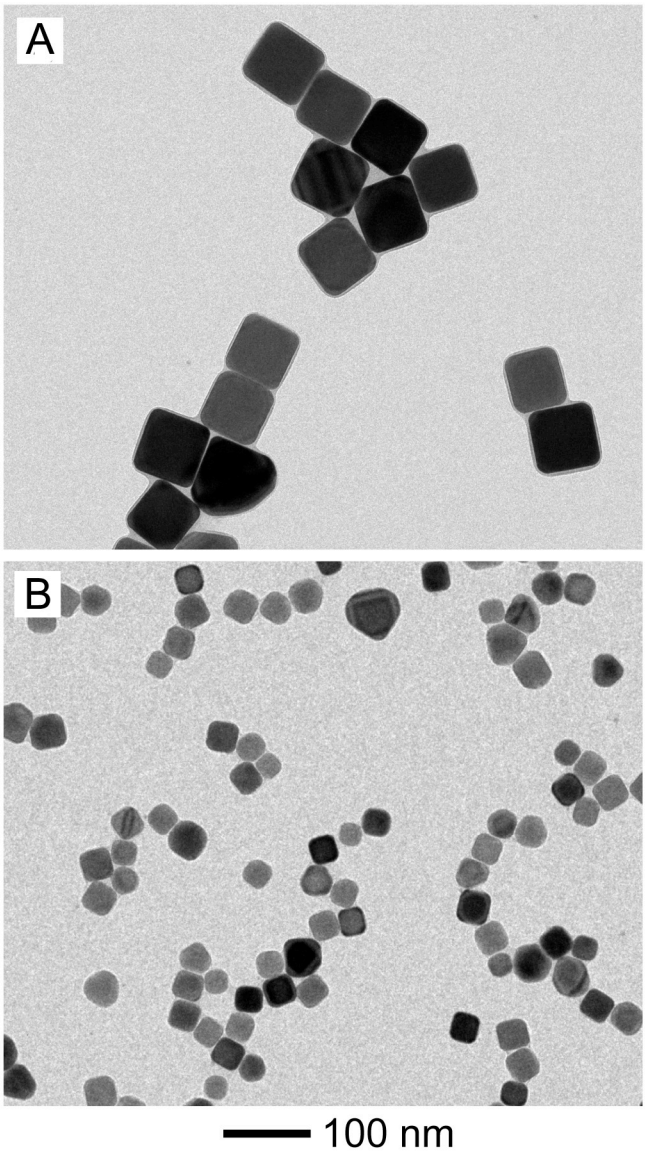

Figure 2.5. Control experiments. (A) TEM image of the final product when additional $AgNO_3$ was added at a 15x slower rate (0.05 mL/minute). (B) TEM image of the final product when additional $AgNO_3$ was added to an Ar-saturated and Ar-protected synthesis. These final cubes were a few nm larger than the original cubes.

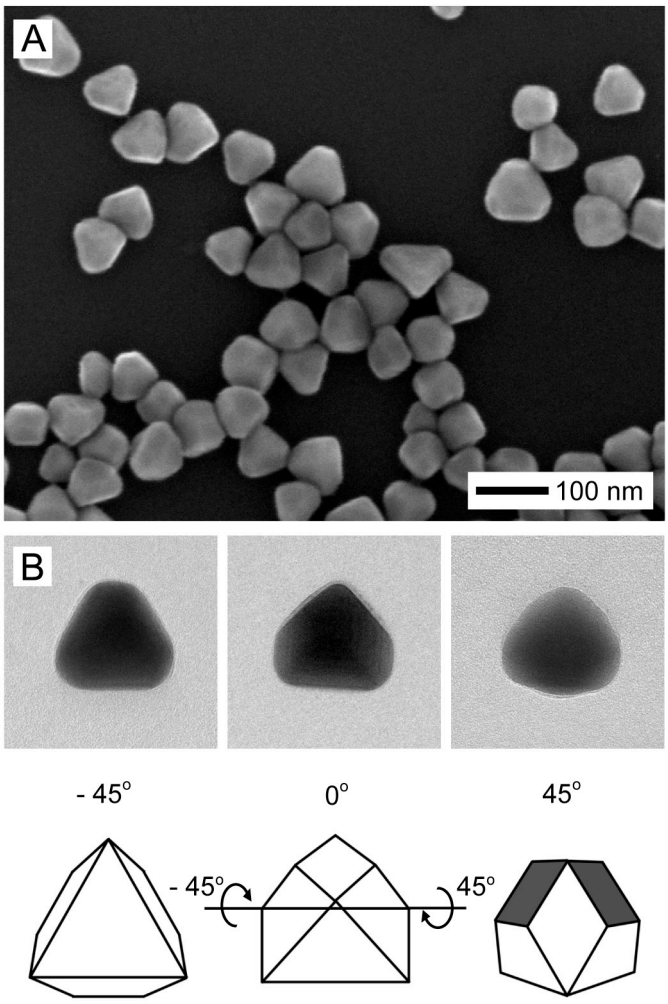

Figure 2.6. (A) A high-magnification SEM image of the anisotropically-truncated octahedrons of Ag with well-developed facets. (B) TEM images taken from a single anisotropically-truncated octahedron at three different tilting angles and images of a model which has been tilted the same amount (the direction is indicated by the circular arrows). White and grey signify {111} and {100} facets, respectively.

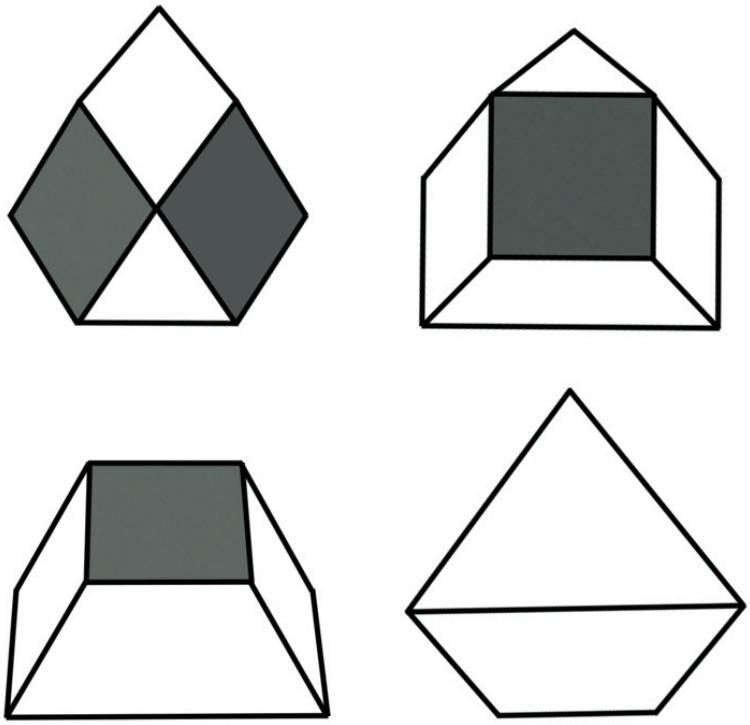

Figure 2.7. Additional orientations of the anisotropically-truncated octahedron, as viewed from above. Particles with these orientations are not sitting on a flat face, and consequently represent only a small portion of the particles in the SEM and TEM micrographs. Grey signifies {100} facets and white signifies {111} facets.

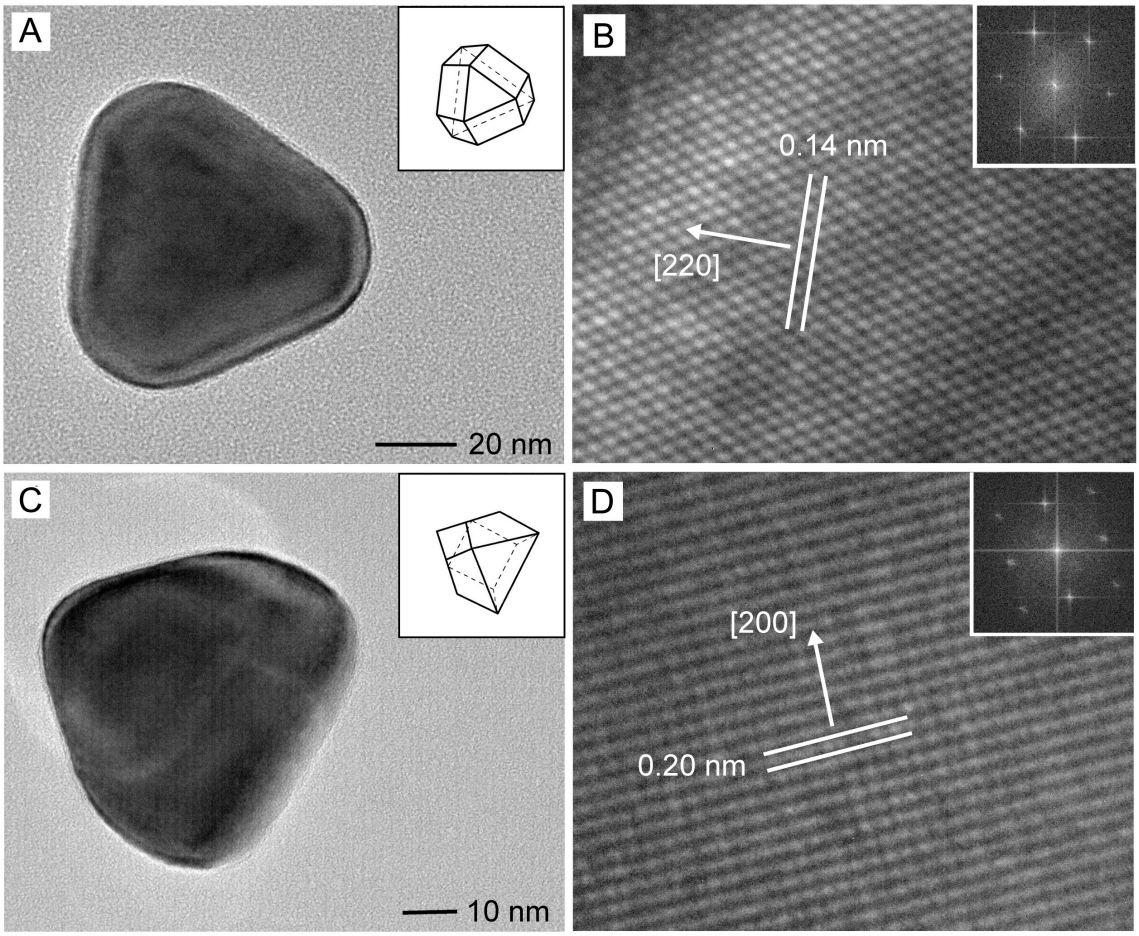

Figure 2.8. High-resolution TEM analysis of the two orientations typically observed, with the anisotropically-truncated octahedron sitting on a (A, B) triangular, {111} face and (C, D) square, {100} face. Insets for (A) and (C) are models of the anisotropically-truncated octahedron at that orientation, and for (B) and (D) are fast Fourier transform (FFT) patterns of the high-resolution TEM images, respectively.

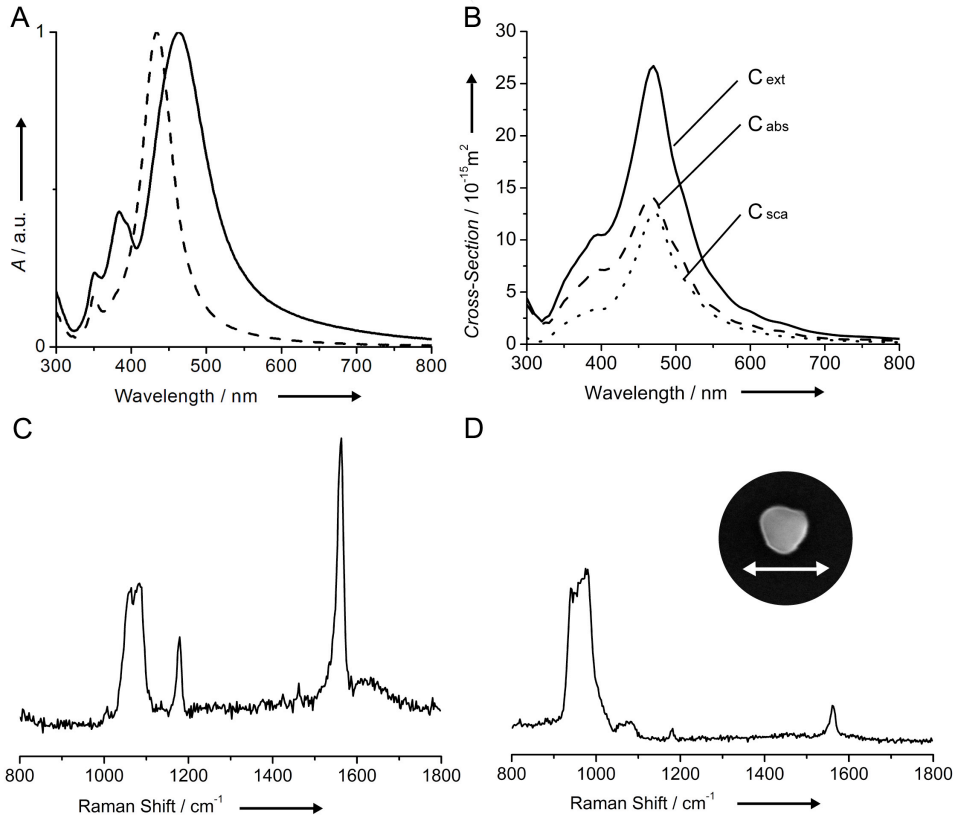

Figure 2.9. (A) Normalized UV-vis spectra of aqueous suspensions of the Ag nanocubes (dashed) and the corresponding product of anisotropically-truncated octahedrons (solid). (B) DDA calculations of the extinction (solid), absorption (dashed), and scattering (dotted) coefficients for an anisotropically-truncated octahedron suspended in water with random orientations. The sharp corners were snipped by 11.7 nm to reflect the slightly truncated nature to provide a better fit with the experimental data. (C) Solution phase SERS spectrum of 1,4-BDT adsorbed onto the surface of the anisotropically-truncated octahedrons. The overlapping peaks at 1067 cm^{-1} and 1085 cm^{-1} are attributed to the fundamental benzene ring breathing mode 1, the peak at 1182 cm^{-1} is attributed to the 9a ring breathing vibration, and the peak at 1563 cm^{-1} is attributed to the 8a ring breathing vibration. (D) Single particle SERS spectrum of 1,4-BDT adsorbed on the anisotropically-truncated octahedron shown in the inset. In addition to the peaks seen in c, a broad peak just below 1000 cm^{-1} is visible, which can be ascribed to the silicon substrate. The polarization direction is indicated by the white arrow.

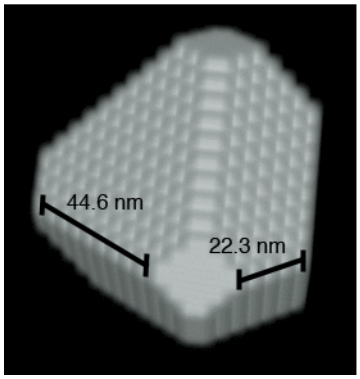

Figure 2.10. Model used in DDA calculations. The 44.6 nm edge length marked results from a 68 nm edge having two 11.7 nm segments removed at either end.

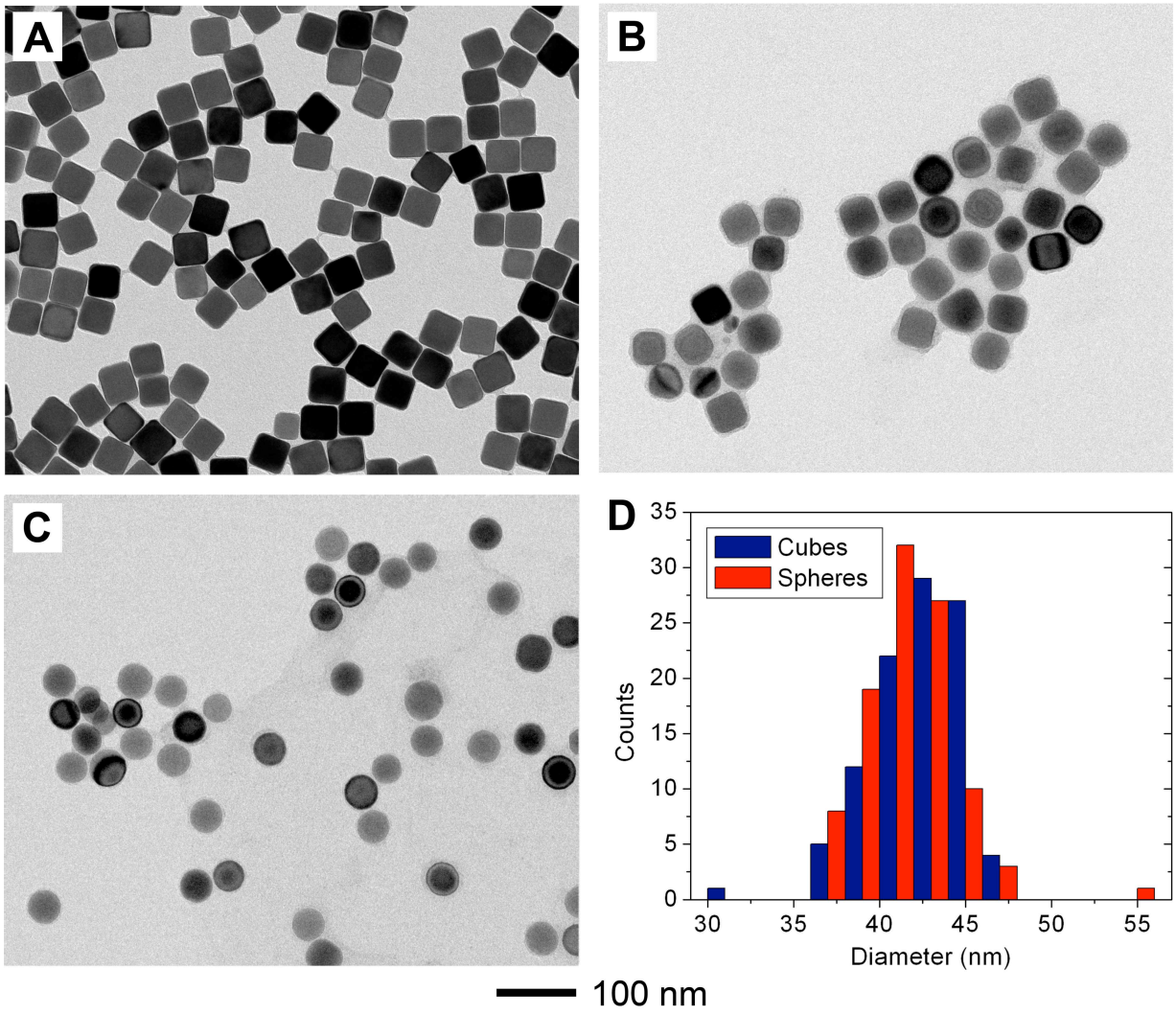

Figure 2.11. TEM images (A-C) of 42-nm Ag cubes capped with PVP when etched with different volumes of 0.5 mM ferric nitrate: (A) 0 μL, (B) 10 μL, and (C) 100 μL. (D) Size distributions calculated from 100 particles in (A) and (C).

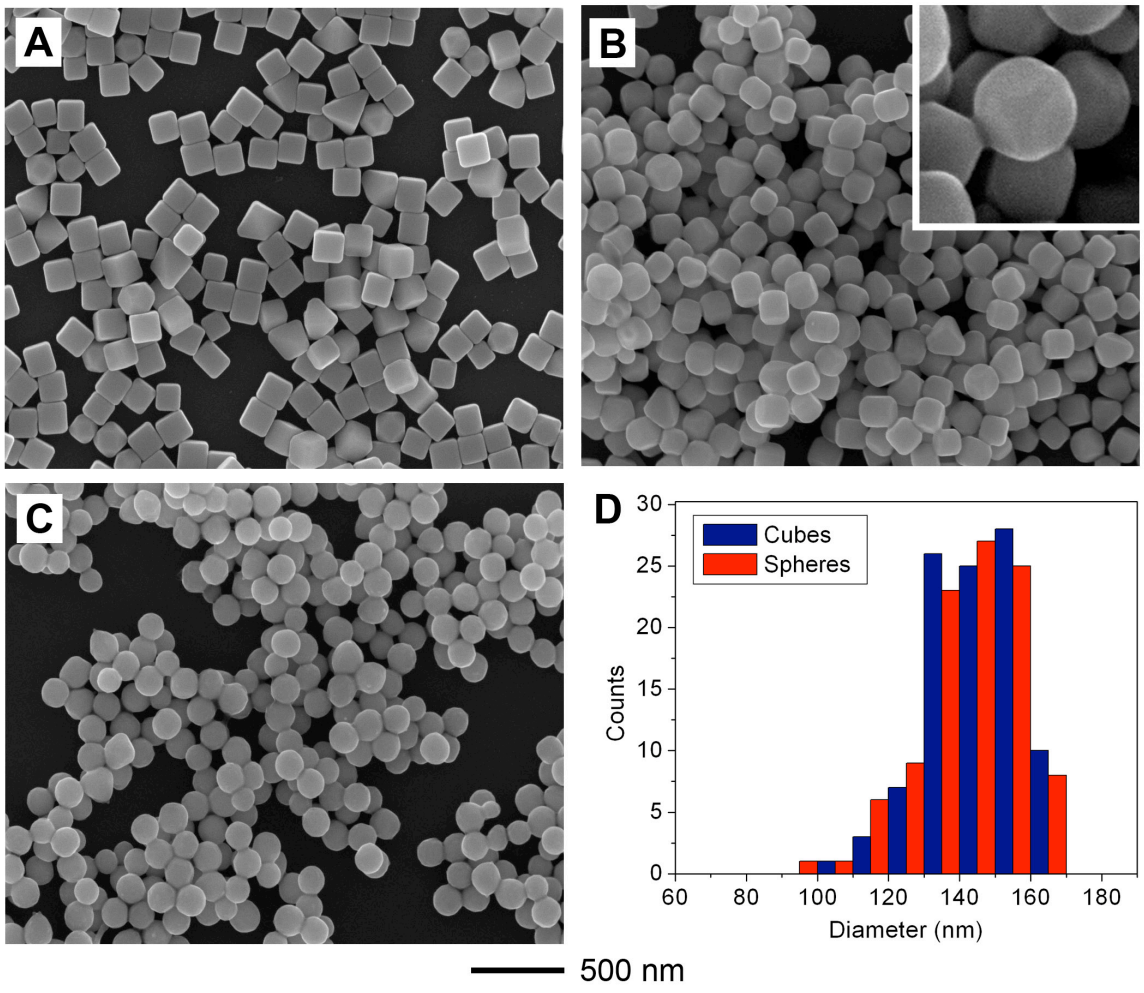

Figure 2.12. SEM images (A-C) of 144-nm Ag cubes capped with PVP when etched with different volumes of a ferricyanide etching solution: (A) 0 μL, (B) 5 μL, and (C) 20 μL. The inset in (B) shows that both the edges and the corners of the cubes were rounded during the etching process. (D) Size distributions calculated from 100 particles in (A) and (C).

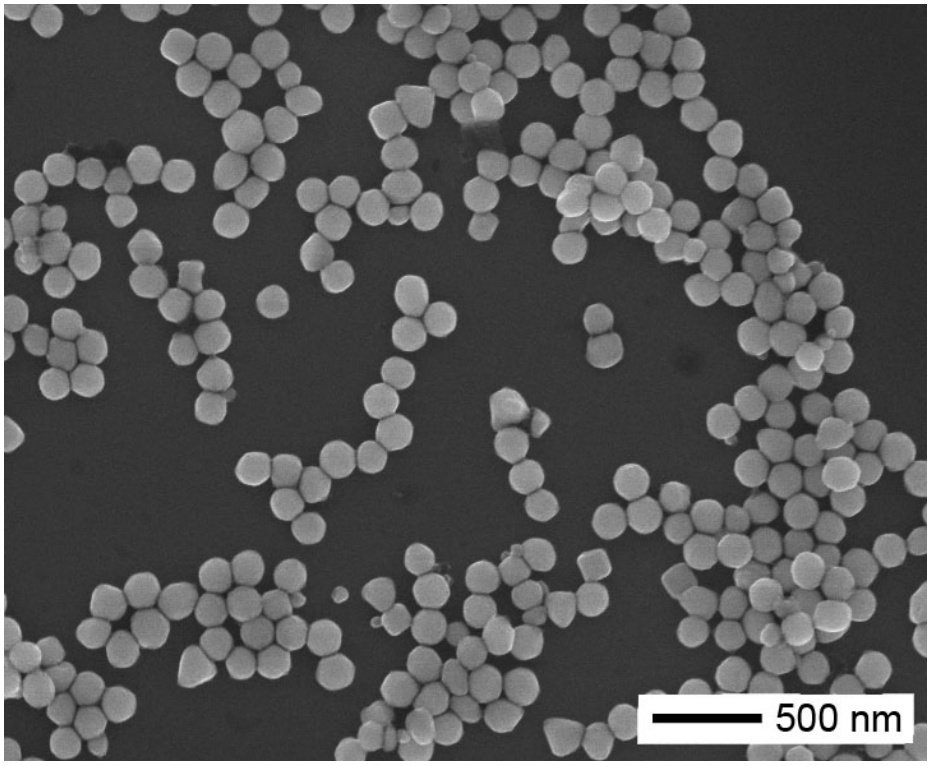

Figure 2.13. Large, 144-nm Ag nanocubes protected with PVP after etching with 75 μL of 5 mM ferric nitrate. The profile was not as uniform and smooth as with the ferricyanide etchant.

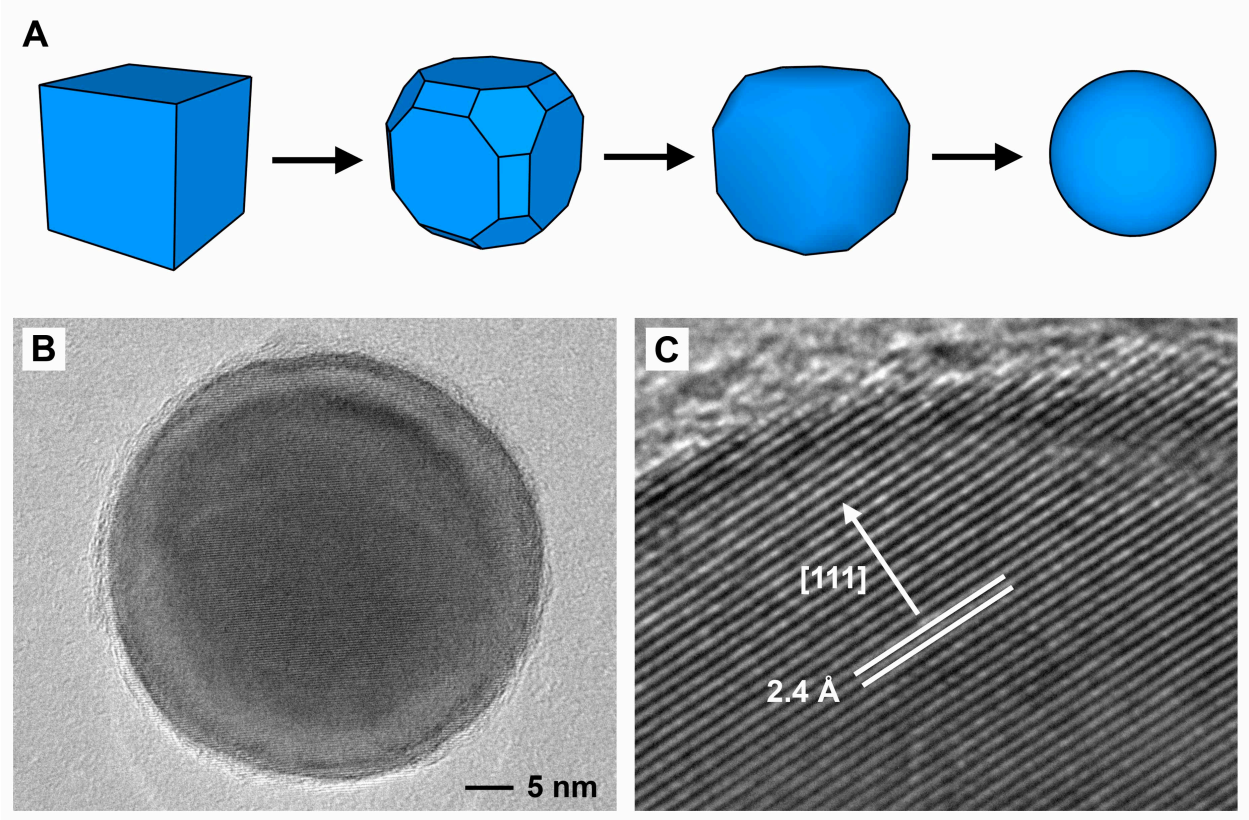

Figure 2.14. (A) Schematic showing the transformation of a sharp cube into a sphere by truncation of all sharp edges and corners. (B) High-resolution TEM image of a single-crystal Ag sphere of 42 nm in diameter. (C) Higher magnification image of the nanosphere in (B), showing 2.4 Å lattice fringes, which corresponds to the {111} spacing of Ag.

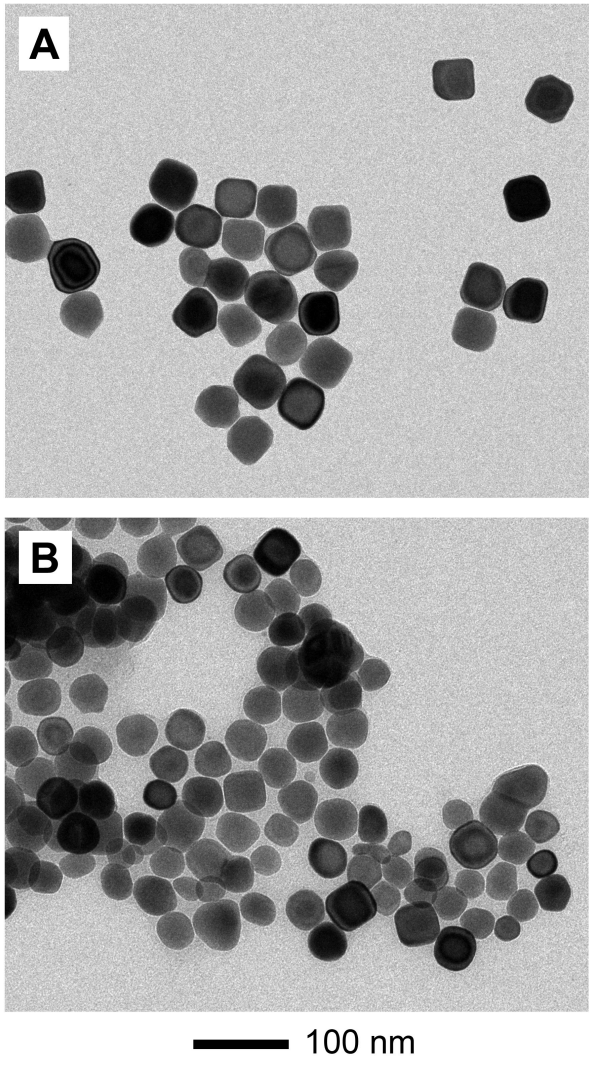

Figure 2.15. TEM images of PVP-capped 42-nm Ag nanocubes after being etched with two weaker etchants: (A) 20 μL of a 1:1 mixture of 3% ammonium hydroxide and 3% hydrogen peroxide, and (B) 25 μL of 30% ammonium hydroxide.

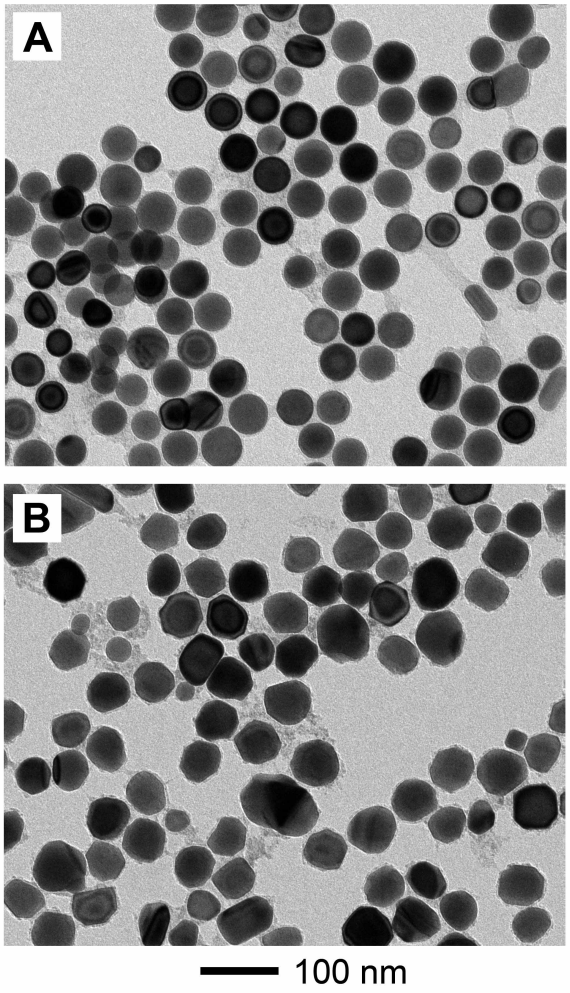

Figure 2.16. Morphological transformation of 54-nm cubes protected with PVP after etching with ferric nitrate under different stirring conditions: (A) 15 s of vortex mixing followed by a 10 min pause, (B) 10 min on stir plate at 300 rpm.

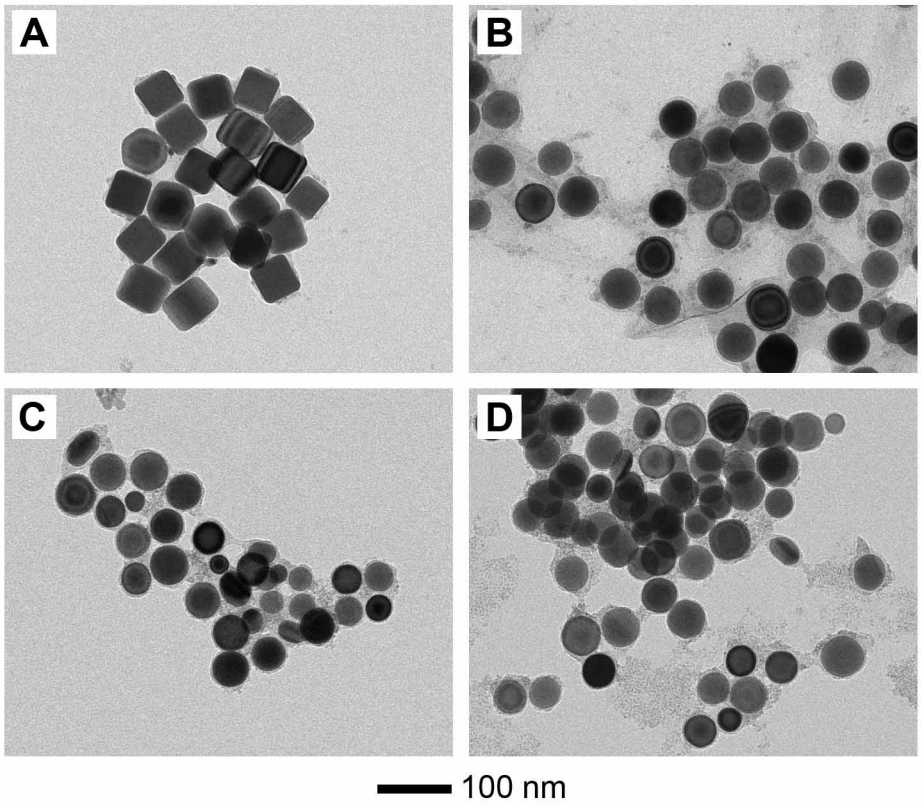

Figure 2.17. Etching of cubes with protection from different surface capping agents: (A) 6-mercapto-1-hexanol, (B) 2-mercaptoethanol, (C) 6-amino-1-hexanol, and (D) 6-hydroxycaprioic acid.

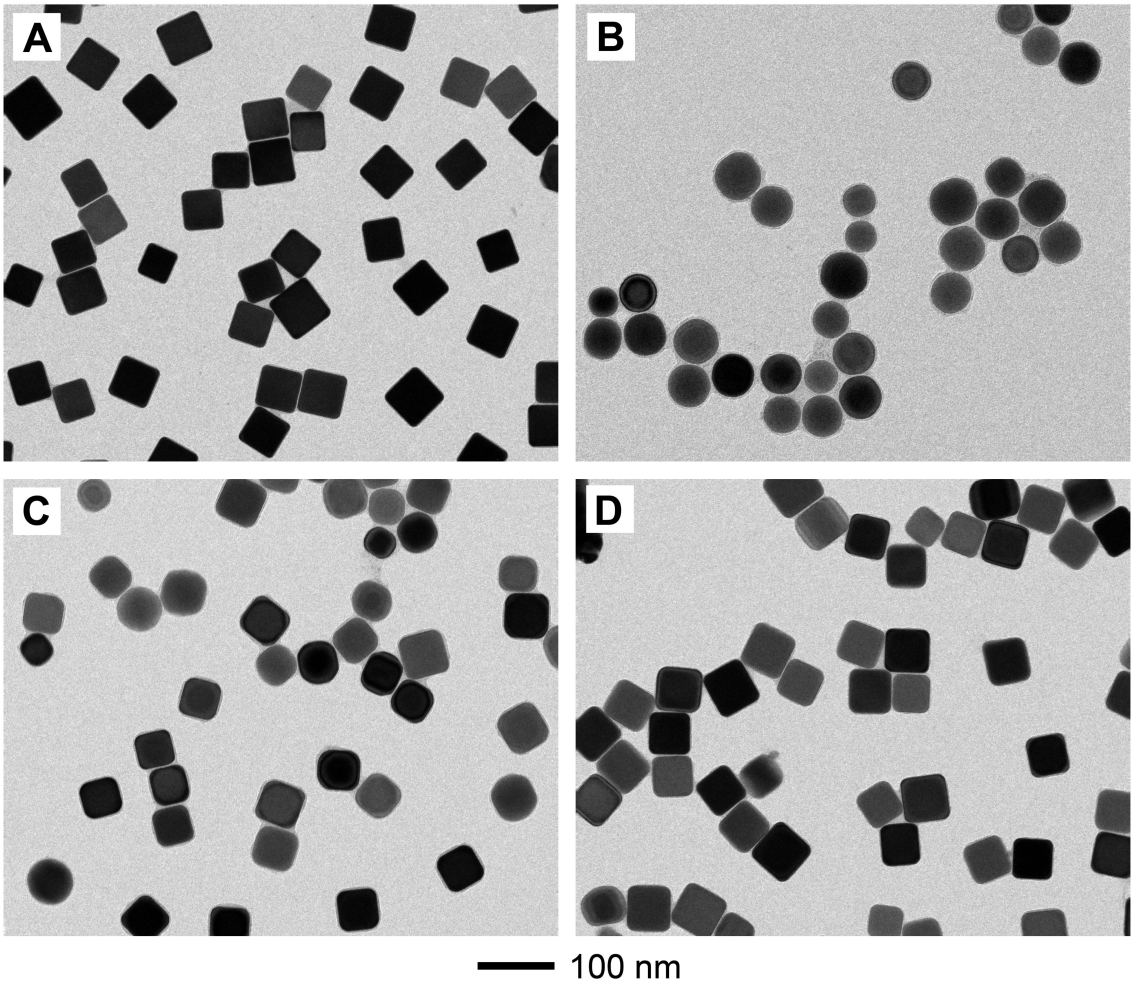

Figure 2.18. TEM images of 54-nm cubes (A) that had been etched into spheres (B) with ferric nitrate using the same method as in Figure 2.11 and then re-grown into rounded (C) and sharp (D) cubes through the addition of different volumes of 0.1 mg/mL $AgNO_3$ into a pre-heated ethylene glycol solution in the presence of PVP at 0.05 mL/min: (C) 1.00 mL and (D) 1.50 mL.

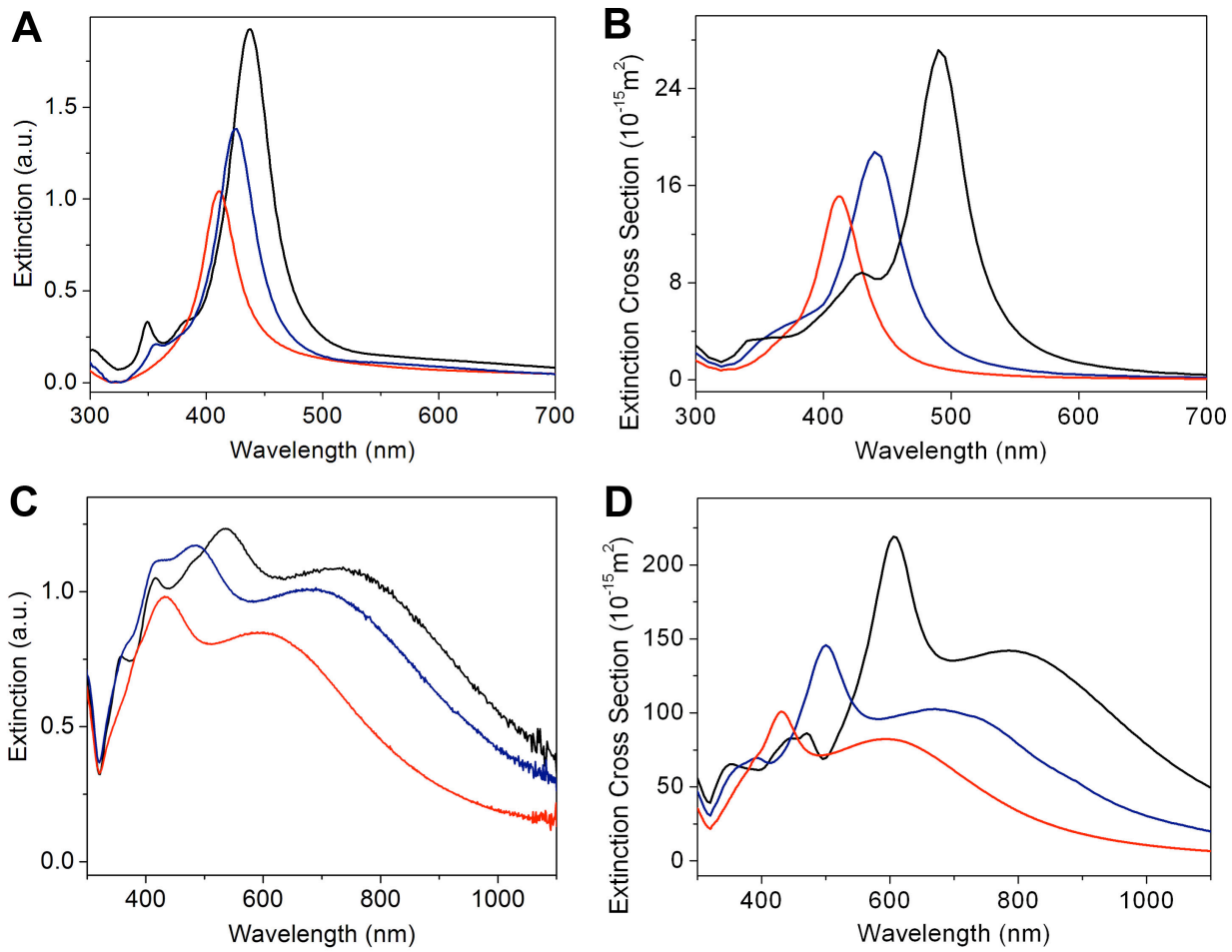

Figure 2.19. UV-Vis spectra of (A) 42-nm and (C) 144-nm Ag nanoparticles with different levels of rounding suspended in water. Mie theory (spheres) and DDA (cubes and truncated cubes) calculations for (B) 42 nm and (D) 144 nm Ag nanoparticles suspended in water, simulating the etching shown in Figures 2.11 and 2.12. Black lines indicate sharp cubes, blue lines indicate rounded cubes, and red lines indicate spheres. For the rounded cubes, both the edges and corners of the cubes were truncated, as shown in Figure 2.20.

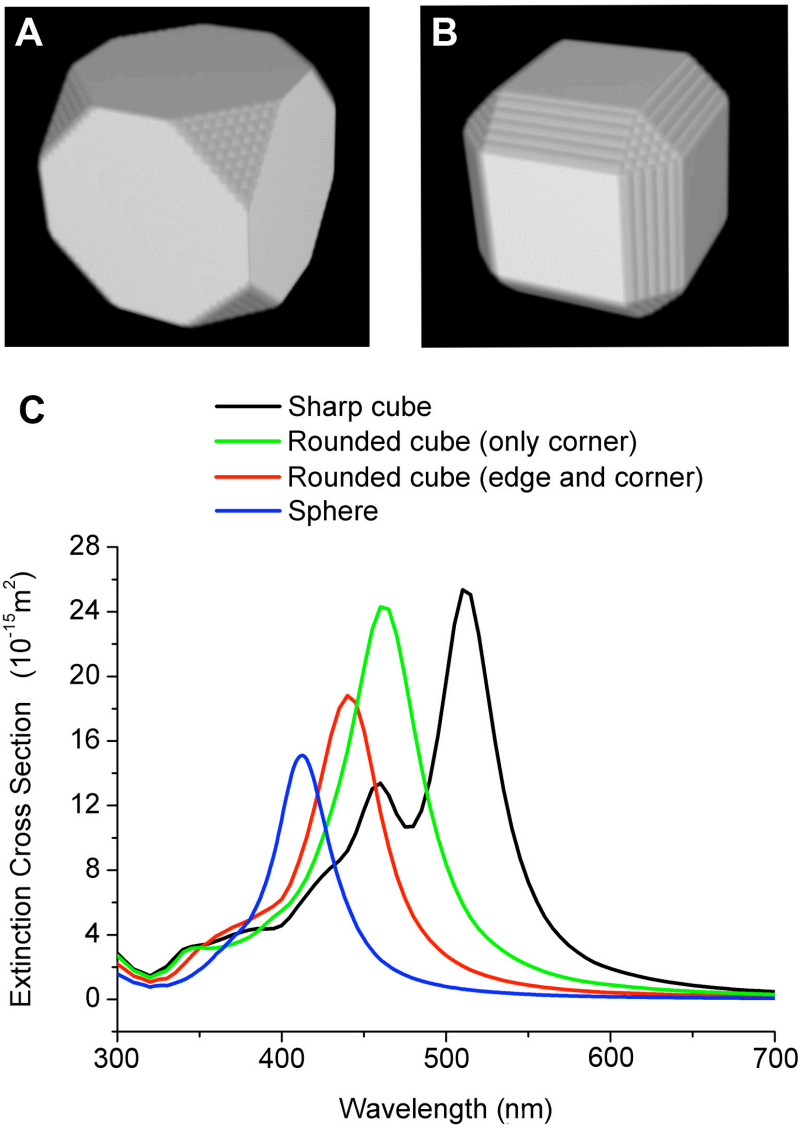

Figure 2.20. Comparison of DDA spectra with different methods of truncation: (A) model showing corners only truncation, (B) model showing corner and edge truncation (C) comparison of calculated spectra shown in Figure 2.19 (sharp cubes: black, rounded cubes: red, and spheres: blue) and a cube that is only rounded at the corners (green).

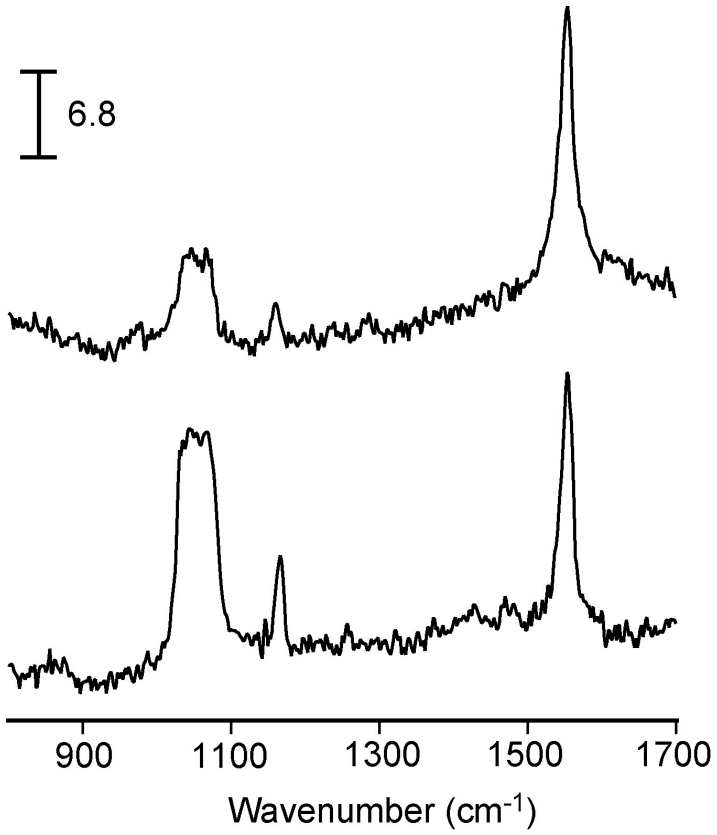

Figure 2.21. Representative solution phase SERS spectra of 1,4-BDT taken from suspensions of 142 nm spheres (top trace) and 25 nm spheres (bottom trace). The 142 nm spheres were found to have an enhancement factor of 1.0×10^5 while the 25 nm spheres only had an enhancement factor of 8.9×10^3, as calculated with the 8a ring breathing vibration at 1563 cm^{-1}. The overlapping peaks at 1067 cm^{-1} and 1085 cm^{-1} are attributed to the fundamental benzene ring breathing mode 1 and the peak at 1182 cm^{-1} is attributed to the 9a ring breathing vibration. The scale bar is in adu mW^{-1} s^{-1} and applies to both spectra.

2.6. References for Chapter 2

[1] Pyayt, A. L.; Wiley, B.; Xia, Y.; Chen, A.; Dalton, L. *Nature Nanotech.* **2008**, *3*, 660.

[2] Rosi N. L. and Mirkin C. A., *Chem. Rev.* **2005**, *105*, 1547.

[3] Alivisatos, A. P. *Nat. Biotechnol.* **2004**, *22*, 47.

[4] Kneipp, K., Kneipp, H., Itzkan, I., Dasari, R. and Feld, M. *Chem. Rev.* **1999**, *99*, 2957.

[5] Nie, S.; Emory, S. *Science* **1997**, *275*, 1102.

[6] (a) Wiley B. J., Im, S. H., Li, Z.-Y., McLellan, J., Siekkinen, A. R., Xia, Y. *J. Phys. Chem. B* **2006**, 110, 15666. (b) Kelly, K.; Coronado, E.; Zhao, L.; Schatz, G. *J. Phys. Chem. B* **2003**, 107, 668.

[7] (a) Quinten, M. *Appl. Phys. B*. **2001**, *73*, 245., (b) Yguerabide, J.; Yguerabide, E. E. *Anal. Biochem.* **1998**, *262*, 137.

[8] Cobley, C. M.; Skrabalak, S. E.; Campbell, D. J.; Xia, Y. *Plasmonics* **2009**, *4*, 171.

[9] Kreibig, U.; Vollmer, M. *Optical Properties of Metal Clusters*; Springer Series in Material Science 25; Springer: Berlin, **1995**.

[10] Ferraro, J. R.; Nakamoto, K.; Brown, C. W. *Introductory Raman Spectroscopy*; Academic Press, Elsevier Science, **2003**.

[11] Ru, E. L.; Etchegoin, P. Principles of Surface Enhanced Raman Spectroscopy Elsevier **2009**.

[12] (a) Moskovits, M. J. Raman Spectrosc. **2005**, 36, 485. (b) Haynes, C. L.; McFarland, A. D.; Duyne, R. P. V. *Anal. Chem.* **2005**, *77*, 338A.

[13] Haynes, C.; Yonzon, C.; Zhang, X.; Duyne, R. V. *J Raman Spectrosc.* **2005**, *36*, 471.

[14] Grubisha, D. S.; Lipert, R. J.; Park, H.-Y.; Driskell, J.; Porter, M. D. *Anal. Chem.* **2003**, *75*, 5936.

[15] Xia, Y.; Xiong, Y.; Lim, B.; Skrabalak, S. E. *Angew. Chem. Int. Ed.* **2009**, *48*, 60.

[16] Tao, A.; Sinsermsuksakul, P.; Yang, P. *Angew. Chem. Int. Ed.* **2006**, *45*, 4597.

[17] McLellan, J.; Siekkinen, A. R.; Chen, J.; Xia, Y. *Chem. Phys. Lett.* **2006**, *427*, 122.

[18] Draine, B.; Flatau, P. *J. Opt. Soc. Am. B* **1994**, *11*, 1491.

[19] Sherry, L. J.; Chang, S. H.; Schatz, G. C.; Duyne, R. P. V.; Wiley, B. J.; Xia, Y. *Nano Lett.* **2005**, *5*, 2034.

[20] McLellan, J.; Li, Z.-Y.; Siekkinen, A.; Xia, Y. *Nano Lett.* **2007**, *7*, 1013.

[21] Camargo, P. H. C.; Rycenga, M.; Au, L.; Xia, Y. *Angew. Chem. Int. Ed.* **2009**, *48*, 2180.

[22] Wiley, B. J.; Xiong, Y.; Li, Z.-Y.; Yin, Y.; Xia, Y. *Nano Lett.* **2006**, *6*, 765.

[23] Rycenga, M.; Hou, K. K.; Cobley, C. M.; Schwartz, A.; Camargo, P. H. C.; Xia, Y. *Phys. Chem. Chem. Phys.* **2009**, *11*, 5903.

[24] Yin, Y.; Li, Z.-Y.; Zhong, Z.; Gates, B.; Xia, Y.; Venkateswaran, S. J. *Mater. Chem.* **2002**, *12*, 522.

[25] Kim, D., Jeong, S., Moon, J. *Nanotechnol*. **2006**, *17*, 4019.

[26] Wiley, B. J.; Herricks, T.; Sun, Y.; Xia, Y. *Nano Lett.* **2004**, 4, 1733.

[27] Rycenga, M., Kim, M. H., Camargo, P. H. C., Cobley, C. M., Li, Z.-Y., Xia, Y. *J. Phys. Chem. A* **2009**, *113*, 3932.

[28] Li, W., Camargo, P. H. C., Lu, X., Xia, Y. Nano Lett. **2009**, *9*, 485.

[29] Rycenga, M.; Camargo, P. H. C.; Li, W.; Moran, C. H.; Xia, Y. *J. Phys. Chem. Lett.* **2010**, *1*, 696.

[30] Wiley, B.; Chen, Y.; McLellan, J.; Xiong, Y.; Li, Z.-Y.; Ginger, D.; Xia, Y. *Nano Lett.* **2007**, *7*, 1032.

[31] Murphy, C.; Sau, T.; Gole, A.; Orendor *J. Phys. Chem. B* **2005**, *109*, 13857.

[32] Skrabalak, S. E.; Wiley, B. J.; Kim, M.; Formo, E.; Xia, Y. *Nano Lett.* **2008**, *8*, 2077.

[33] Smith, D. J.; Petford-Long, A. K.; Wallenberg, L. R.; Bovin, J. O. *Science* **1986,** *233*, 872.

[34] Iijima, S.; Ichihashi, T. Phys. Rev. Lett **1986**, *56*, 616.

[35] Wiley, B. J.; Xiong, Y.; Li, Z.-Y.; Yin, Y.; Xia, Y. *Nano Lett.* **2006**, *6*, 765.

[36] Wiley, B. J.; Sun, Y.; Xia, Y. *Langmuir* **2005**, *21*, 8077.

[37] Siekkinen, A. R.; McLellan, J. M.; Chen, J.; Xia, Y. *Chem. Phys. Lett.* **2006**, *432*, 491.

[38] Skrabalak, S. E.; Au, L.; Li, X.; Xia, Y. Nat. Protoc. **2007**, *2*, 2182.

[39] Kryukov, A.; Zinchuk, N.; Korzhak, A.; Kuchmii, S. Theor. Exp. Chem. **2001**, *37*, 355.

[40] Kryukov, A.; Stroyuk, A.; Zinchuk, N.; Korzhak, A.; Kuchmii, S. J. Mol. Cat. **2004**, *221*, 209.

[41] Zhang, Q.; Cobley, C.M., Au, L.; McKiernan, M.; Schwartz, A.; Wen, L.-P.; Chen, J.; Xia, Y. *ACS Appl. Mater. Chem*. **2009**, *9*, 2044.

[42] Sun, Y.; Mayers, B.; Herricks, T.; Xia, Y. *Nano Lett.* **2003***, 3*, 955.

[43**]** Zeng, J.; Zheng, Y.; Rycenga, M.; Tao, J.; Li, Z.-Y.; Zhang, Q.; Zhu, Y.; Xia, Y. *J. Am. Chem. Soc*. **2010**, *132*, 8552.

[44] (a) Lim, B.; Lu, X.; Jiang, M.; Camargo, P. H. C.; Cho, E. C.; Lee, E. P.; Xia, Y. *Nano Lett.* **2008**, *8*, 4043. (b) Fan, F.-R.; Liu, D.-Y.; Wu, Y.-F.; Duan, S.; Xie, Z.-X.; Jiang, Z.-Y.; Tian, Z.-Q. *J. Am. Chem. Soc.* **2008**, *130*, 6949. (c) Seo, D.; Yoo, C. I.; Jung, J.; Song, H. *J. Am. Chem. Soc.* **2008**, *130*, 2940.

[45] Habas, S. E.; Lee, H.; Radmilovic, V.; Somorjai, G. A.; Yang, P. *Nat Mater* **2007**, *6*, 692.

[46] Seo, D.; Yoo, C. I.; Park, J. C.; Park, S. M.; Ryu, S.; Song, H. *Angew. Chem. Int. Ed.* **2008**, *47*, 763.

[47] Cobley, C. M.; Rycenga, M.; Zhou, F.; Li, Z.-Y.; Xia, Y. *Angew. Chem. Int. Ed.* **2009**, *48*, 4824.

[48] Xiong, Y.; Cai, H.; Wiley, B. J.; Wang, J.; Kim, M. J.; Xia, Y. *J. Am. Chem. Soc.* **2007**, *129*, 3665.

[49] (a) Xiong, Y.; Wiley, B. J.; Chen, J.; Li, Z.-Y.; Yin, Y.; Xia, Y. *Angew. Chem. Int. Ed.* **2005**, *44*, 7913. (b) Kuo, C.-H.; Huang, M. H. *J. Am. Chem. Soc.* **2008**, *130*, 12815.

[50] Lu, X.; Au, L.; McLellan, J.; Li, Z.-Y.; Marquez, M.; Xia, Y. *Nano Lett.* **2007**, *7*, 1764.

[51] (a) An, J.; Tang, B.; Zheng, X.; Zhou, J.; Dong, F.; Xu, S.; Wang, Y.; Zhao, B.; Xu, W. *J. Phys. Chem. C* **2008**, *112*, 15176. (b) Jana, N.; Gearheart, L.; Obare, S.; Murphy, C. *Langmuir* **2002**, *18*, 922.

[52] Xia, Y.; Zhao, X.; Kim, E.; Whitesides, G. *Chem. Mater.* **1995**, *7*, 2332.

[53] Xia, Y.; Kim, E.; Whitesides, G. *J. Electrochem. Soc.* **1996**, *143*, 1070.

[54] Im, S. H.; Lee, Y. T.; Wiley, B. J.; Xia, Y. *Angew. Chem. Int. Ed.* **2005**, *44*, 2154.

[55] Zhang, Q.; Li, W.; Wen, L.-P.; Chen, J.; Xia, Y. *Chem. Eur. J.* **2010**, *16*, 10234.

[56] Zhang, Q.; Li, W.; Moran, C.; Zeng, J.; Chen, J.; Wen, L.-P.; Xia, Y. *J. Am. Chem. Soc.* **2010**, *132*, 11372.

[57] (a) Kondo, K.; Kurihara, H.; Murakami, H. *Electrochem. Solid-State Lett.* **2006**, *9*, C36. (b) Lee, D. *J. App. Phys.* **1969**, *40*, 4569. (c) Bean, K. *IEEE Trans. Electron. Devices* **1978**, *25*, 1185.

[58] Randle, T. *J. Chem. Educ.* **1994**, *71*, 261.

[59] (a) Love, J.; Estroff, L.; Kriebel, J.; Nuzzo, R.; Whitesides, G. *Chem. Rev* **2005**, *105*, 1103. (b) Xia, Y. and Whitesides, G. *Annu. Rev. Mater. Sci.* **1998**, *28*, 153.

[60] Li, W.; Virtanen, J.; Penner, R. *Langmuir* **1995**, *11*, 4361.

[61] Zhou, F.; Li, Z.-Y.; Liu, Y.; Xia, Y. *J. Phys. Chem. C* **2008**, *112*, 20233.

[62] Fuchs, R. *Phys. Rev. B* **1975**, *11*, 1732.

Chapter 3

Galvanic Replacement as a Route to Complex Nanostructures

3.1. Introduction

As discussed in Chapter 2, significant progress has been made in recent years in shape-controlled synthesis of solid, single component metal nanostructures.[1-4] However, researchers have also invested significant efforts in developing methods for producing nanostructures with greater structural and compositional complexity.[5-7] These novel structures are interesting for applications in areas such as plasmonics and catalysis due to the strong effect of geometry on the localized surface plasmon resonance (LSPR) of metallic nanostructures,[8-10] the high surface areas possible with unusual geometries (such as hollow, porous, or dendritic structures),[11,12] and the synergetic effects that can occur in bimetallic catalysts.[13-15]

Of the many techniques that have been demonstrated, galvanic replacement is particularly interesting due to its simplicity, versatility, and its use to probe the intricacies of alloying and dealloying in metallic nanostructures.[16,17] Galvanic replacement occurs spontaneously when atoms of a metal react with ions of another metal having a higher electrochemical potential in the solution phase. The metal atoms are oxidized and dissolved into the solution, while the metal ions are reduced and plated on the surface of the metal template. This simple reaction can be used with a wide variety of metal

templates and salt precursors and is limited by little more than the requirement of an appropriate difference in the electrochemical potentials between the two metals. Based on fundamental chemistry, this reaction provides a straightforward route to a broad range of simple and complex structures including hollow nanocrystals, alloyed nanostructures with controllable elemental compositions, and nanoparticles with tunable optical properties.[16,17] A number of different factors can be manipulated to engineer the final morphologies and properties of the resultant structures, including the crystallinity of the template, the salt precursor(s), and the presence of different crystallographic facets on the surface of the template.[18-23]

One type of study that has been critical to achieving this high degree of control is performing the galvanic replacement reaction with a variety of templates. Previous studies have investigated templates such as polycrystalline nanoparticles, single-crystal Ag nanospheres, Ag nanocubes, and truncated Ag nanocubes with multiple crystallographic facets on the surface.[17-20] In Section 3.2 I will discuss the reaction with Ag nanocubes (i.e. the production of Au-Ag nanocages) as an introduction to the fundamentals of this reaction and background for the applications of Au-Ag nanocages discussed in Chapter 4.

However, while such initial studies have made it possible to create plasmonic nanostructures with interesting properties for biomedical applications, certain fundamental investigations were out of reach due to the lack of availability of less symmetric nanocrystals. For example, in a highly symmetric nanocrystal, the crystallographically equivalent facets are often identical in area and shape, making it

difficult to examine if there is any effect from these parameters. Another limitation with the highly symmetric substrates used in previous studies is that specific crystal facets are typically located in the same region of a particle, making it difficult to separate out the effects of facet crystallographic packing and facet location. For example, in Ag nanocubes, {100} facets are always located on the large, flat side faces, {111} facets occur only in truncated corner regions, and {110} facets occur only if the sharp edges of the cube are rounded.[20] The high curvature of corner and edge regions could influence their reactivity, especially if the corners were truncated using etching. While other geometries, such as octahedra, may have different facet configurations, the different synthetic methods (particularly the different capping agents) used to create each type of particle will influence the surface chemistry and facet reactivity.[12] For this reason, it is more desirable to study a single type of particle with an asymmetric geometry, where the same type of crystal facet is located in different areas of the particle.

As discussed in Chapter 2, recent advances in the synthesis of Ag nanostructures have made it possible to create structures with low symmetry, non-uniform surfaces, and well-defined facets.[24] In Section 3.3, I will discuss how I took advantage of these developments to investigate the effects of asymmetric geometries and facet shape in galvanic replacement reactions, and to investigate more fully the effect of facet crystallographic packing on pore formation. I did so by examining the galvanic replacement reaction with two Ag structures having non-uniform surfaces: asymmetrically truncated octahedrons (ATOs) and nanobars.

In addition to the choice of template particle, the next most common way to

control the product of a galvanic replacement reaction is by manipulating the metal precursor used in the titration. Both the identity and the valency of the metal precursor can have strong effects. For example, while titrating with an Au(III) salt will produce thin-walled nanocages with numerous small pores, titrating with an Au(I) salt will produce nanoframes with robust edges and empty sides.[21,22] The composition and morphology of the resulting structures will also change if precursors of different metals are used, such as Na_2PdCl_4 or Na_2PtCl_4, as the alloying and dealloying abilities of these precursors are different from those of $HAuCl_4$.

In Section 3.3, I will compare the galvanic replacement reaction of Ag nanocubes with $HAuCl_4$, Na_2PdCl_4, and a combination of the two precursors. I am particularly interested in the combined system due to the catalytic potential of this system. Palladium-based nanostructures are attractive for a number of catalytic applications and have been demonstrated in a variety of reactions that include Heck coupling,[25] Suzuki coupling,[26] and hydrogenation.[27] However, it has been noted by many groups that bimetallic catalysts often show enhanced performance when compared to each individual metal.[13,28] For instance, Pd-Au bimetallic systems have been shown to exhibit enhanced catalytic activity for multiple reactions including the hydrodechlorination of trichloroethene,[13,28,29] and Pd-Ag bimetallic catalysts have also been shown to have enhanced selectivity in the hydrogenation of hexa-1,5-diene.[29] Since the ratio between the two metals was found to be an important factor in determining the magnitude of enhancement, nanostructures with tunable compositions should provide the best candidates for bimetallic catalysts, a strong feature of the galvanic replacement system.

There is also evidence that hollow structures can perform better than their solid counterparts for some reactions. While solid Pd nanoparticles used as catalysts for Suzuki coupling lost their activity after one use,[30] Pd nanoshells have been shown to retain their activity for this type of reaction for seven cycles.[31]

For these reasons, I synthesized nanoboxes and nanocages containing Pd, Au, and Ag by performing the galvanic replacement reactions in sequence. The stoichiometry of the galvanic replacement reaction provides a simple way to fine-tune the relative portion of each metal. I also investigated the optical properties of these structures as well as their use as catalysts in the decolorization of methyl red dye, and found that the order at which the metal salts were added during the synthesis played a vital role in determining both properties.

Section 3.2. The Synthesis of Au-Ag Nanocages: Galvanic Replacement between Ag Nanocubes and $HAuCl_4$

Galvanic replacement has been applied with great success to Ag nanocubes. By titrating a suspension of Ag nanocubes with $HAuCl_4$, hollow and porous structures of Au-Ag alloys can be routinely produced.[17] These are commonly referred to in our papers as Au-Ag nanocages. The overall reaction can be separated into two half reactions, the oxidation/dissolution of Ag at the anode, and the reduction/deposition of Au ions at the cathode. The relevant equations for a typical reaction are shown below:

Half reactions:

$$Ag^{+}_{(aq)} + e^{-}_{(aq)} \rightarrow Ag_{(s)} \qquad (0.80 \text{ V vs. SHE}) \qquad (3.1)$$

$$Au^{3+}_{(aq)} + 3e^{-}_{(aq)} \rightarrow Au_{(s)} \qquad (1.50 \text{ V vs. SHE}) \qquad (3.2)$$

Combined reaction:

$$Au^{3+}_{(aq)} + 3Ag_{(s)} \rightarrow Au_{(s)} + 3Ag^{+}_{(aq)} \qquad (3.3)$$

The electrochemical potentials of a number of commonly used metals are shown in Table 3.1. Note that the potentials listed here are for ideal reactions at 25 ^{o}C and 1 atm, and that the elevated temperature of this reaction (100 ^{o}C), the presence of Cl^{-} ions, and other non-standard conditions can all affect the actual potentials.[32,33] The galvanic replacement reaction is typically performed in boiling water to prevent the precipitation of AgCl onto the surface of the Ag template.[34]

Figure 3.1 shows a schematic illustration and scanning electron microscopy (SEM) images of the morphological transformations at different stages of this reaction (i.e., after the titration with different volumes of $HAuCl_4$) for a sample of Ag nanocubes ~100 nm in edge length.[17] Similar morphological changes are observed for Ag nanocubes of a wide range of sizes (30-200 nm). Figure 3.1B shows a SEM image of the starting template of solid Ag nanocubes. The inset shows an electron diffraction pattern obtained with the beam perpendicular to the surface of a nanocube. The square pattern indicates that the cube was bound by {100} facets.

When $HAuCl_4$ was added, a small pit formed on the surface of the nanocube, likely at a defect site (Figure 3.1C).[35] As the titration was continued, this pit expanded into the interior of the nanocube and the resulting structure became increasingly hollow as more Ag was dissolved. Simultaneously, Au atoms plated on the surface of the nanocube, protecting the outer surface of Ag from oxidation. A small increase in size (10-20% of the initial cube size) was observed as the reaction progressed, indicating that the Au atoms were deposited on the outer surface.[17] The conductive nature of the particle allows for electrons generated at the anode to move freely to the cathode where Au^{3+} ions are reduced and deposited. Figure 3.1D shows the product after enough $HAuCl_4$ had been added to partially hollow out the Ag nanocube. The inset shows transmission electron microscopy (TEM) image of a microtomed single particle, clearly showing the enlarged void inside the particle.

Eventually, this void expanded to fill the entire particle, resulting in a hollow shell with a shape similar to the original template, typically referred to as a nanobox (Figure

3.1E). A TEM image of a microtomed sample from this stage is given in the inset of Figure 3.1E, showing the thin walled, hollow nanostructure. Notably, the pore in the surface had closed due to volume diffusion, surface diffusion, and/or dissolution and deposition.[17,36] At this stage, the walls were composed of a Au-Ag alloy. Due to the close match in lattice constant and the high rate of interdiffusion between Au and Ag at 100 °C, an alloy quickly formed as the Au was deposited.

As additional $HAuCl_4$ was added, Ag was selectively removed from the alloyed walls, as no pure Ag remained. Due to the 3:1 stoichiometric ratio between Ag and Au, many vacancies were generated during this process. In order to incorporate these vacancies, the nanobox was forced to reconstruct into a structure with a lower surface area.[17] The sharp corners of the cubic box became truncated through the creation of triangular {111} facets at each corner, as shown in Figure 3.1F. As the dealloying process continued and additional voids were generated, they coalesced into pores on the surface, transforming the nanobox into a nanocage (Figure 3.1G). Note that the term nanocage is not shape specific, and can be applied to hollow and porous particles of other morphologies as well. If this reaction was continued even further, the pores became so large that the structure began to fall apart, resulting in Au nanoparticles with irregular shapes. The gradual replacement of Ag with Au allows for the creation of nanostructures with specific compositional ratios, an important ability given the strong effect that alloy composition has been shown to play in catalytic ability.

It is also important to mention that the final product retained the single-crystalline nature of the initial nanocube due to the epitaxial relationship between the Ag nanocube

and the Au shell that was deposited. This is evident in the diffraction pattern taken from a single Au-Ag nanobox, shown in the inset of Figure 3.1F. The square pattern of spots indicates that the nanobox was bound by single-crystal {100} facets, just like the solid Ag nanocube. The face-centered cubic (fcc) lattice constants of Au and Ag are almost identical, 4.08 and 4.09 Å, respectively, so the diffraction pattern was not expected to change after the incorporation of Au.

3.3. The Role of Surface Non-uniformity in Controlling the Initiation of a Galvanic Replacement Reaction

When asymmetric Ag nanostructures are used instead, the same general stages of the reaction can be observed (e.g., pitting, hollowing, and dealloying), however the non-uniformity of the surface provides a way to study the factors that affect the sensitivity of nanocrystal surfaces to galvanic replacement. As discussed in Section 2.1, the Ag ATO has a non-centrosymmetric shape, and can be considered as a hybrid structure between a sharp octahedron and cuboctahedron.[24] Its surface is comprised of three identical {100} facets and four types of {111} facets with a variety of areas and shapes. Figure 3.2 shows SEM images of the morphological evolution of Ag ATOs as they were titrated with increasing amounts of $HAuCl_4$. Due to the higher electrochemical potential of $HAuCl_4$ as compared to Ag, electrons were rapidly transferred from the Ag template to the $AuCl_4^-$ ions, resulting in deposition of Au atoms onto the surface of the template and dissolution of Ag from the interior of the template. This resulted in a number of distinct morphological changes as the reaction progressed. Figure 3.3 shows schematic representations of the entire process for the two most common orientations of this non-centrosymmetric particle on a flat substrate, referred to as "triangles" (Figure 3.3, A and B) and "houses" (Figure 3.3, C and D) for simplicity. Red color indicates {100} facets and blue color indicates {111} facets.

In the first step of the reaction, pitting was observed on essentially all of the {111} facets of the ATO (Figure 3.2B). Often, one pit was observed to be deeper than the others, which likely expanded to form the void in the center of the hollow nanostructure

in the next stage of the reaction. In previous studies with truncated Ag nanocubes, which also had both and {111} facets on the surface, pitting was found to occur at all eight {111} corners.[20] The pitting in the reaction with ATOs was consistent with these results, as it occurred with high selectivity on the {111} facets, providing strong support for the claim that the initiation of the galvanic replacement reaction in both cases is sensitive to either the crystal facet itself or differences in the capping of different facets.[20] In previous studies, it has been shown that PVP (the capping agent for all the Ag structures discussed in this paper) preferentially binds to the {100} facets of Ag over the {111} facets.[37,38] The relatively weak binding of PVP to {111} facets is likely an explanation of their higher reactivity to $HAuCl_4$ than the PVP-protected {100} facets.

As mentioned previously, one of the unique attributes of ATOs is the wide variety of areas and shapes of facets on the surface. Interestingly, the area and shape of the facet seem to have little effect on the initiation of galvanic replacement. Another feature of ATOs is that {111} facets comprise the majority of the surface area of the particle, instead of being limited to small corner regions as in truncated cubes. As seen in Figure 3.2B, pitting consequently occurred over more than half of the surface of the nanocrystal template. It is interesting that the particle maintained its morphology despite this large amount of corrosion.

In the next stage of the reaction, the interior of the template was hollowed out via one or more of the initial pitting sites (Figure 3.2C). The large pits created in the first stage of the reaction also began to close on the surface of the nanostructure. Tendrils of metal seemed to extend from the edges of the facets toward the center. This effect is most

noticeable on the largest {111} triangular facet, as is shown in the top right particle in Figure 3.2C. A cross sectional view of this process is shown in Figure 3.3E. While the closing of small pores has been observed in the galvanic replacement reaction with sharp Ag nanocubes due to a combination of diffusion and dissolution/deposition (enhanced at the reaction temperature of 100 °C), to my knowledge, pore closing has not been observed over such a large area.[17]

Theoretical calculations and simulations have been used previously to investigate the mobility of adatoms on Ag and Au {111} surfaces.[39] These studies found that adatoms of both metals could move rapidly across {111} facets even at low temperatures due to the low energy barrier for diffusion (0.1 eV). In addition to diffusion across {111} facets, adatoms could easily diffuse to different {111} facets and to {100} facets (though diffusion from {111} to {100} was less frequently observed with Ag). The edges of {111} facets were also slightly more energetically stable than their centers. Though in this theoretical study single metal surfaces and structures were investigated instead of alloys, the results fit well with the observation that as additional Au was deposited on the surface of the alloy, diffusion occurred rapidly across the {111} facets, resulting in closing of the pits formed in the early stages of the galvanic reaction.

Eventually, the metal extends across the void to form a structure with smooth walls, as shown in Figure 3.2D. The surfaces at this stage were either continuous Au-Ag alloy walls, or contained small pores due to incomplete sealing of the pits. As more $HAuCl_4$ was titrated, large pores developed selectively on the {111} facets due to dealloying of the Au-Ag walls (Figure 3.2E). This progression fits with what was

observed in previous systems, but it is possible to create highly porous structures due to the large size of the {111} facets on ATOs. The area and shape of the pores on the {111} facets were somewhat variable, but no pores were observed on the {100} facets. When the reaction was continued, however, the resulting structures were less well-defined and lacked a clear morphology (Figure 3.2F). Small pores developed randomly across the surface due to the extensive removal of Ag, and the nanostructures eventually collapsed into rings or small pieces.

In addition to SEM imaging, the reaction was also monitored with UV-Vis spectroscopy, as the plasmonic properties of hollow metal nanostructures depend strongly on their wall thickness.[8] Figure 3.4 shows spectra that correspond to the images in Figure 3.2. The initial suspension of Ag ATOs displayed a strong dipole resonance at 460 nm and small dipole resonance at 350 nm, as well as an additional peak at 380 nm that distinguishes the spectra of Ag ATOs from Ag nanocubes.[24] As $HAuCl_4$ was added, the primary dipole peak shifted across the visible and NIR spectrum to ~950 nm. This shift is due to the decrease in the ratio between the wall thickness and the overall diameter of the particle, confirming that the templates became increasingly hollow throughout the reaction.[8,40] The broad nature of the peak after 2.0 mL of $HAuCl_4$ solution had been added can be attributed to the non-uniform nature of the pore closing and hollowing process.

To further examine the effect of facet area and shape on the galvanic replacement reaction, I also investigated the galvanic replacement reaction between Ag nanobars and $HAuCl_4$. The nanobars had sharp corners, and were capped by two types of {100} facets

(the square ends and rectangular sides). The products resulting from this titration are shown in Figure 3.5. Similarly to what was observed with the ATOs, the position, area, and shape of the facet did not have a dominant effect on the initiation of pitting – all facets behaved equivalently. Since there were no real {111} facets in this structure (though slight corner rounding was possible), {100} facets were the only places pitting/pore formation could occur. In Figure 3.5B, pitting can be observed on both the ends and sides of the nanobar. When the reaction was continued, one (or occasionally two) of these pits expanded to create a void in the center of the nanostructure, as can be seen by the fact that a number of nanobars had a hollow side and a solid side (Figure 3.5C). Note that pure Ag was dissolved before dealloying (pore formation) began. When dealloying did occur, the pores formed on all sides of the nanobar, as with pitting (Figure 3.5D). Figure 3.6 shows the UV-vis spectra that correspond to this reaction. As the reaction progressed, the peak also redshifted due to the continuous reduction in wall thickness and broadened due to the asymmetry of the intermediate products and the porous nature of the final structures.

I also examined the reaction between Ag nanobars and AuCl (Figure 3.7), and unlike the reaction with $HAuCl_4$, the reaction did not proceed uniformly in all areas. The main difference between these precursors is while three Ag atoms must be dissolved to reduce one Au atom in the reaction with $HAuCl_4$, in the reaction with AuCl the stoichiometric ratio is 1:1. Previously, it was found that when Ag nanocubes were titrated with AuCl, the final product was Au-Ag nanoframes instead of the nanocages with many small pores seen with $HAuCl_4$.[21,22] During this process, pores initially formed both on the

sides and corners of the nanocages, but the pores on the corners filled in as the pores on the sides grew larger, resulting in a frame-like morphology. Small bumps could be seen at the corners of a number of the resulting nanoframes and the sides of the frame became significantly thicker as the reaction progressed, suggesting that atoms diffused to or were deposited preferentially on the edges of the structure.

When I performed the same reaction on the less symmetric substrate of Ag nanobars, a frame-like morphology was also observed, but with significantly more material at the ends of the nanobar than the sides (Figure 3.7B). This phenomenon would be difficult or impossible to observe in more symmetric substrates, such as Ag nanocubes. A slight "dog-bone" shape could also be seen in the early stages of the reaction (Figure 3.7A). A number of different mechanisms have been proposed for preferential deposition at the tips of structures. Preferential deposition at the corners of Au rods to form solid "dog-bone" structures during seeded growth has been attributed to uneven distribution of the micellar surfactant cetyltrimethylammonium bromide (CTAB) or facet-selective capping from other surfactants or ions added during the synthesis.[41,42] However, due to the identical capping agents and synthesis conditions in the reaction with $HAuCl_4$ and AuCl, this seems unlikely to be the cause of the unusual morphology in this reaction. A more likely explanation is reconstruction of the hollow structure, with Ag and/or Au atoms migrating to the more thermodynamically stable {111} corner facets. This mechanism has also been used to explain the closing of the corner pores in the middle of the reaction between AuCl and Ag nanocubes and the truncation of the corners of sharp Ag nanoboxes at the beginning of the dealloying stage of the galvanic

replacement reaction with $HAuCl_4$.[17,21,22] In comparison with the reaction between Ag nanobars and $HAuCl_4$, the 1:1 stoichiometric ratio in this reaction meant that additional Au would be deposited as the same amount of Ag was removed. The greater amount of metal present likely influenced the reconstruction process, leading to the different morphologies with the two precursors.

Through studying the galvanic replacement reactions involving Ag ATOs and nanobars, I have found that the crystallographic packing of the atoms on the surface is a more important parameter than the area, shape, or location of the facet. Pitting is initiated on all the {111} facets of a structure when multiple crystallographic facets are present (e.g., on ATOs) or form randomly across the {100} facets when no {111} facets are available. In the later stages of the galvanic reaction, pores also form selectively in the same regions. With ATOs, I have also been able to observe the following interesting phenomenon: (1) when many {111} facets were present, it was possible to have pitting and pore formation across a large percentage of the particle surface while still retaining the original morphology, and (2) in the intermediate stages of the reaction, the pits were mostly closed through a combination of atomic diffusion and deposition of new atoms before the dealloying stage and pore formation began. Finally, I have shown that the reaction between Ag nanobars and AuCl produced elongated nanoframes with the majority of the material concentrated at the tips of the structures, demonstrating that facets that behave equivalently under one set of reaction conditions may behave differently when reaction parameters such as the metal precursor are changed.

3.4. Tailoring the Optical and Catalytic Properties of Au-Ag Nanoboxes and Nanocages by Introducing Pd

While the galvanic replacement reaction between Ag and $HAuCl_4$ is the most commonly studied system, this reaction has also been performed with Na_2PtCl_4 and Na_2PdCl_4 and notable differences were observed.[43] In the case of Pt, a uniform alloy was not formed and Pt bumps grew on the surface of the cube as the Ag nanocube was hollowed out. In the case of Pd (Figure 3.8, the second line), alloy nanoboxes with smooth walls were formed and the system mimicked the reaction with $HAuCl_4$ until the start of the dealloying phase. Unlike the Au system, at this point Na_2PdCl_4 stopped reacting and no further morphological changes were observed, leading to a nanobox morphology instead of a nanocages as seen with $HAuCl_4$ (Figure 3.9A and B).

The early stopping of the reaction indicates that the Na_2PdCl_4 is unable to dealloy the Pd-Ag walls that formed in the early stage of the reaction. It has been noted in theoretical studies that Au and Pd can be stabilized when alloyed into an Ag matrix (and vice versa), and will consequently require higher potentials to be removed from the alloy than would be required to be oxidized as a pure metal .[32,33] Given the small magnitude of the difference between the Pd and Ag potentials, the ability of Na_2PdCl_4 to oxidize the pure Ag in the core but not dealloy Ag in the Pd-Ag alloy walls can reasonably be attributed to this type of stabilization.

In my work, I investigated the combination of these two systems, and found that the order in which the metal precursors were added had an influence on the resultant morphology.[19] For these syntheses, the galvanic replacement reactions were performed

as usual except that two different salt solutions were added one after the other. Figure 3.8 (lines 3 and 4) shows a schematic of the reaction pathways and Figures 3.9C and D show SEM and TEM images of the products, with $HAuCl_4$ or Na_2PdCl_4 added first, respectively. In comparing these two Figures, it can be seen that the resultant nanoboxes were far more porous when Na_2PdCl_4 was added first. In Figure 3.9C where $HAuCl_4$ was added first, small pits could be seen during the hollowing out phase of the reaction, but no dealloying was observed, even after large excesses of Na_2PdCl_4 had been added (e.g., 3.0 mL of a 0.5 mM solution). The only exception to this observation is when enough $HAuCl_4$ was added to initiate dealloying before any Na_2PdCl_4 had been introduced. This result suggests that the Na_2PdCl_4 was unable to effectively dealloy the Au-Ag alloy walls, so once the hollowing out of the pure Ag core was complete, the reaction could not continue any further.

Figure 3.9D shows that if the reagents were added in the reverse order, Na_2PdCl_4 first, pores were easily formed and a cage morphology was observed. This suggests that $HAuCl_4$ had no problem dealloying the Pd-Ag alloy. Furthermore, this allows for the creation of a Pd-Au system with a higher surface area, which could further increase its catalytic potential since more sites are readily available for reaction. The effect of order of addition can be explained with a mechanism similar to that discussed for the Pd-Ag system above. The Au^{3+}/Au pair has a much higher electrochemical potential than the Pd^{2+}/Pd pair, and consequently even if small increases in the dissolution potential occur due to alloying, Ag can still be removed through reaction with $HAuCl_4$. On the other hand, Pd is unable to remove Ag due to its weaker dealloying ability.

These morphological changes correspond well with differences between the LSPR spectra of each system. As discussed in Chapter 1, the LSPR peaks of Au-Ag nanocages can be continuously tuned from approximately 450 nm to 1200 nm by titrating with increasing amounts of $HAuCl_4$ solution.[17] This wavelength shift corresponds to the change in wall thickness as the solid nanocubes transform into increasingly hollow boxes, cages, and finally broken pieces. However, Pd-Ag nanoboxes, could only be tuned from 450 nm to 730 nm due to the fact that the Ag in their walls could not be dealloyed. This limiting wavelength corresponded to a final morphology of hollow boxes with smooth walls. Titrating with additional Na_2PdCl_4 did not have any effect. This abrupt stop in the LSPR peak shifting corresponded to the abrupt stop in morphological changes, in particular, the thickness and porosity of the walls.[43]

The LSPR peaks of these structures were also affected by the stoichiometry of the reaction. In Figure 3.10A the same amounts of 0.5 mM $HAuCl_4$ and Na_2PdCl_4 solution were added, but the resulting LSPR peaks were separated by ~225 nm. Part of this difference can be attributed to the uneven stoichiometric ratios caused by the difference in oxidation state for the salt precursors. The relevant galvanic replacement reactions are:

$$AuCl_4^-{}_{(aq)} + 3Ag_{(s)} \rightarrow Au_{(s)} + 3Ag^+{}_{(aq)} + 4Cl^-{}_{(aq)} \qquad (3.4)$$

$$PdCl_4^{2-}{}_{(aq)} + 2Ag_{(s)} \rightarrow Pd_{(s)} + 2Ag^+{}_{(aq)} + 4Cl^-{}_{(aq)} \qquad (3.5)$$

Since three Ag atoms are required to deposit one Au atom, while only two are necessary to deposit one Pd atom, the walls of the Au nanobox will be thinner, resulting in a further

redshift for the LSPR peak.[8] It is also possible that some of this shift was caused by the difference in the percent conversion of the salt precursor to metal, as both reactions have been shown to have less than 100% conversion.[17,43] Furthermore, the difference in dielectric function between Au and Pd should also contribute to the spectral difference.[44]

Figure 3.10B compares the UV-visible spectra of samples produced with different orders of precursor addition. Despite the fact that the same amount of each metal precursor was added (0.5 mL each of 0.5 mM solutions), the two peaks differed in wavelength by ~175 nm. The sample where Na_2PdCl_4 was added second had a shorter wavelength. This difference indicates that Na_2PdCl_4 was less effective at dealloying the Au-Ag alloy than $HAuCl_4$ was at dealloying the Pd-Ag alloy even before the limiting wavelength of 730 nm was reached.

Finally, the atomic compositions of these two samples were different. The $HAuCl_4$ followed by Na_2PdCl_4 sample was comprised of 63% Ag, 20% Au, and 17% Pd. The Na_2PdCl_4 followed by $HAuCl_4$ sample was 55% Ag, 17% Au, and 28% Pd, showing that significantly more Pd could be incorporated into the final product when Na_2PdCl_4 was added first. All of these observations support the hypothesis that $HAuCl_4$ could easily dealloy the Pd-Au-Ag alloy nanoboxes, but Na_2PdCl_4 had difficulty in dealloying Pd-Au-Ag nanoboxes, and could not do so at all once a certain stage in the reaction had been reached. This difference could be attributed to the fact that $AuCl_4^-$/Au and $PdCl_4^{2-}$/Pd pairs have different electrochemical potentials. The electrochemical potential of the nanoboxes can increase slightly to pass the electrochemical potential for $PdCl_4^{2-}$/Pd pair when Ag is alloyed with Pd, eliminating the driving force for extracting Ag atoms from

the alloyed wall by $PdCl_4^{2-}$.[33]

Methyl red was used as a model system to study the catalytic properties of the nanoboxes and nanocages. Many research groups have investigated the use of Pd-containing catalysts for the decolorization of azo dyes by splitting them into two amines.[45-47] The hydrogenation of the azo N=N bond can be monitored by using UV-visible spectroscopy, as it results in the loss of the bright red color. Figure 3.11A shows a sample set of UV-visible spectra recorded at different times, and Figure 3.11B shows a schematic of the decolorization reaction. Note that mild decolorization was also observed even without the presence of any catalyst. The rate constants for catalyst-containing samples were divided by the number of mols of Pd in the sample to take into account small differences in concentration that may arise during washing. Table 1 lists these rate constants as well as the atomic ratios, and it can be seen that the order the two salt precursors were added had an effect on the catalytic activity. Lines 2 and 3 of Table 3.2 compare samples with equal amounts of $HAuCl_4$ and Na_2PdCl_4 added, but in different orders. The sample with Na_2PdCl_4 added first had a slightly higher rate constant than the sample where $HAuCl_4$ was added first, 3.1×10^7 and 2.3×10^7 respectively. This corresponds well with the greater amount of Pd in the first sample as measured by atomic emission spectroscopy (AES). It is interesting that adding $HAuCl_4$ after Pd has been deposited does not prevent the Pd from acting as a catalyst. This implies that the two metals form an alloy or the Au forms an incomplete coverage over the Pd. Palladium-gold alloys have been reported, but are somewhat disfavored because of a lattice mismatch.[48] The opposite can be seen in a sample where additional $HAuCl_4$ was added,

the last line in the table. In this case, the catalytic ability dropped to 0.4 x 10^7, despite the fact that the amount of Pd was roughly equal to the sample with less $HAuCl_4$ added. This drop suggests that the surface was almost completely coated by Au, preventing the methyl red from accessing Pd atoms on the surface.

In summary, by performing galvanic replacement reactions sequentially with two different salt precursors, $HAuCl_4$ and Na_2PdCl_4, I have prepared Pd-Au-Ag nanoboxes and nanocages with controllable optical and catalytic properties. I have also investigated how the order of precursor addition affects the morphology, composition, optical properties, and catalytic activity of these nanostructures. If Na_2PdCl_4 was added before $HAuCl_4$, the product was more porous, contained more Pd, had a further redshifted LSPR peak, and showed higher catalytic activity.

3.5. Experimental Section

Materials. Silver nitrate ($AgNO_3$, Sigma-Aldrich, 06005KJ, 06521AD), silver trifluoroacetate (CF_3COOAg, Sigma-Aldrich, 04514TH), sodium hydrosulfide hydrate (NaHS, JT Baker, 02326AH, B25B15), sodium sulfide 9-hydrate (Na_2S, JT Baker, Y51592), ethylene glycol (EG, JT Baker, G32B27), poly(vinyl pyrrolidone) (PVP, M.W.≈55,000, Sigma-Aldrich, 03817JJ), methyl red (p-dimethylaminoazobenzene-o-carboxylic acid, JT Baker, 32001), sodium bromide (NaBr, Sigma-Aldrich, 073638), chloroauric acid ($HAuCl_4$, Sigma-Aldrich, 55898MJ), sodium palladium(II) tetrachloride (Na_2PdCl_4, Sigma-Aldrich, 01623ME), gold(I) chloride (AuCl, Sigma-Aldrich, 95096MJ) Beckman buffer (pH 4.01, Beckman Instruments), and hydrogen gas (H_2, Pacific Airgas, 99.95%) were all used as received without further purification. All water used was filtered through a Millipore E-pure filtration system at >18 MΩ cm.

Synthesis of Ag Nanocubes. In a typical synthesis, EG (6 mL) was dispensed in a 24 mL vial containing a magnetic stir bar and loosely capped with a paper lined lid (VWR, 24 mL, cat. no. 66011-143) which was then heated in a 150 ^oC oil bath for 1 hour. After that time, Na_2S dissolved in EG (80 μL, 3 mM) was injected with a micropipette, which was followed by a PVP solution (30 mg in 1.5 mL EG) and a silver nitrate solution (24 mg in 0.5 mL EG) approximately 7 minutes later. Upon addition of the silver nitrate, the solution first turned yellow, then brown, and finally became an opalescent silver color. Once this color change was complete (approximately 7-15 minutes after addition of the silver nitrate), the vials were cooled in cold water. The contents were then washed once with acetone and twice with water before being dispersed into water (4 mL).

Synthesis of Ag Asymmetrically Truncated Octahedra. Silver ATOs were prepared using a previously described overgrowth method (Chapter 2).[24] In the first step, $AgNO_3$ was reduced in a sulfide-mediated polyol reaction to generate Ag nanocubes (described in detail in ref. 49). Ten minutes after the complete addition of $AgNO_3$ solution, the cap of the reaction vial was removed, and an additional aliquot of $AgNO_3$ solution (24 mg in 0.5 mL EG) was added using a syringe pump at a rate of 0.75 mL/min. Overgrowth occurred unevenly across the surface of the nanocube, leading to the formation of ATOs. After heating for an additional 10 min, the reaction was quenched in an ice bath, washed once with acetone and then washed and dispersed in water.

Synthesis of Ag Nanobars. Silver nanobars were synthesized using a recently developed, seed-mediated method. To generate the seeds, CF_3COOAg was reduced in a polyol reaction containing trace amounts of HCl and NaHS (described in detail in ref. 4). The reaction was quenched in an ice bath when the LSPR peak of the suspension reached 400 nm, and the products were collected by centrifugation, washed with acetone and water, and dispersed in EG. For the growth of seeds into bars, 1.25 mL of EG was placed in a glass vial and heated at 150 °C under magnetic stirring. Once the temperature was stable, 50 μL of NaBr solution (6 mM in EG) was injected. After 1.5 min, 0.3 mL of a PVP solution (20 mg/mL in EG) was injected. After another 1.5 min, 40 μL of the single-crystal Ag seeds ($1x10^{12}$ particles/mL in EG) was added, followed by 40 μL of $AgNO_3$ (48 mg/mL in EG). After 3 h, the reaction was quenched in an ice bath and the products were collected by centrifugation, washed once with acetone, and then washed and dispersed in water.

Galvanic Replacement with $HAuCl_4$. A small amount of a concentrated suspension of Ag nanocrystals (25 μL of ATO or 100 μL of Ag nanobars) was added into 5 mL of PVP solution (1 mg/mL in water) that had been preheated to 100 °C. A syringe pump (KD Scientific, Single-Syringe Infusion Pump, cat no. KDS100 230) was then used to inject the volume of $HAuCl_4$ or AuCl (0.05 mM or 0.1 mM in water, respectively) indicated in the text at a rate of 0.5 mL/min.[49] After addition of the designated amount of solution, the mixture was refluxed another 10 minutes to ensure full reaction. Products were allowed to cool, collected by centrifugation, and then washed with concentrated NaCl once (for samples titrated with $HAuCl_4$) and water several times (for all).

Galvanic Replacement with $HAuCl_4$ and Na_2PdCl_4. In each reaction, the as-prepared cube solution (100 μL) was added to a PVP in water solution (5 mL, 1 mg/mL) and was preheated for 10 minutes under magnetic stirring. $HAuCl_4$ and/or Na_2PdCl_4 aqueous solutions (0.5 mM) were titrated using a syringe pump at a rate of 0.2 mL per minute, which is approximately dropwise. In reactions where both solutions were used they were titrated one after the other. After addition of the designated amount of solution, the mixture was refluxed another 10 minutes to ensure full reaction. The resulting product was washed with a concentrated NaCl solution once to remove any AgCl that formed, and then 6 times with water or a water-ethanol mixture to remove excess PVP before being dispersed in water (0.5 mL) for further analysis.

Decolorization of Methyl Red. Methyl red stock solution was prepared by dissolving solid (0.0063 g) in ethanol (25 mL), adding pH 4.01 buffer (50 mL) and then diluting to a total volume of 500 mL with water, yielding a 47 μM methyl red solution.

To perform the catalysis studies, this methyl red stock solution (3 mL) was placed in a spectrophotometer cuvette. The top of the cuvette was covered with Parafilm and bubbled with hydrogen gas (supplied by a balloon) for at least 15 minutes. The spectrophotometer was set to acquire a spectrum every three minutes. Immediately after acquisition of the first spectrum, the nanocage suspension (5 mL) was injected into the hydrogen-bubbled methyl red solution and acquisitions continued at 3 minute intervals. The maximum absorbance of each scan was converted to a concentration using the measured molar absorptivity of 24123 $M^{-1}cm^{-1}$. Nakaishi et al. reports the molar absorptivity of methyl red as 23,360$M^{-1}cm^{-1}$.[50] First order rate constants were calculated by finding the slope of the natural log of concentration vs. time plot for the time interval from 3 to 45 minutes.

Instrumentation for Section 3.2. Transmission electron microscopy (TEM) images were captured with a Tecnai G2 Spirit Twin microscope operated at 120 kV (FEI, Hillsboro, OR). Scanning electron microscopy (SEM) images were captured with a Nova NanoSEM 230 field-emission microscope (FEI, Hillsboro, OR) operated at an accelerating voltage of 15 kV. The sample was prepared by dropping an aqueous suspension of the nanoparticles onto a piece of silicon wafer (for SEM) or carbon-coated copper grid (for TEM). The LSPR spectra were recorded using a UV-visible spectrometer (Varian, Cary 50).

Instrumentation for Section 3.3. Transmission electron microscope images were captured with a Philips CM100 operated at 100 kV. Scanning electron microscope images were captured with a Sirion XL field-emission microscope (FEI, Hillsboro, OR)

at an accelerating voltage of 10 kV. Energy-dispersive X-ray spectroscopy was recorded with the EDAX system attached to the scanning electron microscope (EDX, Genesis 2000, Mahwah, NJ), also at 10 kV. Samples were prepared by dropping an aqueous suspension of particles onto a piece of silicon wafer (for SEM) or carbon coated copper grid (for TEM). LSPR spectra were recorded using a UV-visible spectrometer (Varian, Cary 50). Concentrations of the cage suspensions and molar ratios were analyzed using atomic emission spectrometry (ICP-OES, Perkin-Elmer 3300 DV with an AS93plus Autosampler).

Table 3.1. Electrochemical potentials of relevant species relative to the standard hydrogen electrode (SHE).

Half reaction	E^o/V vs SHE[a]
$Ag^+ + e^- \rightarrow Ag$	0.80
$Au^{3+} + 3e^- \rightarrow Au$	1.50
$Au^+ + e^- \rightarrow Au$	1.69
$Pd^{2+} + 2e^- \rightarrow Pd$	0.95
$Pt^{2+} + 2e^- \rightarrow Pt$	1.18

[a] For ideal reactions at 25 ºC and 1 atm. Elevation of temperature, the presence of ions such as Cl^-, and other non-standard conditions can all affect the actual potentials.[32]

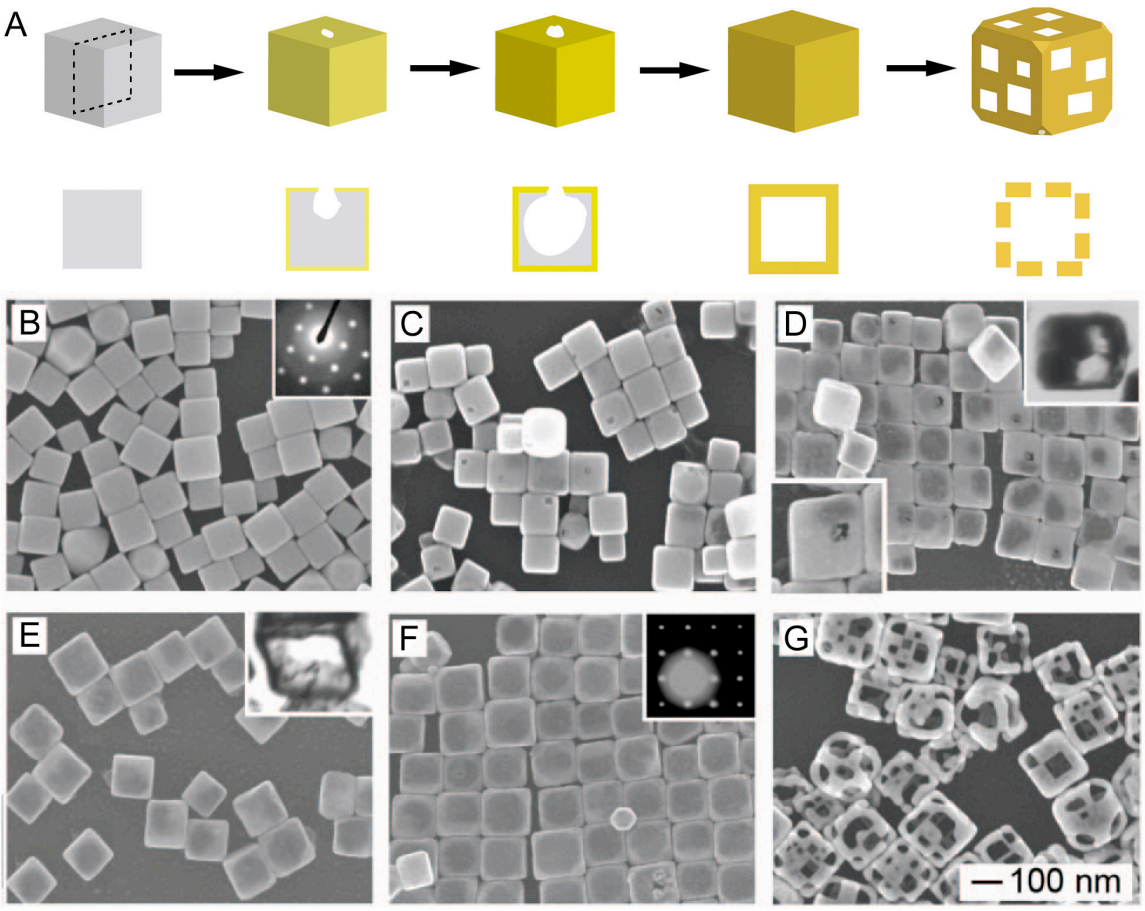

Figure 3.1. (A) Schematic illustrating the major morphological and structural changes involved in the galvanic replacement reaction between a sharp Ag nanocube and $HAuCl_4$. The cross-sectional views correspond to the plane along the dashed lines. (B) SEM image of Ag nanocubes, the sacrificial templates; and (C-G) SEM images for the hollow nanostructures obtained from sequential stages of the galvanic replacement reaction. Insets of (D) and (E) are microtomed TEM samples showing the hollow interior, and insets of (B) and (F) are the electron diffraction patterns for the corresponding nanostructures. The 100 nm scale bar applies to all SEM images.[17]

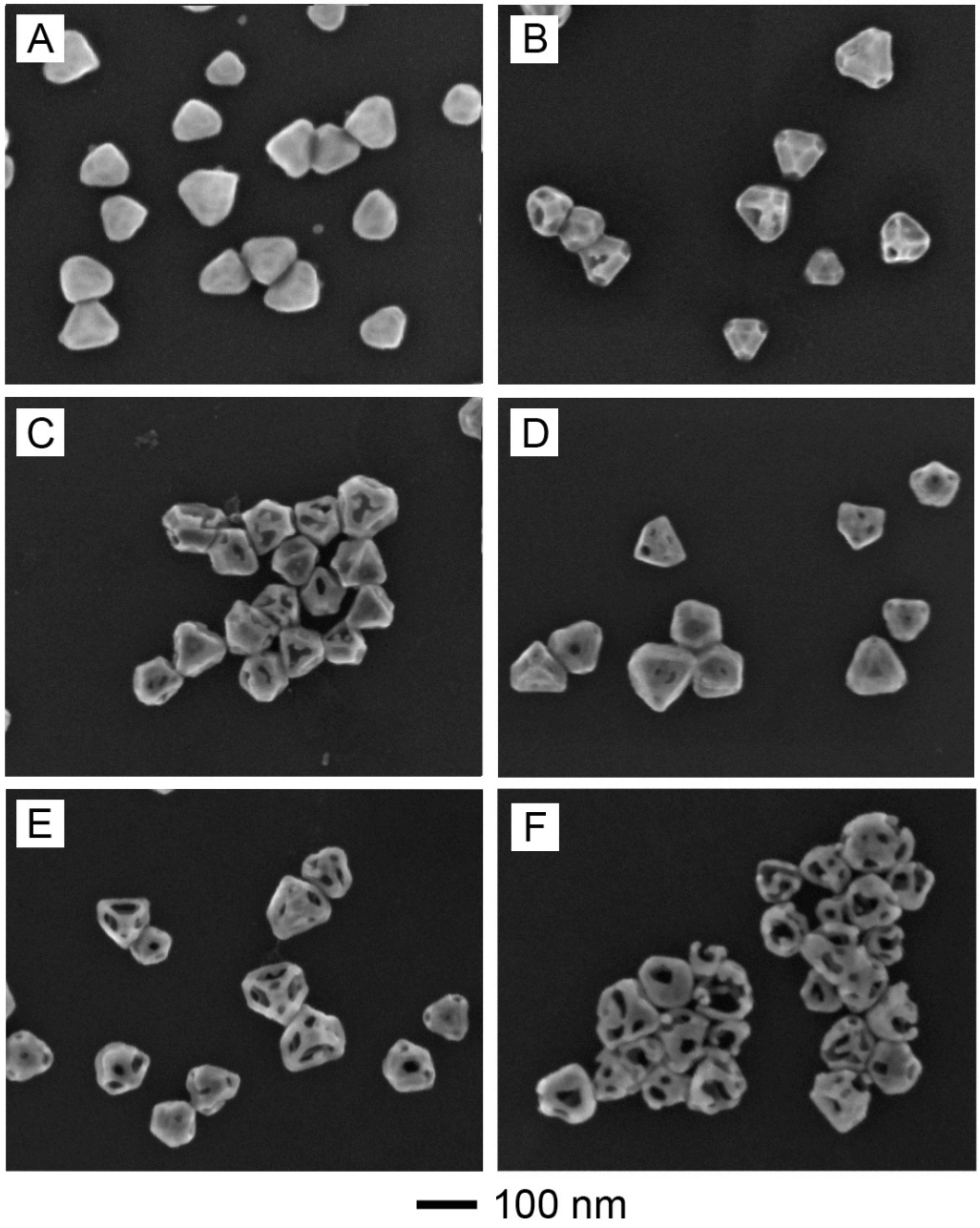

Figure 3.2. Morphological changes during the galvanic replacement reaction between asymmetrically truncated octahedra and different amounts of 0.05 mM $HAuCl_4$: (A) 0.0 mL, (B) 0.5 mL, (C) 2.0 mL, (D) 5.0 mL, (E) 6.0 mL, and (F) 7.5 mL.

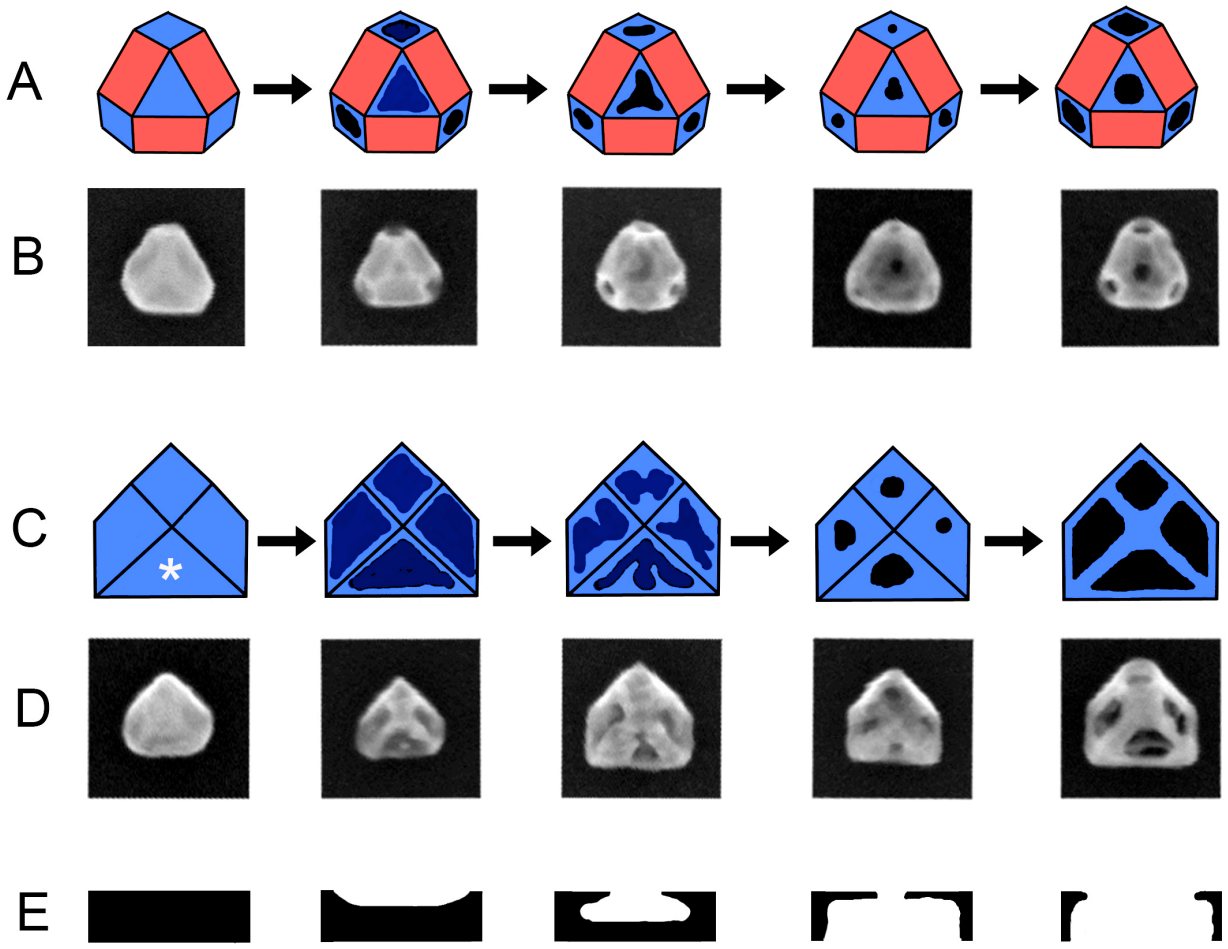

Figure 3.3. Schematic and high-magnification SEM images of the galvanic replacement process for an asymmetrically truncated octahedron at two common orientations: (A) schematic for the triangular cross-section sitting on a {111} facet, (B) SEM images at various stages of galvanic replacement for the triangular cross-section, (C) schematic for the "house" cross-section sitting on a {100} facet, (D) SEM images at various stages for the "house" cross-section, and (E) Cross-sectional view of the galvanic reaction on the large triangular {111} facet indicated with a white * in (C).

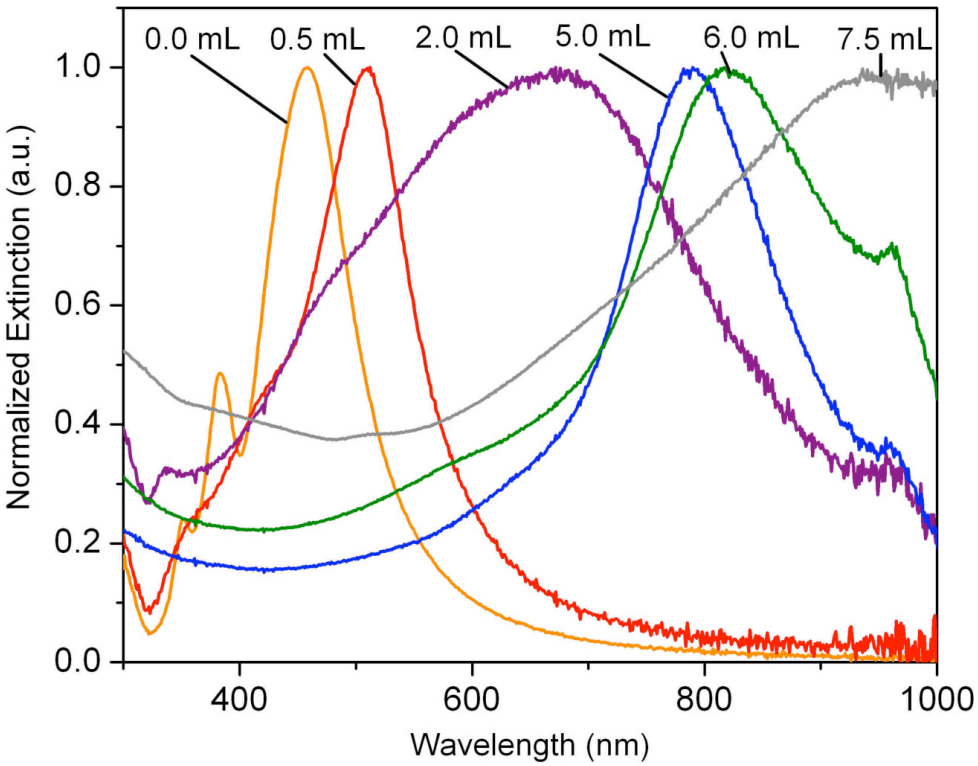

Figure 3.4. Normalized UV-vis spectra of different stages of the galvanic replacement reaction involving asymmetrically truncated octahedra, corresponding to the morphologies shown in Figures 3.2 and 3.3. The volume of $HAuCl_4$ solution is indicated above each trace.

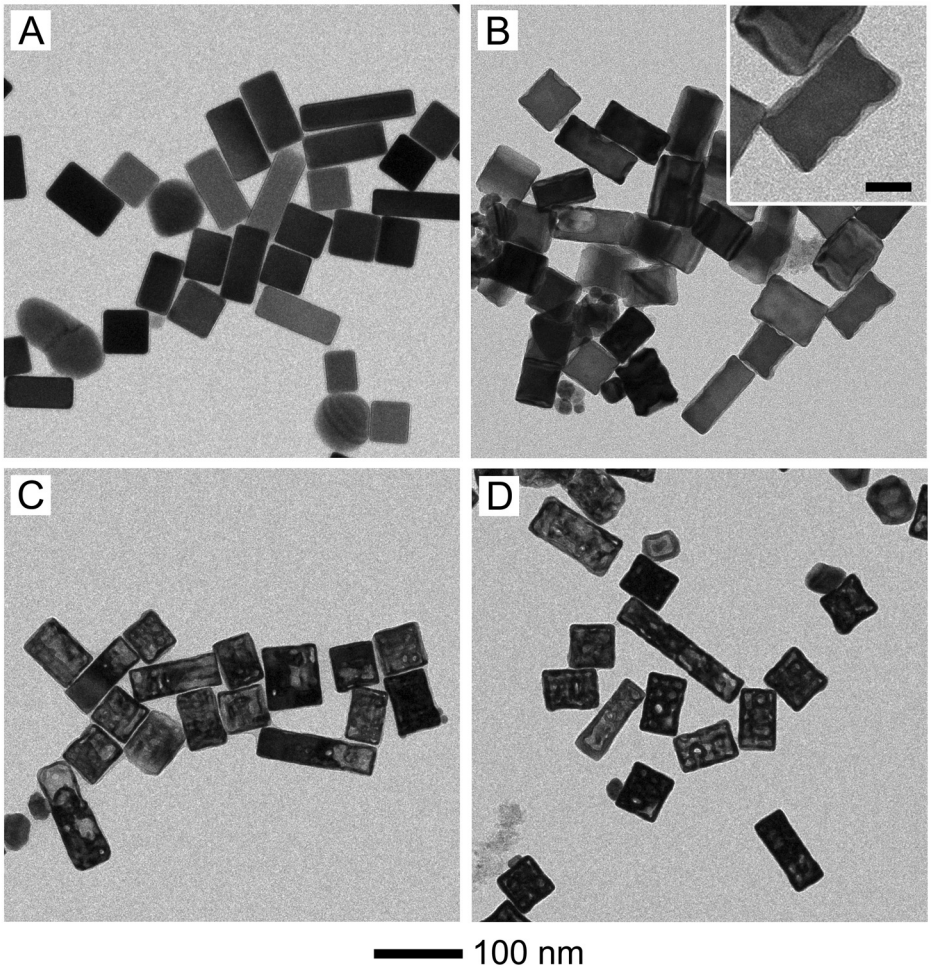

Figure 3.5. Galvanic replacement reaction between Ag nanobars and different amounts of 0.05 mM $HAuCl_4$: (A) 0 mL, (B) 0.5 mL, (C) 1.0 mL, and (D) 1.5 mL. Inset scale bar 25 nm.

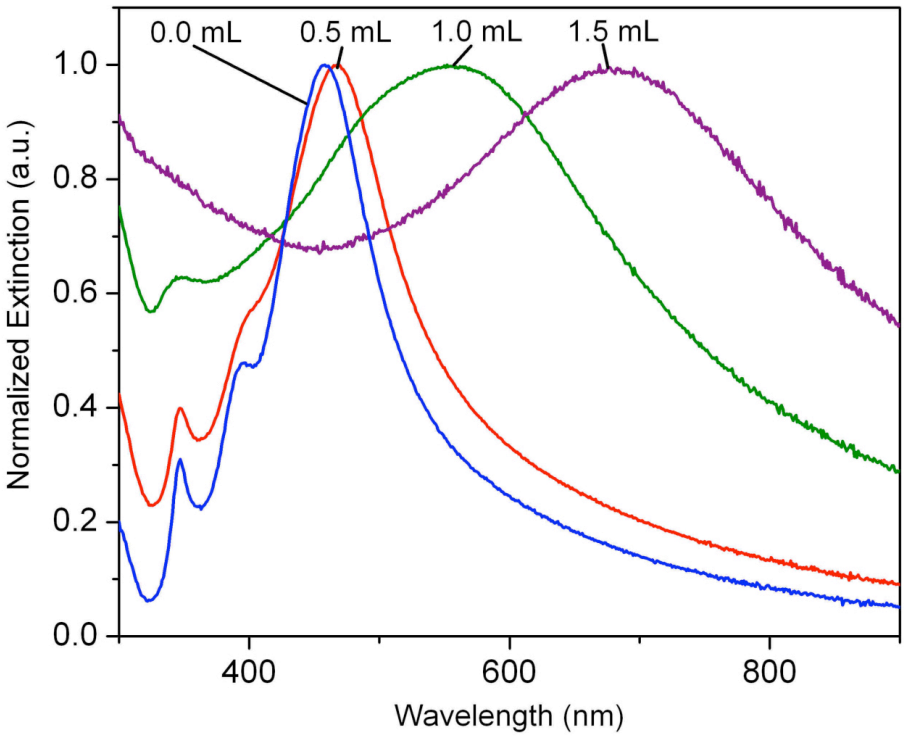

Figure 3.6. Normalized UV-vis spectra of different stages of the galvanic replacement reaction involving Ag nanobars, corresponding to the morphologies shown in Figures 3.5. The volume of $HAuCl_4$ solution is indicated above each trace.

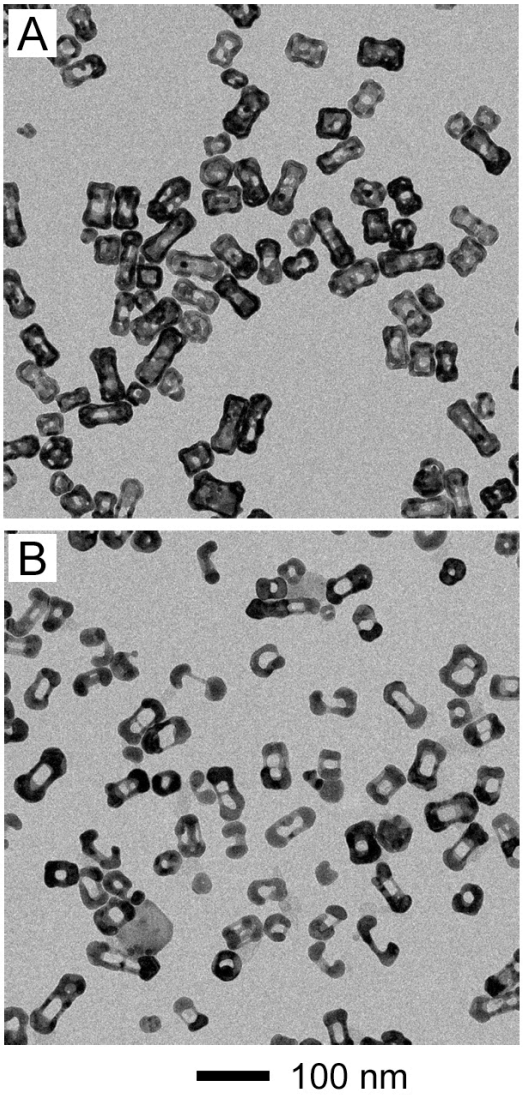

Figure 3.7. Galvanic replacement between Ag nanobars and different amounts of 0.1 mM AuCl: (A) 0.50 mL, and (B) 0.70 mL.

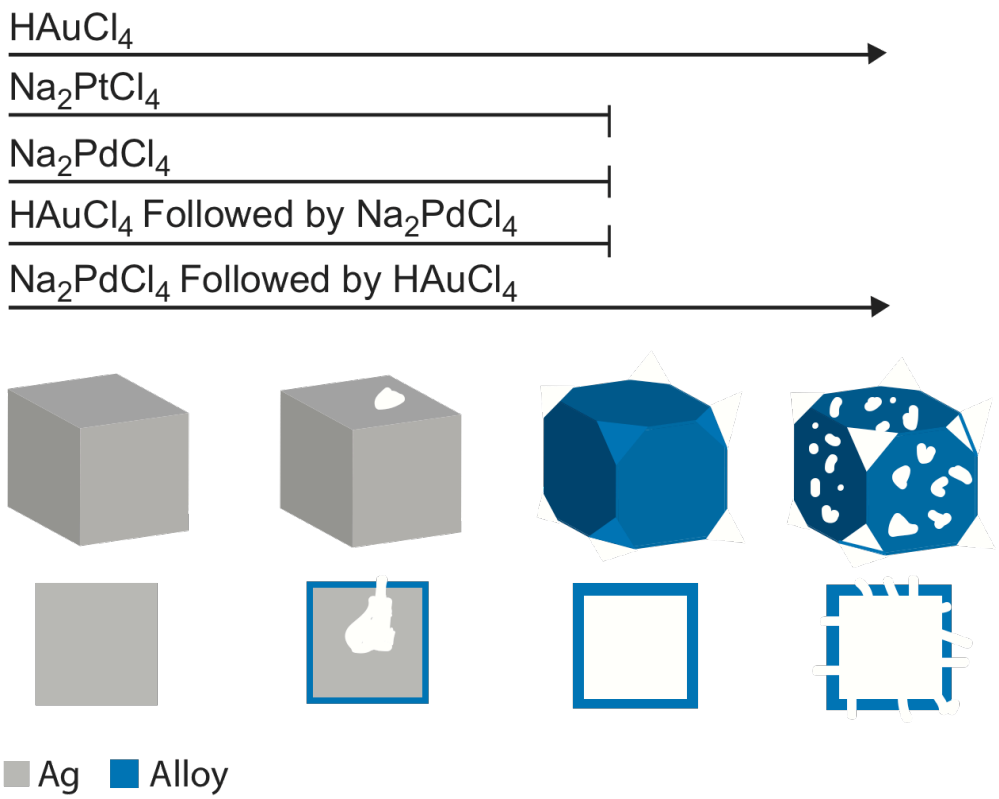

Figure 3.8. Schematic illustration of the morphological changes produced by refluxing Na_2PdCl_4 and $HAuCl_4$ with a suspension of Ag nanocubes. When only Na_2PdCl_4 was added, a hollow nanobox was produced. When only $HAuCl_4$ was added, the reaction could continue further by dealloying the nanobox to produce a porous nanobox also known as a nanocage. By combining these systems, it was possible to create a nanobox or nanocage containing Pd, Au, and Ag. Notably, if $HAuCl_4$ was added before Na_2PdCl_4, the morphology changes stopped at the box stage unless enough $HAuCl_4$ was added to introduce pores before adding Na_2PdCl_4. If Na_2PdCl_4 was added before $HAuCl_4$, the nanobox continued with dealloying to form a porous nanocage.

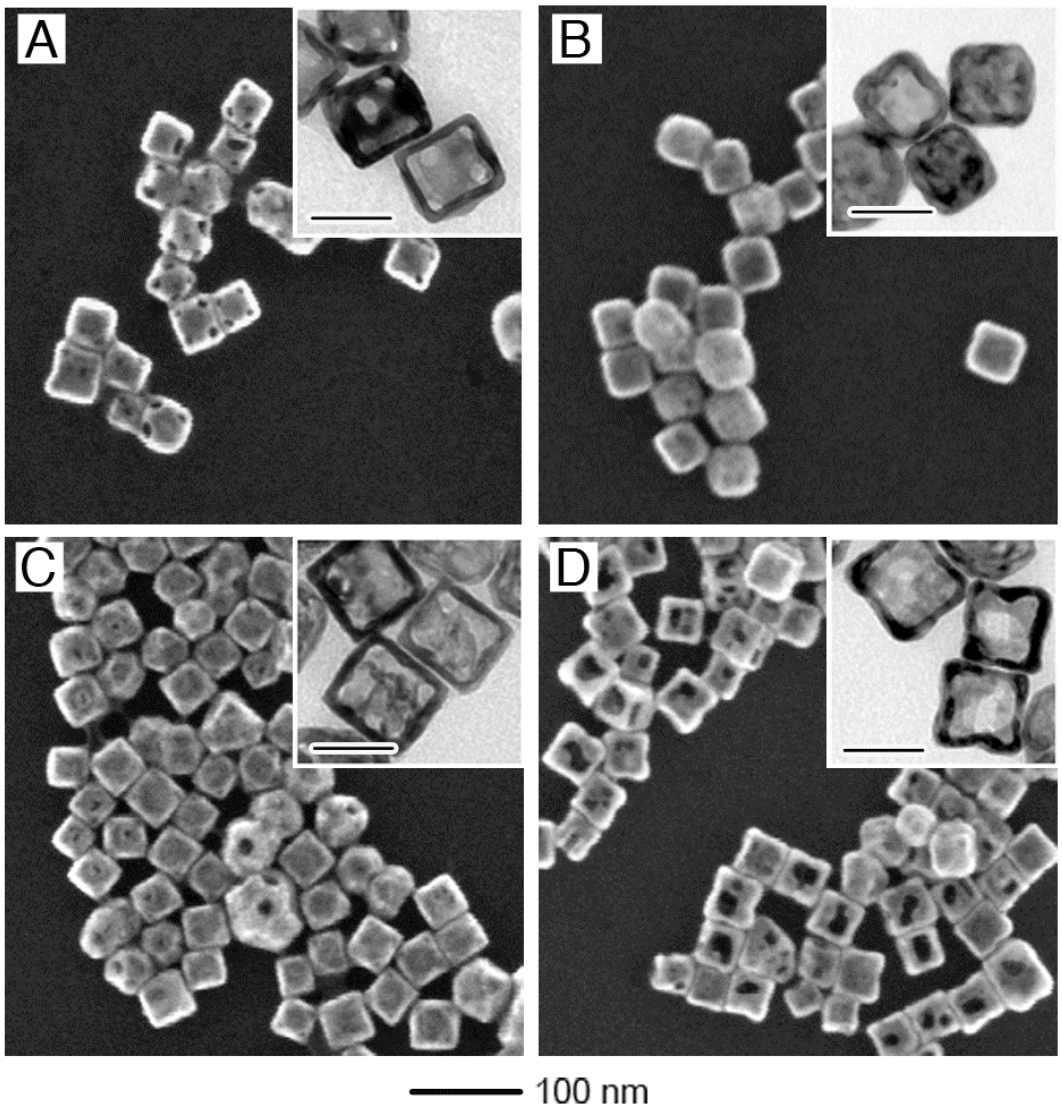

Figure 3.9. SEM images (with TEM images in the insets) of four samples showing morphologies depicted in Figure 1. To each reaction was added: (A) $HAuCl_4$ only, (B) Na_2PdCl_4 only, (C) $HAuCl_4$ followed by Na_2PdCl_4, (D) Na_2PdCl_4 followed by $HAuCl_4$. The scale bar at the bottom is for the SEM images. The TEM scale bars are 40 nm.

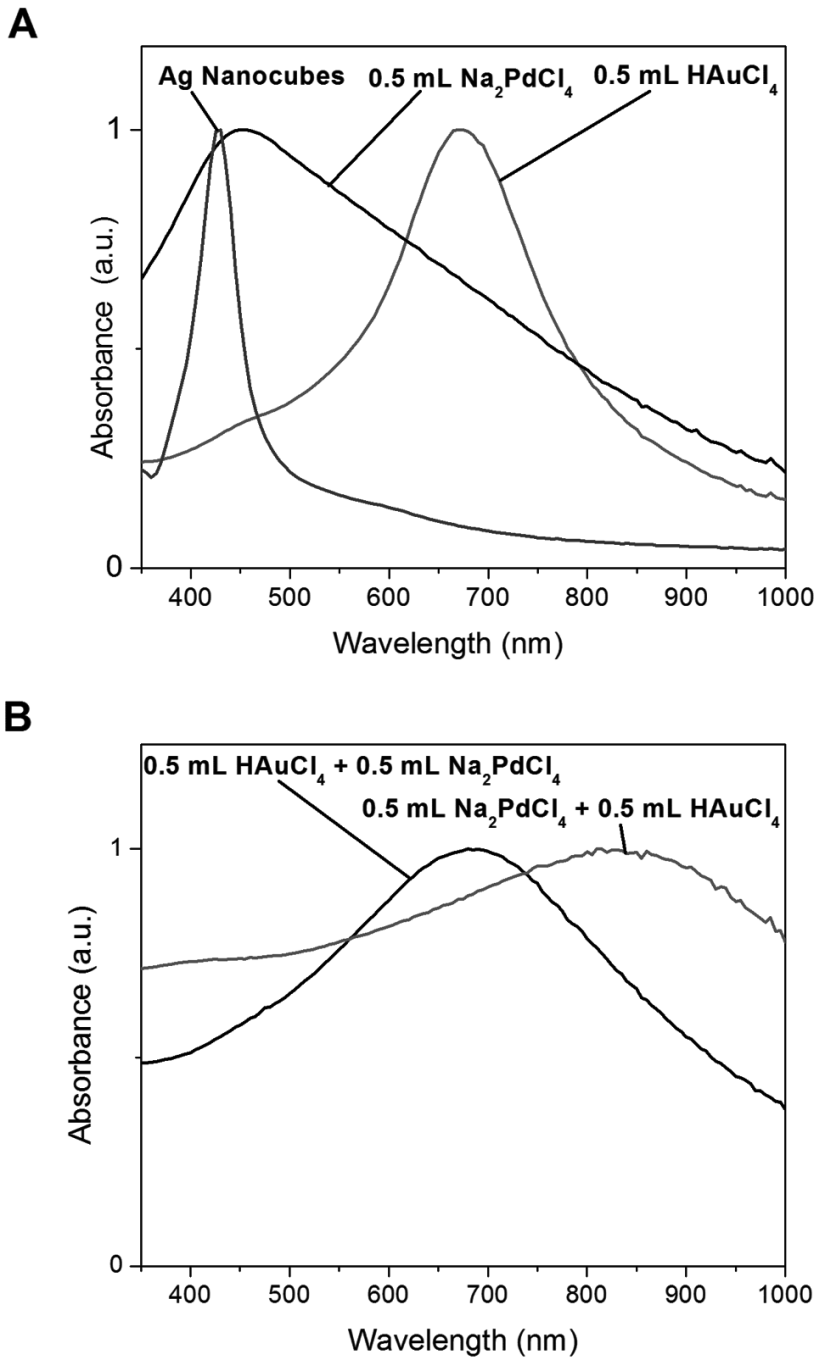

Figure 3.10. (A) Comparison of the UV-visible spectra when an equal amount of $HAuCl_4$ or Na_2PdCl_4 was added. (B) Comparison of the UV-visible spectra taken from samples when the order of solution addition was different.

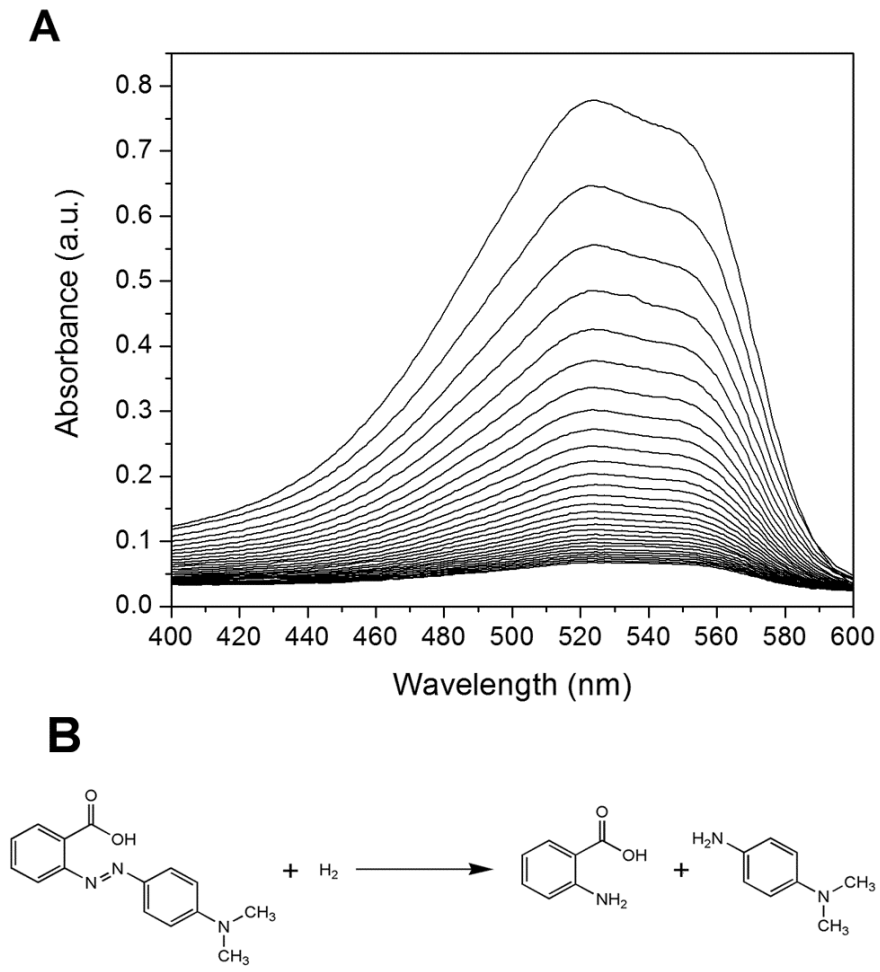

Figure 3.11. Decolorization of methyl red by hydrogenation with Pd-Au-Ag nanoboxes acting as a catalyst. (A) Gradual decrease of UV-visible peak intensity with time. Scans were taken at 3 minute intervals from top to bottom. 25 μL of the 0.5 mL $HAuCl_4$ + 0.5 mL Na_2PdCl_4 sample was used as the catalyst. (B) The decolorization reaction.

Table 3.2. Comparison of rate constants and elemental ratios.

mL of 0.5 mM solution added	k mol^{-1} Pd	% Ag	% Au	% Pd
0.5 Na_2PdCl_4	3.5 x 10^7	79	0	21
0.5 $HAuCl_4$ + 0.5 Na_2PdCl_4	2.3 x 10^7	63	20	17
0.5 Na_2PdCl_4+ 0.5 $HAuCl_4$	3.1 x 10^7	55	17	28
0.5 Na_2PdCl_4+ 1.0 $HAuCl_4$	0.4 x 10^7	21	64	25

[a] All raw k values had the k value for the blank subtracted off and were then divided by the number of mols of palladium in the catalyst. The concentrations necessary for this calculation and the elemental ratios listed all come from AES measurements.

3.6. References for Chapter 3

[1] Burda, C.; Chen, X.; Narayanan, R.; El-Sayed, M. A. *Chem. Rev.* **2005**, *105*, 1025.

[2] Xia, Y.; Xiong, Y.; Lim, B.; Skrabalak, S. E. *Angew. Chem. Int. Ed.* **2009**, *48*, 60.

[3] Tao, A.; Sinsermsuksakul, P.; Yang, P. *Angew. Chem. Int. Ed.* **2006**, *45*, 4597.

[4] Zhang, Q.; Li, W.; Wen, L.-P.; Chen, J.; Xia, Y. *Chemistry* **2010**, *16*, 10234.

[5] Yin, Y.; Alivisatos, A. P. *Nature* **2005**, *437*, 664.

[6] Habas, S. E.; Lee, H.; Radmilovic, V.; Somorjai, G. A.; Yang, P. *Nat. Mater.* **2007**, *6*, 692.

[7] Lim, B.; Wang, J.; Camargo, P. H. C.; Cobley, C. M.; Kim, M. J.; Xia, Y. *Angew. Chem. Int. Ed.* **2009**, *48*, 6304.

[8] Hu, M.; Chen, J.; Li, Z.-Y.; Au, L.; Hartland, G. V.; Li, X.; Marquez, M.; Xia, Y. *Chem. Soc. Rev.* **2006**, *35*, 1084.

[9] Wiley, B. J.; Im, S. H.; Li, Z.-Y.; McLellan, J. M.; Siekkinen, A. R.; Xia, Y. *J. Phys. Chem. B* **2006**, *110*, 15666.

[10] Kelly, K.; Coronado, E.; Zhao, L.; Schatz, G. C. *J. Phys. Chem. B* **2003**, *107*, 668.

[11] Lim, B.; Jiang, M.; Camargo, P. H. C.; Cho, E. C.; Tao, J.; Lu, X.; Zhu, Y.; Xia, Y. *Science* **2009**, *324*, 1302.

[12] Zeng, J.; Zhang, Q.; Chen, J.; Xia, Y. *Nano Lett.* **2010**, *10*, 30.

[13] Nutt, M.; Hughes, J.; Wong, M. *Environ. Sci. Technol.* **2005**, *39*, 1346.

[14] Chen, M.; Kumar, D.; Yi, C.; Goodman, D. *Science* **2005**, *310*, 291.

[15] Greeley, J.; Mavrikakis, M. *Nat. Mater.* **2004**, *3*, 810.

[16] Lu, X.; Chen, J.; Skrabalak, S. E.; Xia, Y. *Proc. Inst. Mech. Eng. N* **2008**, *221*, 1.

[17] Sun, Y.; Xia, Y. *J. Am. Chem. Soc.* **2004**, *126*, 3892.

[18] Lu, X.; Tuan, H.-Y.; Chen, J.; Li, Z.-Y.; Korgel, B. A.; Xia, Y. *J. Am. Chem. Soc.* **2007**, *129*, 1733.

[19] Cobley, C. M.; Campbell, D. J.; Xia, Y. *Adv. Mater.* **2008**, *20*, 748.

[20] Chen, J.; McLellan, J. M.; Siekkinen, A.; Xiong, Y.; Li, Z.-Y.; Xia, Y. *J. Am. Chem. Soc.* **2006**, *128*, 14776.

[21] Au, L.; Lu, X.; Xia, Y. *Adv. Mater.* **2008**, *20*, 2517.

[22] Au, L.; Chen, Y.; Zhou, F.; Camargo, P. H. C.; Lim, B.; Li, Z.-Y.; Ginger, D. S.; Xia, Y. *Nano Res.* **2008**, *1*, 441.

[23] Cobley, C. M.; Xia, Y. *Mater. Sci. Eng., R* **2010**, 70, 44-62.

[24] Cobley, C. M.; Rycenga, M.; Zhou, F.; Li, Z.-Y.; Xia, Y. *Angew. Chem. Int. Ed.* **2009**, *48*, 4824.

[25] Trzeciak, A.; Ziolkowski, J. *Coord. Chem. Rev.* **2007**, *251*, 1281.

[26] Moreno-Manas, M.; Pleixats, R. *Acc. Chem. Res* **2003**, *36*, 638.

[27] Niu, Y.; Yeung, L.; Crooks, R. *J. Am. Chem. Soc* **2001**, *123*, 6840.

[28] Venezia, A.; La Parola, V.; Deganello, G.; Pawelec, B.; Fierro, J. *J. Catal.* **2003**, *215*, 317.

[29] Andrade Sales, E.; Benhamida, B.; Caizergues, V.; Lagier, J.; Fiévet, F.; Bozon-Verduraz, F. *App. Catal. A* **1998**, *172*, 273.

[30] Li, Y.; Hong, X.; Collard, D.; El-Sayed, M. *Org. Lett.* **2000**, *2*, 2385.

[31] Kim, S.; Kim, M.; Lee, W.; Hyeon, T. *J. Am. Chem. Soc.* **2002**, *124*, 7642.

[32] Dursun, A.; Pugh, D.; Corcoran, S. *J. Electrochem. Soc.* **2003**, *150*, B355.

[33] Greeley, J.; Norskov, J. *Electrochimica Acta* **2007**, *52*, 5829.

[34] Sun, Y.; Mayers, B.; Xia, Y. *Nano Lett.* **2002**, *2*, 481.

[35] Wang, Z.; Ahmad, T.; El-Sayed, M. *Surf. Sci.* **1997**, *380*, 302.

[36] Batzill, M.; Koel, B. *Surf. Sci.* **2004**, *553*, 50.

[37] Sun, Y.; Mayers, B.; Herricks, T.; Xia, Y. *Nano Lett.* **2003**, *3*, 955.

[38] Zeng, J.; Zheng, Y.; Rycenga, M.; Tao, J.; Li, Z.-Y.; Zhang, Q.; Zhu, Y.; Xia, Y. *J. Am. Chem. Soc.* **2010**, *132*, 8552.

[39] Baletto, F.; Mottet, C.; Ferrando, R. *Surf. Sci.* **2000**, *446*, 31.

[40] Xia, Y.; Halas, N. *MRS Bull.* **2005**, *30*, 338.

[41] Gou, L.; Murphy, C. *Chem. Mater.* **2005**, *17*, 3668.

[42] Song, J. H.; Kim, F.; Kim, D.; Yang, P. *Chemistry* **2005**, *11*, 910.

[43] Chen, J.; Wiley, B. J.; McLellan, J. M.; Xiong, Y.; Li, Z.-Y.; Xia, Y. *Nano Lett.* **2005**, *5*, 2058.

[44] Creighton, J.; Eadon, D. *J. Chem. Soc. Faraday T.* **1991**, *87*, 3881.

[45] Straub, R.; Voyksner, R.; Keever, J. *Anal. Chem.* **1993**, *65*, 2131.

[46] Patel, R.; Suresh, S. *J. Hazard. Mater.* **2006**, *137*, 1729.

[47] Selvam, P.; Mohapatra, S.; Sonavane, S.; Jayaram, R. *App. Catal., B.* **2004**, *49*, 251.

[48] Massalski, T. B. *Binary alloy phase diagrams 2nd Edition*; ASM International: Materials Park, Ohio, 1990.

[49] Skrabalak, S. E.; Au, L.; Li, X.; Xia, Y. *Nature Protoc.* **2007**, *2*, 2182.

[50] Fu, E.; Ramsey, S. A.; Chen, J.; Chinowsky, T. M.; Wiley, B.; Xia, Y.; Yager, P. *Sens. Actuators, B* **2007**, *123*, 606.

Chapter 4

Gold Nanocages for Biomedical Imaging

4.1. Introduction

Optical imaging has been a critical tool in biomedical research for many years. From the use of basic light microscopy to observe the morphologies of cells, to advanced techniques for imaging millimeters (mm) deep into tissues, it is a rich and diverse field with applications in both fundamental research and the clinic.[1] One of the many techniques used to increase contrast or identify specific areas of interest during imaging is to introduce optically responsive materials to the sample.[2] Fluorescent and absorbing dyes have been used to this end with great success, but in recent years the strong, tunable, optical properties of plasmonic nanostructures have made them promising candidates for novel imaging techniques.[3-6]

Plasmonic nanostructures have a number of favorable properties that make them better than, or complimentary to, current dyes. First of all, plasmonic nanostructures can have optical cross-sections significantly higher than conventional dyes.[6,7] For example, a 45 nm Au-Ag nanocage with a LSPR peak at 650 nm has a per-particle absorption cross section (σ_a) of 5.96 x 10^{-15} m^2 (as measured by photoacoustic imaging at 650 nm), which is 200,000 fold higher than a single methylene blue dye molecule (σ_a = 2.83 x 10^{-20} m^2 at

667 nm).[8,9] Alternatively, one can compare the dimensionless absorption efficiencies (Q_a), which can be calculated by dividing σ_a by the geometrical cross section of the structure. For the nanocage described above and a methylene blue molecule, the Q_a's are 2.9 (= 5.96×10^{-15} $m^2/(45 \times 10^{-9}$ $m)^2$) and 0.025 (2.83×10^{-20} $m^2/(0.7 \times 10^{-9}$ m)$(1.6 \times 10^{-9}$ m)),[10] respectively. Even using this size-normalized comparison, nanocages absorb 116 times more strongly, which is likely related to the different mechanisms for absorption.

Another advantage of using nanostructures to enhance biomedical imaging is the ease with which one can manipulate the surface chemistry and/or add targeting ligands.[11,12] For example, it is possible to control the charges on a nanostructure by adsorbing specific polymers to the surface, which is important because surface charges can have a significant effect on both the cellular uptake and biodistribution of nanostructures. Positively charged nanostructures have been shown to have enhanced affinity to negatively charged cell surfaces, and are the most likely to cross cellular membranes and enter the cytoplasm of cells.[13,14] For Au nanostructures, the most commonly used plasmonic particles in biomedical applications, surface modification can also be achieved through the strong binding between Au and thiolate groups.[15] This approach is commonly used to coat particles with poly(ethylene glycol) to extend their circulation time for *in vivo* applications, or to add targeting ligands such as peptides and antibodies.[16,17] In addition, modifications to the surface of nanostructures can be used to add functionality. For example, if smart polymers or drugs are conjugated to the surface, nanostructures can be used for stealth delivery applications.[18,19]

In addition, plasmonic nanostructures are very versatile, as there are multiple

types of optical interactions that can be harnessed for imaging.[20,21] In one of the simplest setups, dark-field microscopy, the strong scattering of light by plasmonic nanostructures makes it possible to locate particles smaller than the diffraction limit on substrates or in *in vitro* environments due to their appearance as bright spots against a dark background.[22] Other, more complex imaging techniques which rely on light scattering for contrast, such as optical coherence tomography (OCT), can also benefit from contrast agents based on plasmonic nanoparticles.[3-5] For example, Au-Ag nanocages have been shown to enhance the contrast of OCT images in tissue phantoms.[7] The strong absorption of light by compact plasmonic nanostructures can also provide contrast both directly and through the heat that is generated from the photothermal effect.[7,23] In one such application, photoacoustic imaging, the transient heat resulting from pulsed laser excitation of plasmonic nanostructures generates acoustic signals which can be detected using a scanning transducer.[24,25] Finally, plasmonic nanostructures can also exhibit a bright multi-photon luminescence which, in combination with fluorescent dyes, makes it possible to image their distribution in, and uptake by cells.[21,26,27]

Though a number of types of plasmonic nanostructures have been investigated for use in biomedical imaging,[4-6] the Au-Ag nanocages described in Section 3.2 are ideal for such applications for a number of reasons.[28] First of all, the position of their LSPR peak can be easily shifted into the NIR region where light absorption from blood and tissue is low, and to match the wavelength of the laser setup.[29,30] By simply changing the amount of $HAuCl_4$ titrated during the galvanic replacement reaction, it is possible to shift the LSPR peak from the ~450 nm of Ag nanocubes to 800 nm and beyond, depending on the

size of the nanocubes (Figure 1.2).[28] This dramatic change in optical properties is due to the reduction in wall thickness during the galvanic replacement reaction described in the previous chapter.[31]

The relative contributions of absorption and scattering to the overall extinction cross section of Au-Ag nanocages can also be controlled. This is achieved by simply adjusting the size of the nanocages.[32] The LSPR response of small nanocages (e.g., 35 nm in edge length) is dominated by absorption, however the LSPR response of large nanocages (e.g., >60 nm) has a large scattering component.[3] Advantageously, the size of Au-Ag nanocages can be easily tuned by adjusting the size of the initial template Ag nanocubes. A number of synthetic methods have been developed for generating Ag nanocubes with edge lengths in the range of 25-200 nm (typical Au-Ag nanocages are ~20% larger than the initial template nanocubes), providing a wide range of available sizes.[29,33-36] Conveniently, this size regime is also appropriate for passive targeting of tumors in *in vivo* applications.[37]

Due to these favorable properties, Au-Ag nanocages have been investigated as contrast agents for OCT, photoacoustic imaging, and both two- and three-photon luminescence (2PL, 3PL) probes.[18,26-28] Additionally, the potential therapeutic applications of Au-Ag nanocages in both photothermal therapy and drug delivery also make them interesting as theranostic agents, as therapeutics and diagnostics could potentially be combined.[18,26-28]

In this Chapter, I will first describe a study of the cytotoxicity of Au-Ag nanocages with different compositions and surface chemistries (Section 4.2), as

biocompatibility is an important consideration with any new material in biomedicine. This section will be followed by a discussion of two of the recent demonstrations of Au-Ag nanocages for biomedical imaging. Section 4.3 will describe their use in *in vitro* particle tracking based on a novel 3PL technique, and Section 4.4 will discuss their use as contrast agents in *in vi*vo sentinel lymph node mapping with photoacoustic imaging.

4.2. Cytotoxicity of Au-Ag Nanocages with Different Ag Contents and Surface Coatings

Due to the rising number of potential applications of nanostructures in biomedicine, it is important to study the biocompatibility of these materials. Through initial studies with a variety of nanostructures, a number of critical parameters that affect the biocompatibility have been determined, including: composition, surface coating, surface charge, size, shape, and aggregation state.[38-40]

Due to its non-reactive and relatively bio-inert nature, Au nanostructures are the primary class of plasmonic nanostructures being investigated for biomedical applications.[30,38,41] A variety of experiments have been performed with pure Au nanostructures that suggest these structures will be well tolerated. For example, gold nanostructures generally exhibit little or no cytotoxicity, though there are reports of reduced cell viability when the particles are extremely small (e.g., 1.4 nm) or capped with specific surface coatings (e.g. cetyltrimethylammonium bromide).[14,38,42]

Initial *in vivo* and clinical biocompatibility studies have also shown favorable results for Au nanostructures.[38,43,44] Gold colloids were studied in humans in the 1950's as radiotracers for sentinel lymph node biopsy, and a phase I clinical trial has recently been completed for drug carriers based on Au nanospheres.[43-45] Despite the involvement of high doses of a toxic cytokine (tumor necrosis factor-alpha, TNF-α), minimal side effects were observed from treatment with the TNF-Au nanospheres.[44]

On the other hand, Ag nanostructures have caused significant cytotoxicity in some *in vitro* studies.[46-48] In a study with alveolar macrophages, Ag nanostructures were

shown to induce size-dependent cytotoxicity, significant inflammatory responses, and an increase in oxidative stress.[49] As Au-Ag nanocages are comprised of an alloy between these two metals, the expected level of cytotoxicity is not immediately apparent, and there is little data available in the literature on how alloying affects the cell viability.[50] For this reason, I performed an *in vitro* study to examine the cytotoxicity of nanocages with different Au:Ag ratios and surface coatings.

Figure 4.1 shows the results of a cytotoxicity assay based on MTT (3-(4,5-dimethylthiazol-2-yl)-2,5-diphenyl tetrazolium bromide) after WI-38 normal human fibroblasts were exposed to Au, Ag, or Au-Ag alloy nanostructures for 24 h. The nanostructures were either coated with polyvinyl pyrrolidone (PVP) or 5K methoxy(poly ethylene glycol) (mPEG) bound to the nanostructure surface with a thiol group. I tested three different types of alloyed nanocages, with Au:Ag weight ratios of 70:30, 45:55, and 15:85, as well as solid Ag nanocubes and Au nanospheres for comparison. All particles had diameters close to 50 nm; the specific diameters are shown in Table 4.1, as measured by TEM.

A concentration range of 1-500 pM was chosen to represent the expected range encountered by cells in typical *in vitro* and *in vivo* studies. For example, in typical current *in vivo* experiments our group uses 100 μL of a 10 nM nanocage solution (concentration in terms of particles). For a 28 g mouse, this would result in a final blood concentration of ~500 pM.[51] Furthermore, an earlier study of the biodistribution of Au-Ag nanocages after a 15 nM solution was injected found that the final concentration in the spleen, where the highest number of nanocages were observed, corresponded to a

"concentration" of ~520 pM in tissue (treating 1 cm^3 of tissue as 1 mL, using a spleen density of 1.06 g/cm^3).[52] Previous *in vitro* studies of the cellular uptake of Au-Ag nanocages have typically used a concentration around 20 pM.[27]

Figure 4.1A shows the cell viability after treatment with different concentrations of Au, Ag, and Au-Ag nanostructures coated with PVP for 24 h. This surface coating represents as-synthesized nanocubes and nanocages, with no additional conjugation steps. For Au nanospheres, the as-purchased coating of tannic acid was replaced with PVP. For all the samples investigated, greater than 90% viability was observed at the 1 pM level, which was maintained as the concentration increased to 10 pM for all samples except the 15:85 nanocages. Using ANOVA to compare the different nanostructure compositions at each concentration, no significant difference was found at the 1 pM level. While the overall comparison at the 10 pM level showed a statistically significant difference ($P=0.0003$), Tukey-Kramer post-tests between individual pairs only demonstrated significant differences between the 15:85 nanocages and the other compositions.

At the 50 pM level, however, more dramatic changes started to occur. The viability of cells treated with Ag nanocubes decreased to 55±7% when the nanostructure concentration was 50 pM and was severely diminished when the nanostructure concentration was 100 pM or 500 pM, (3±2% and 2±3%, respectively). For the 100 and 500 pM Ag nanocube-treated samples, the cells changed from the elongated morphology typical of WI-38 cells to a rounded shape within 10 minutes of the addition of Ag nanocubes, and only cell debris was visible after 24 h. Statistical analysis showed significant differences in cell viability ($P<0.0001$) with nanostructure composition for the

50, 100 and 500 pM particle concentrations. Post-tests of individual pairs showed differences significant at $P<0.001$ between the low-Au nanostructures (0:100 and 15:85) and high-Au nanostructures (45:55, 70:30, 100:0).

It is interesting that despite only containing a small amount of Au, the Au:Ag 15:85 nanocage sample exhibited a significantly milder cytotoxic response than the Ag nanocubes at the 100 pM (64±2% vs. 3±2%, $P<0.001$) and 500 pM (56±5% vs. 2±3%, $P<0.001$) concentrations, though it was still more toxic than the samples with a greater percentage of Au. This large increase in cell viability may be due to the Au in the nanostructure being present at a higher ratio near the surface of the particle. A higher Au:Ag ratio on the surface would be expected from mechanistic studies of the galvanic replacement reaction which showed that during the early stages of the reaction Au is deposited on the outside of nanocages while Ag is dissolved from the interior (discussed in detail in Section 3.2). The Au nanospheres and Au:Ag nanocages with Au:Ag ratios of 45:55 and 70:30 all exhibited similar, low cytotoxicities at all concentrations. Though some statistically significant comparisons between high-Au nanostructures were observed with certain post-tests ($P<0.05$ for 70:30 vs. 100:0 at 50 pM, 45:55 and 70:30 vs. 100:0 at 100 pM, and 45:55 vs. 70:30 at 500 pM), the magnitude of the differences between cell viabilities were all <15%.

Figure 4.1B shows the cytotoxicity of the same set of samples after coating with mPEG, one of the most common coatings for nanostructures in biomedical applications. Most nanostructures used *in vivo* are capped with mPEG as it minimizes uptake by the reticuloendothelial system (RES), extending their circulation time so that more

nanostructures can accumulate in the desired region.[16] For the Ag and 15:85 Au-Ag samples that caused substantial cytotoxicity with a PVP coating at 50, 100, and 500 pM, the mPEG coating improved the cellular viability (all comparisons significant at $P > 0.01$). In addition, the cells exposed to high concentrations of mPEG-coated Ag nanocubes still had an elongated morphology after 24 h. The effect of composition on cell viability for PEG-coated samples was milder than with the PVP-coated samples. While statistically significant differences were observed as the composition of the particles changed at concentrations ≥50 pM using ANOVA, the magnitude of the change was smaller than with the PVP-coated samples. For example, when comparing the 100:0 Ag nanocubes with the 70:30 nanocages at 500 pM (the largest differences observed), for PVP-coated samples the difference in cell viability was 91%, while for PEG-coated samples the difference was 41%.

As surface charge, aggregation state, and particle etching have been shown to influence the cytotoxicity of nanomaterials, I collected zeta potentials, LSPR spectra, and TEM images of the nanostructures before and after incubation with media. In previous studies, greater cytotoxicity has been observed with nanostructures having positive surface charges.[53] This increased toxicity as compared to negatively charged or neutral nanostructures was attributed to the fact that positively charged nanostructures can induce pore formation in the cell membrane. Larger numbers of nanostructures can consequently cross the cell membrane and enter the cytoplasm, making them interesting for delivery applications, but if the pores are too large the balance of proteins and ions maintained by the cell membrane will be disrupted, resulting in cytotoxicity.[54-56] It is

important to note, though, that the absorption of serum proteins can change the effective surface charge of nanostructures in culture media. The resulting protein corona will influence how the nanostructures interact with cell surfaces, and can also lead to cellular recognition and uptake.[14] Previous studies have reported that Au nanostructures with a variety of initial surface charges all developed a zeta potential near -20 mV after only 5 minutes in media.[14] Table 4.1 shows the zeta potentials of all the nanostructures used in this study before and after incubation in media for 24 h. All the nanostructures exhibited a negative zeta potential before incubation, and a zeta potential not far from -20 mV after incubation. Since none of the nanostructures exhibited a positive surface charge, it is unlikely that the observed cytotoxicity was due to the pore formation mechanism described above.

Figure 4.2 shows the LSPR spectra of the Ag nanocubes and Au nanospheres before (red) and after (blue) incubation in media. Figure 4.3 shows the same measurements for the Au-Ag nanocages. Samples were washed once and transferred into water after 24 h incubation in media. As discussed previously, a number of different factors can influence the LSPR resonances of nanostructures in solution. In this system, the most likely reasons the LSPR spectra would change are: i) a change in the corner sharpness and/or wall thickness due to Ag being removed by etching, ii) a change in the refractive index near the surface of the particle due to the non-specific absorption of proteins from media, and iii) interactions between the plasmons of different particles due to aggregation. Generally, corner-rounding causes a blue-shift in the primary LSPR peak, while protein absorption, wall-thinning, and aggregation cause red-shifts.[27,57,58]

For both the PVP and mPEG-coated Ag nanocubes, a second peak developed to the red of the original LSPR peak (Figure 4.2, A and B). The significant red-shift and the fact that the precise position and size of this peak changes upon sample sonication suggest that it is due to aggregation. This second peak was also visible (though somewhat smaller) before the sample was transferred into water, indicating that the aggregation could occur during incubation in media, not during the transfer into water. The primary LSPR peak also broadened slightly and blue-shifted, which would be consistent with rounding of the sharp features of the cubes due to etching. However, the changes are mild and complicated by the fact that the spectra will also be influenced by the absorption of proteins from media. Minimal or no LSPR shifts were observed with the Au nanospheres – etching would not be expected for Au structures, and mPEG-coated nanostructures would not be expected to absorb proteins as easily.

The spectra of the Au-Ag nanocages shown in Figure 4.3 generally show mild red-shifts in response to media incubation that can be explained by a combination of protein absorption and potentially reduced wall thickness from etching. Note that hollow structures are known to be more sensitive to refractive index changes than solid ones, so the shifts from protein absorption would be expected to be larger with nanocages than with solid particles.[59] The change in position and height of the shoulder for the 15:85 sample in Figure 4.3, A and B, is similar to is the changes typically observed during the early stages of the galvanic titration as the partially reacted particles become increasingly hollow.

I also examined TEM images of the nanostructures before and after incubation in

media. The morphologies of the nanostructures were stable, as shown for the PVP-coated nanostructures in Figure 4.4; similar results were obtained for the mPEG-coated nanostructures. The only potential change in morphology was with the PVP-coated Ag nanocubes, where the final sample appeared to have more rounded nanocubes and irregular particles. Note, however, that very small amounts of Ag etching would not be detectable with TEM imaging.

One potential reason for the cytotoxic response to Ag and predominantly Ag alloyed nanostructures could be Ag^+ ions dissolving from the particles.[60] For this reason, I also performed an MTT assay on WI-38 cells after being exposed to media containing Ag^+ ions (from $AgNO_3$) at different concentrations for 24 h (Figure 4.5). A sharp drop in cell viability occurred between 1.2 and 5.8 μg/mL of Ag^+. A concentration of 5.8 μg/mL is equivalent to dissolving a 10.7 pM solution of nanocubes into ions. Alternatively, this concentration could be reached by dissolving 2.1% of a 500 pM, 10.7% of a 100 pM, or 21.4% of a 50 pM suspension of Ag nanocubes. These values are in line with the cytotoxicity results for PVP-coated Ag nanocubes (Figure 4.1A). For example, it seems reasonable that 2.1% of the 500 pM nanocube sample could be dissolved, resulting in an Ag^+ concentration high enough to contribute to the observed cytotoxicity. However, based on the mild or non-existent changes in the changes in the LSPR and TEM images described above, the large amounts of Ag dissolution that would be necessary to generate a 5.8 μg/mL Ag^+ concentration with low concentrations of Ag nanostructures or Au-Ag nanostructures with high Au:Ag ratios did not occur, fitting with the high cell viabilities observed.

In conclusion, the cytotoxicity of Au-Ag alloyed nanocages generated using the galvanic replacement reaction depends on their composition. However, only a small amount of Au needs to be incorporated to dramatically improve the cell viability when compared to experiments with pure Ag structures. Nanocages with Au:Ag weight ratios of 45:55 and 70:30 exhibited low cytotoxicities, which were similar to those of Au nanospheres over a concentration range of 1-500 pM. Coating the nanostructures with mPEG substantially improved the cell viability for samples that exhibited a cytotoxic response when they had a PVP coating. The cytotoxicity of the nanostructures containing large amounts of Ag is likely related to Ag dissolution from the particles, though other factors such as reactive oxygen species (ROS) production on the surface of the nanostructures likely also play a role, and will be the subject of future work.[49]

4.3. Bright Three-Photon Luminescence from Au-Ag Alloyed Nanostructures for Bioimaging with Negligible Photothermal Toxicity

In recent years, two-photon microscopy has gained popularity due to its ability to penetrate deeper into tissue than related high-resolution imaging techniques such as confocal microscopy.[61] Typical depth penetration is on the order of 100's of microns.[61] While originally used to image NIR fluorescence dyes, it has been recently demonstrated as a method to image Au nanostructures with appropriate LSPR resonances in cultured cells, tissue phantoms, and *in vivo* circulation for blood vessels near the skin surface, such as those in a mouse ear.[21,62] The resulting signal has been reported to be 60-140 times greater than seen with fluorescent beads.[62] When Au nanostructures are excited with a femtosecond pulsed laser, the absorption of two photons excites electrons from the d-band to the sp-band, creating electron-hole pairs. When these electron-hole pairs recombine, luminescence is emitted in the visible region. This process is significantly enhanced when the LSPR of the nanostructure matches well with the wavelength of the photons used to excite the luminescence.[21] For this reason, nanostructures with tunable LSPR resonances like Au-Ag are typically used.[21,62] The two-photon luminescence (2PL) of Au-Ag nanocages was recently used to monitor the cellular uptake and binding of targeted and non-targeted Au-Ag nanocages in an *in vitro* study.[27]

However, due to the requirement that the LSPR of the Au-Ag nanocages must have strong overlap with the laser wavelength, heat will also be generated through the photothermal effect.[26] While this is advantageous for certain applications such as thermal ablation of tumors, it is not ideal for imaging applications as it will influence the sample.

Figure 4.6 shows a sample of KB cells before and after 90 s of raster scanning the region of interest with a 760 nm femtosecond laser with a power of 1.9 mW after the objective.[26] The white arrows indicate areas where membrane blebbing occurred and membrane damage is revealed by ethidium bromide staining (shown in green). Furthermore, the intensity of the 2PL decreased after repetitive scanning, likely due to melting of nanocages and resultant shifting of the LSPR peak position.

In a collaboration with Prof. Ji-Xin Cheng's group at Perdue, we found that Au-Ag nanocages also exhibit a novel 3PL which is not dependent on LSPR overlap with the laser source.[26] Instead, this less commonly observed luminescence appears to originate from the alloyed composition of Au-Ag nanocages. Substrate-based studies of the luminescence intensity and spectral properties were performed with pure Au and Ag nanoparticles as well as solid Au-Ag nanospheres for comparison. The 3PL of alloyed nanocages and nanospheres was found to be an order of magnitude stronger than that observed with the single metal particles. Figure 4.6, D and E, shows the same type of imaging as in Figure 4.6, A and B, except that 3PL was excited in the nanocages instead of 2PL. To excite the 3PL, the sample was scanned with a 1,290 nm femotsecond laser at a power of 4.0 mW after the objective. Despite a higher laser power, no membrane damage or photobleaching of the luminescence was observed after 90 s of scanning. Another advantage for imaging with a laser at 1,290 nm instead of 760 nm is that this wavelength of light induces less autofluorescence in tissue, making it easier to distinguish the luminescence from the nanoparticles, shown in Figure 4.6F for a liver tissue slice.

4.4. Near-Infrared Au-Ag Nanocages as a New Class of Tracers for Photoacoustic Mapping of a Sentinel Lymph Node on a Rat Model

In vivo optical imaging techniques are of great interest due to their low cost, portability, and non-ionizing radiation. Unfortunately, such techniques are typically limited by the strong light absorption of blood and tissue, limiting their depth penetration. However, photoacoustic methods can offer non-invasive imaging at depths of 10's of mm by combining optical techniques with ultrasonic imaging.[25] When tissue is irradiated with a pulsed laser source, the resulting heat creates a transient thermoelastic expansion, which leads to an acoustic signal that can be detected and converted into an image by a scanning transducer.[24] As the signal is directly related to the amount of light absorption, the sensitivity of this technique can be enhanced through the addition of highly absorbing Au-Ag nanocages, providing enhanced contrast and depth capabilities.[23] Furthermore, Au-Ag nanocages can provide additional functionality, through the addition of targeting ligands to concentrate their uptake in cancerous tissue or potentially by combining imaging with therapeutic techniques such as photothermal therapy or Au-Ag nanocage-based drug delivery.[18,63]

The combination of Au-Ag nanocages and photoacoustic imaging has the potential to improve upon existing breast-cancer staging techniques, in particular sentinel lymph node biopsy.[64] Before a biopsy can be collected for analysis to determine the stage of a cancer, the sentinel lymph nodes must be identified. Current detection techniques based on staining with methylene blue dye or labeling with radioactive colloids are not ideal because they either require invasive techniques to visualize the blue

stain or specialized facilities to deal with potentially hazardous radioactive components.[65] An optical technique which could detect sentinel lymph nodes without surgery or radiation is therefore highly desirable. Consequently, in collaboration with Prof. Lihong Wang's group, we investigated the use of Au-Ag nanocages as contrast agents in the non-invasive photoacoustic mapping of sentinel lymph nodes.[64]

Figure 4.7 shows the depth capability of photoacoustic imaging when Au-Ag nanocages were used as a contrast agent for *in vivo* sentinel lymph node mapping.[64] The first panel shows the region before nanocage injection. Each successive panel shows an image with an additional layer of ~10 mm thick chicken breast tissue placed on top of the region of interest to demonstrate the feasibility of this method to detect sentinel lymph nodes for breast cancer staging in humans. A distinct image of the sentinel lymph node could be obtained as deep as 33 mm, though this limitation was actually imposed by the memory of the acquisition system. This depth is significantly greater than the typical ~12 mm depth of sentinel lymph nodes in humans, making this a promising approach for the detection of sentinel lymph nodes without invasive procedures.

4.5. Experimental Section

Materials. Silver nitrate ($AgNO_3$, Sigma-Aldrich, 06005KJ, 06521AD), silver trifluoroacetate (CF_3COOAg, Sigma-Aldrich, 04514TH), sodium hydrosulfide hydrate (NaHS, JT Baker, 02326AH, B25B15), ethylene glycol (EG, JT Baker, G32B27), poly(vinyl pyrrolidone) (PVP, M.W.≈55,000, Sigma-Aldrich, 03817JJ), and chloroauric acid ($HAuCl_4$, Sigma-Aldrich, 55898MJ) were all used as received without further purification. All water used was filtered through a Millipore E-pure filtration system at >18 MΩ cm. Minimum essential media (MEM) was obtained from ATCC (30-2003). Fetal bovine serum (FBS), 3-(4,5-dimethylthiazol-2-yl)-2,5-diphenyl tetrazolium bromide (MTT), and phosphate-buffered saline (PBS) were obtained from Invitrogen. The 50 nm Au nanospheres were obtained from Ted-Pella. Thiolated methoxy polyethylene glycol (mPEG-SH, MW ~5K) was obtained from Laysan Bio.

Synthesis of Ag Nanocubes. The Ag nanocubes used for the synthesis of Au-Ag nanocages for the imaging experiments were synthesized using the sulfide-mediated Ag nanocube synthesis described in Section 2.4. The Ag nanocubes used for the Au-Ag nanocages in the cytotoxicity study were synthesized using a recently reported large-scale reaction based on the decomposition of CF_3COOAg.[34] In the first step, 0.6 mL of a NaHS solution (3 mM in EG) was injected into 50 mL of EG that had been preheated in a 250 mL flask until the temperature of the bath recovered to 150 °C. All the solutions were freshly made during this ~30 min preheat. After 4 min, 5 mL of a HCl solution (3 mM in EG) was added, followed 2 min later by 12.5 mL of a PVP solution (0.35 g/17.5 mL EG), and two more minutes later by 4 mL of a CF_3COOAg solution (282 mM). Upon the final

addition, the solution became reddish-brown in color, which deepened as the nanocubes grew. The size of the nanocubes was monitored using UV-Vis spectroscopy, and the reaction was quenched in an ice bath when the desired size was reached. The nanocubes were then washed once in acetone and twice in water.

Synthesis of Au-Ag Nanocages. In a typical reaction, 1.75 mL of ~1.5 nM Ag nanocubes was added to 20 mL of PVP solution (1 mg/mL in water) that had been preheated to 100 °C. A syringe pump (KD Scientific, Single-Syringe Infusion Pump, cat no. KDS100 230) was then used to inject 0.5 mM $HAuCl_4$ at a rate of 0.75 mL/min until the desired wavelength was reached.[29] The mixture was then refluxed an additional 10 minutes to ensure full reaction. Products were allowed to cool, stirred in saturated NaCl for 1 h to remove any residual AgCl, collected by centrifugation and washed by 3 rounds of centrifugation and re-dispersion in fresh water.

Surface Modification of Au, Ag and Au-Ag Nanostructures. For PVP-coated Ag nanocubes and Au-Ag nanocages, the nanostructures were used as-prepared after the washing steps described above. The Au nanospheres were received with tannic acid coating, which was replaced with PVP by 24 h stirring in a 25 mg/mL PVP solution for 24 h followed by three washes in water. In a typical mPEG conjugation, 0.3 mL of a 1 mM mPEG solution was added to 2.5 mL of a 0.6 nM nanostructure solution, which resulted in a 200,000:1 mPEG:nanostructure ratio (a 10-fold excess based on previous calculations). The products were then collected by centrifugation and washed two times in water. Samples were filtered with a 0.22 μm PES filter and concentrated to 5-10 nM.

Instrumentation. Transmission electron microscopy (TEM) images were captured

with a Tecnai G2 Spirit Twin microscope operated at 120 kV (FEI, Hillsboro, OR). Scanning electron microscopy (SEM) images were captured with a Nova NanoSEM 230 field-emission microscope (FEI, Hillsboro, OR) operated at an accelerating voltage of 15 kV. The sample was prepared by dropping an aqueous suspension of the nanoparticles onto a piece of silicon wafer (for SEM) or carbon coated copper grid (for TEM). The LSPR spectra were recorded using a UV-visible spectrometer (Varian, Cary 50).

Cell Culture. The WI-38 cell line was obtained from ATCC and was cultured in ATCC MEM containing 2 mM L-glutamine, 1 mM sodium pyruvate, non-essential amino acids and 10% FBS under 5% CO_2 at 37 °C.

MTT Assay. WI-38 cells were reseeded 24 h before experiments in 96-well plates at a density of 1.5 E4 cells/well. The following day, the media was removed and replaced with fresh media containing Au, Ag or Au-Ag nanostructures at the desired concentration. After 24 h of incubation, the nanostructure-containing media was removed. Cells were then rinsed once with media under gentle rotation (10 rpm, 4 min). After adding 100 μL of fresh media, 20 μL of MTT solution (5 mg/mL in PBS) was injected into each well. The plates were then briefly shaken (20 rpm, 5 min) and placed into an incubator at 37 °C. After 4 h, the media was removed and the purple crystals from MTT reduction were solubilized with 100 μL of IPA on a shaker (35 rpm, 15 min). To eliminate any optical interference from the nanocages taken up by the cells, 85 μL of this solution was transferred to a fresh 96-well plate before analysis with a microplate reader at a wavelength of 560 nm. P-values were determined with a one-sided ANOVA and Tukey-Kramer multiple comparisons post-tests.

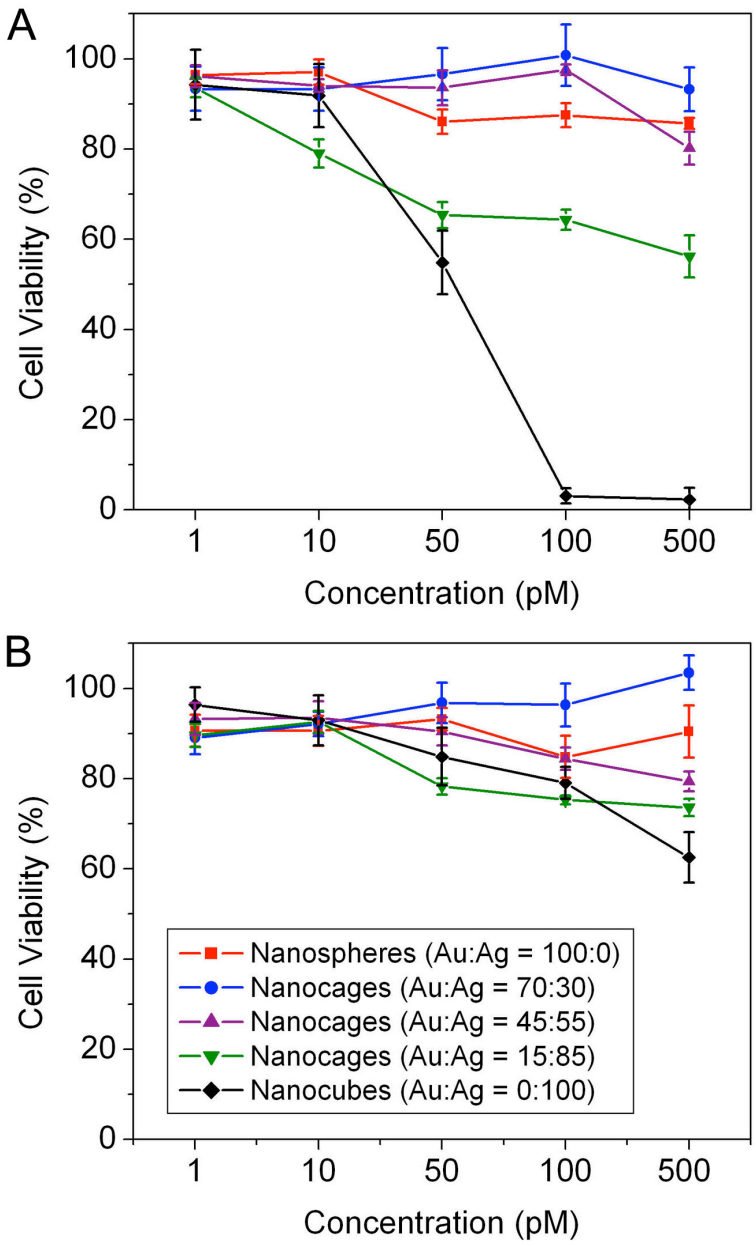

Figure 4.1. Viability of WI-38 fibroblast cells after exposure to ~50 nm nanostructures with different compositions for 24 h, as measured by the MTT assay: (A) nanostructures coated with PVP, and (B) nanostructures coated with 5K mPEG. Error bars indicate the standard deviation (n = 4 for 1-50 pM and n = 3 for 100 and 500 pM).

Au:Ag - Coating	D_{TEM} (nm)	Zeta Potential Before (mV)	Zeta Potential After (mV)
0:100 -PVP	44.0	-26.1	-27.7
15:85 - PVP	44.5	-33.8	-27.1
45:55 - PVP	49.5	-37.0	-22.8
70:30 - PVP	49.8	-30.5	-25.2
100:0 - PVP	48.1	-11.1	-21.2
0:100 - mPEG	44.0	-16.6	-28.0
15:85 - mPEG	44.5	-15.5	-19.7
45:55 - mPEG	49.5	-17.2	-23.7
70:30 - mPEG	49.8	-25.0	-23.6
100:0 - mPEG	48.1	-10.6	-19.6

Table 4.1. Diameters and zeta potentials of Au, Ag, and Au-Ag nanostructures before and after incubation in media. All measurements were performed in 18 mΩ cm water.

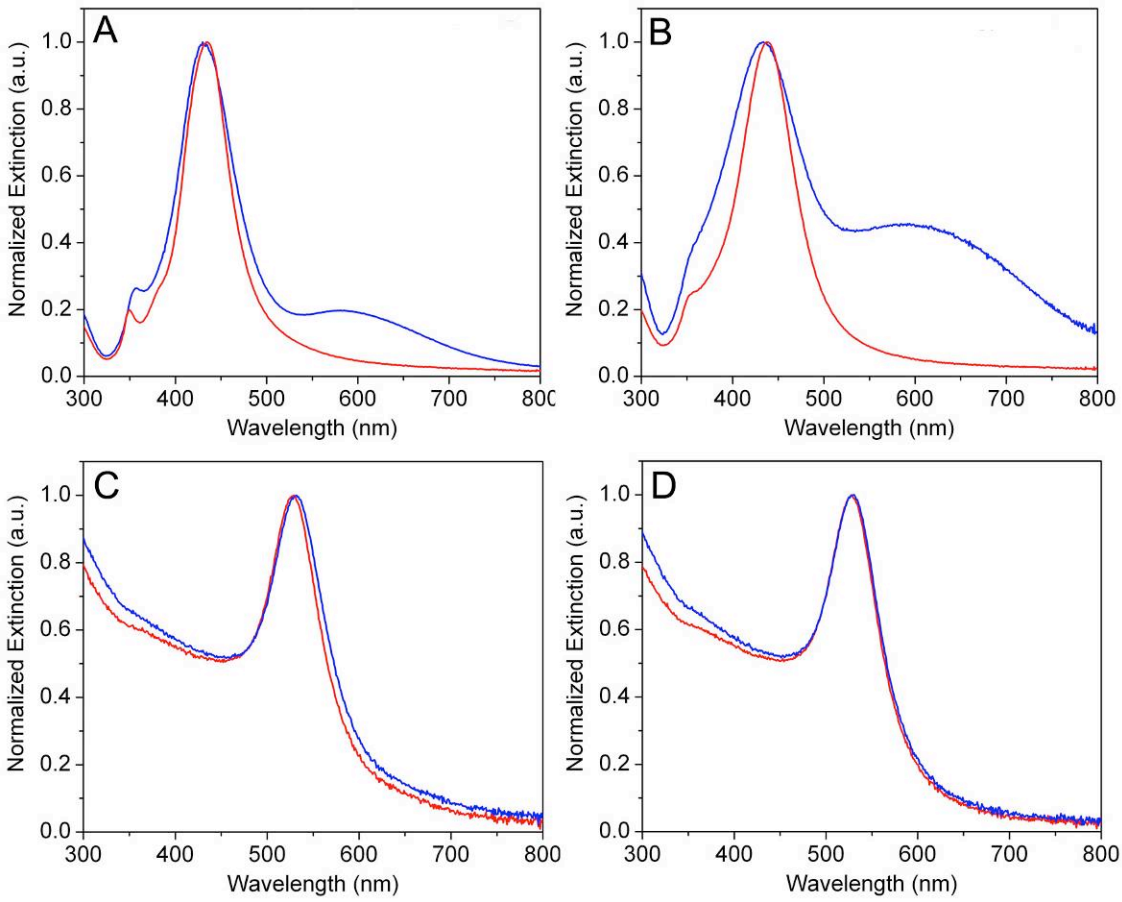

Figure 4.2. LSPR spectra of solid Au and Ag nanostructures before (red) and after (blue) incubation in complete culture media for 24 h. All measurements were performed in 18 mΩ cm water. The compositions (Au:Ag) and surface coatings for each panel are: (A) 0:100 nanocubes-PVP, (B) 0:100 nanocubes-mPEG, (C) 100:0 nanospheres-PVP, (D) 100:0 nanospheres-mPEG.

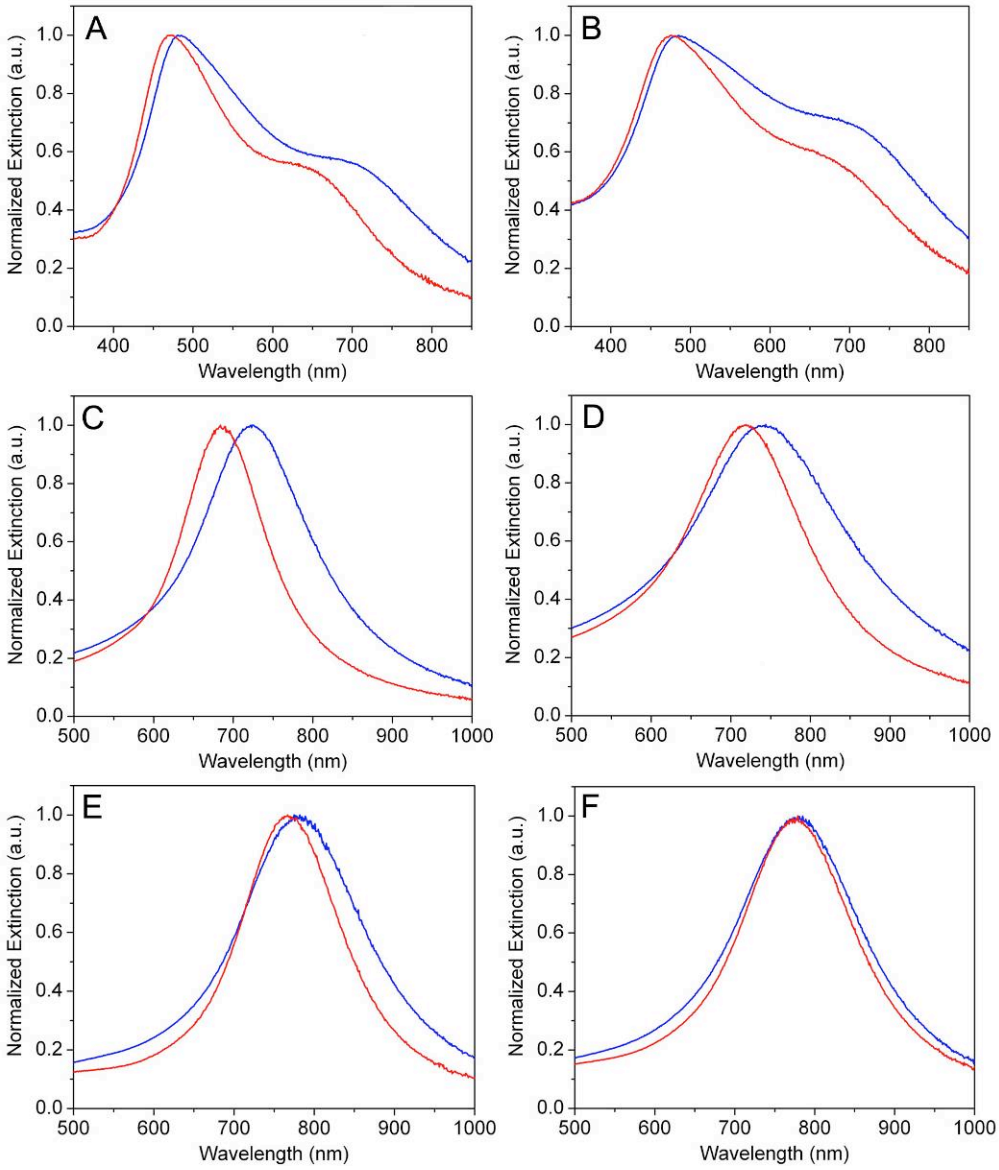

Figure 4.3. LSPR spectra of Au-Ag nanocages before (red) and after (blue) incubation in complete culture media for 24 h. All measurements were performed in 18 mΩ cm water. The compositions (Au:Ag) and surface coatings for each panel are: (A) 15:85-PVP, (B) 15:85-mPEG, (C) 45:55-PVP, (D) 45:55-mPEG, (E) 70:30-PVP, and (F) 70:30-mPEG.

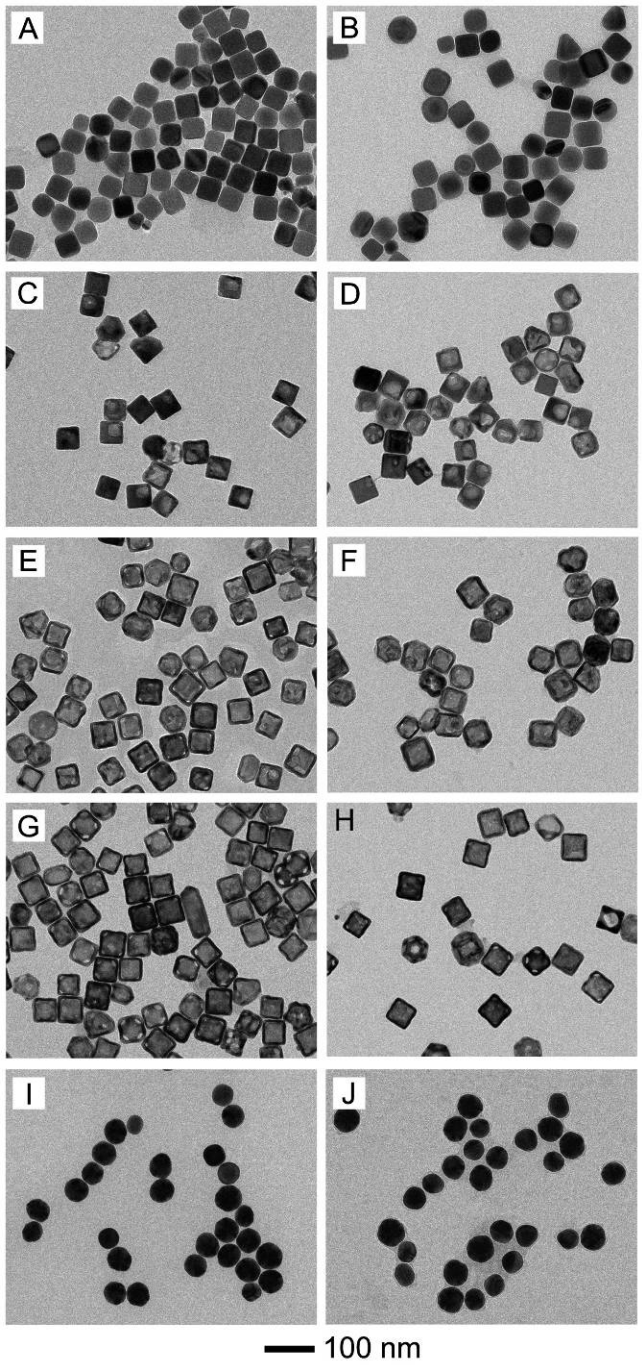

Figure 4.4. TEM images of Au, Ag and Au-Ag nanostructures stabilized with PVP before (A, C, E, G, I) and after (B, D, F, H, J) incubation in culture media for 24 h. The structures had different Au:Ag ratios: (A, B) 0:100 nanocubes, (C, D) 15:85 nanocages, (E, F) 45:55 nanocages, (G, H) 70:30 nanocages, and (I, J) 100:0 nanospheres.

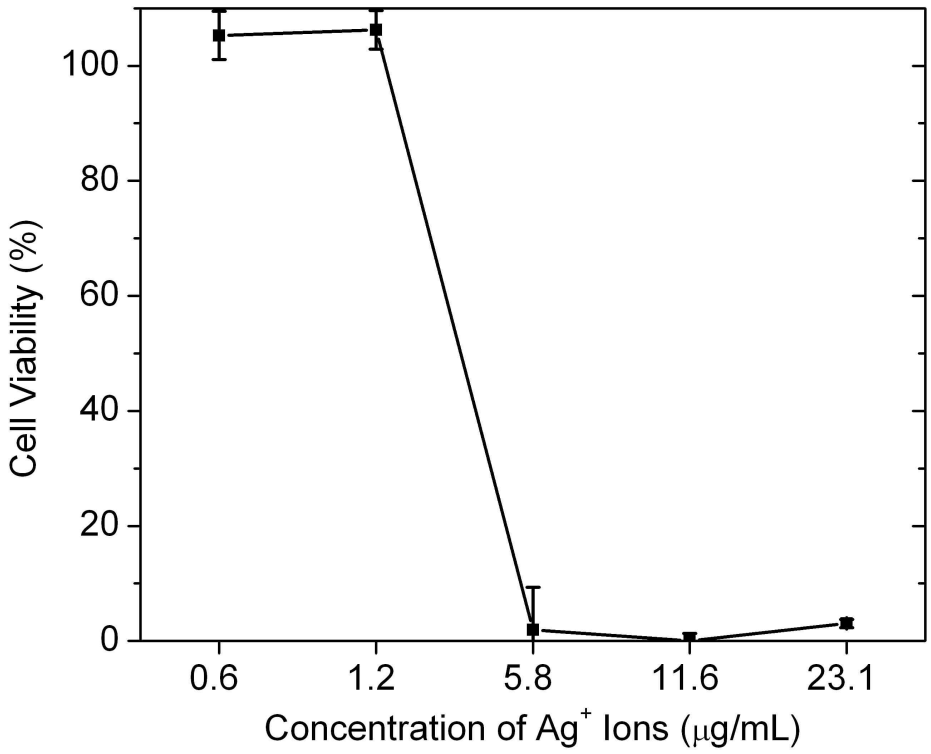

Figure 4.5. Viability of WI-38 fibroblast cells after exposure to different concentrations of $AgNO_3$ for 24 h, as measured by the MTT assay.

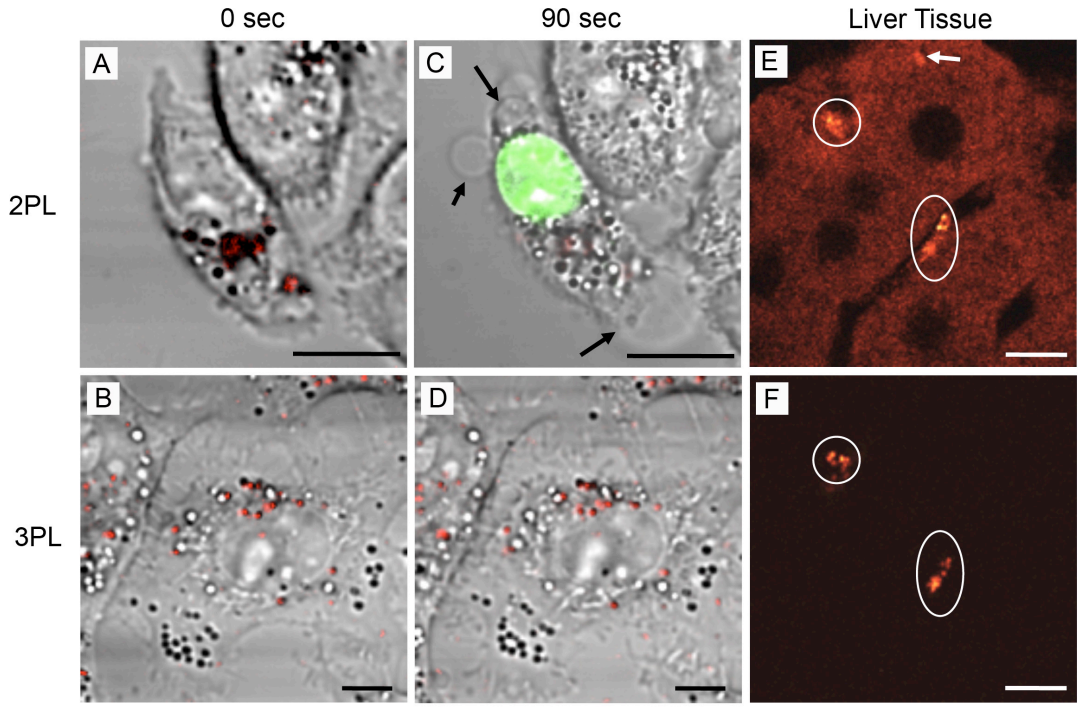

Figure 4.6. Comparison of 2PL and 3PL imaging of Au-Ag nanocages in (A-D) KB cells and (E, F) liver tissues. (A) 2PL image and (B) 3PL image of Au-Ag nanocages (red) in KB cells before laser scanning. (C) Image of the same cell in (A) after scanning with 760-nm fs laser for 90 s. The laser power after objective was 1.9 mW. After scanning, membrane blebbing (arrowed) and compromised membrane integrity indicated by ethidium bromide labeling (green) were observed. (D) 3PL image of the same cell in (B) after scanning with 1,290-nm fs laser for 90 s. The laser power after objective was 4.0 mW. No morphological change or plasma membrane damage was observed. (E) 2PL imaging of Au-Ag nanocages (indicated by white circles) in liver tissue, and (F) 3PL imaging of Au-Ag nanocages (indicated by white circles) in liver tissue from the same area as (E). For both 2PL and 3PL imaging of nanocages in liver, the laser power was 7 mW after objective. Scale bar = 10 μm.

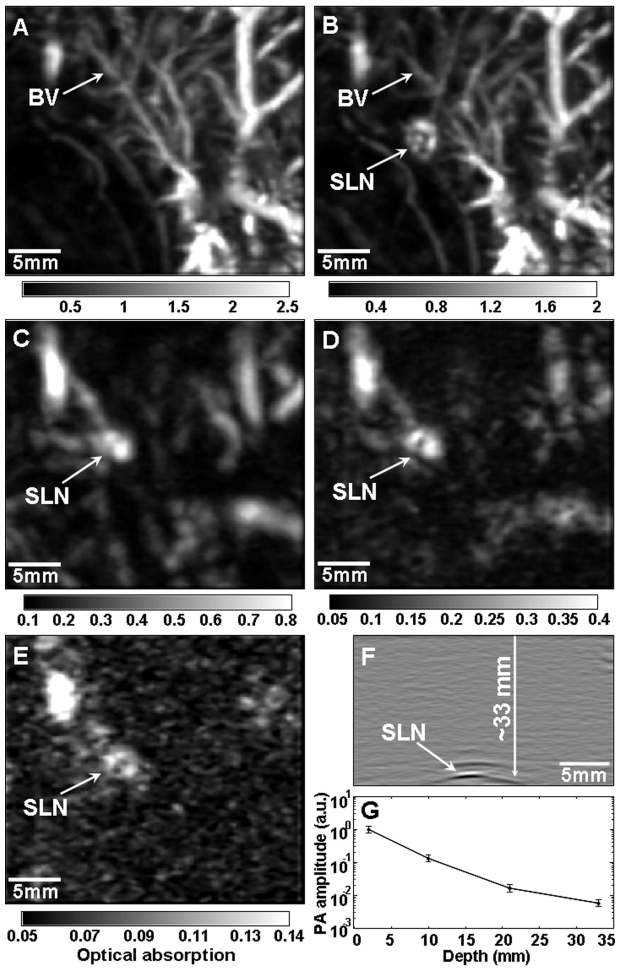

Figure 4.7. Depth capability of sentinel lymph node (SLN) mapping with Au-Ag nanocages for non-invasive *in vivo* breast cancer staging. Photoacoustic images taken (A) before and (B-E) after the injection of nanocages: (A) control image before injection of Au-Ag nanocages; (B) 28 min; (C) 126 min with a layer of chicken breast tissue placed on axillary region (the total imaging depth was 10 mm); (D) 165 min with two layers of chicken breast tissue (the total imaging depth was 21 mm); (E) 226 min with three layers of chicken breast tissue (the total imaging depth was 33 mm). (F) Photoacoustic B-scan with 20 times signal averaging, showing the SLN located 33 mm deep. (G) The amplitude variations of photoacoustic signals over imaging depth. The data were scaled down to 0 dB and normalized by the maximum. Error bar represents standard deviation.

4.6. References for Chapter 4

[1] Ntziachristos, V.; Ripoll, J.; Wang, L.; Weissleder, R. *Nat. Biotechnol.* **2005**, *23*, 313.

[2] Pepperkok, R.; Ellenberg, J. *Nat. Rev. Mol. Cell Biol.* **2006**, *7*, 690.

[3] Skrabalak, S. E.; Chen, J.; Au, L.; Lu, X.; Li, X.; Xia, Y. *Adv. Mater.* **2007**, *19*, 3177.

[4] Murphy, C. J.; Gole, A. M.; Stone, J. W.; Sisco, P. N.; Alkilany, A. M.; Goldsmith, E. C.; Baxter, S. C. *Acc. Chem. Res.* **2008**, *41*, 1721.

[5] Lal, S.; Clare, S. E.; Halas, N. J. *Acc. Chem. Res.* **2008**, *41*, 1842.

[6] Mohamed, M.; Volkov, V.; Link, S.; El-Sayed, M. *Chem. Phys. Lett.* **2000**, *317*, 517.

[7] Chen, J.; Saeki, F.; Wiley, B. J.; Cang, H.; Cobb, M. J.; Li, Z.-Y.; Au, L.; Zhang, H.; Kimmey, M. B.; Li, X.; Xia, Y. *Nano Lett.* **2005**, *5*, 473.

[8] Cho, E.; Kim, C.; Zhou, F.; Cobley, C.; Song, K.; Chen, J.; Li, Z.; Wang, L.; Xia, Y. *J. Phys. Chem. C* **2009**, *113*, 9023.

[9] Oregon Medical Laser Center, O*ptical Absorption of Methylene Blue*, http://omlc.ogi.edu/spectra/mb/index.html.

[10] Song, K. H.; Stein, E. W.; Margenthaler, J. A.; Wang, L. V. *J. Biomed. Opt.* **2008**, *13*, 054033.

[11] Liao, H.; Hafner, J. *Chem. Mater.* **2005**, *17*, 4636.

[12] Chen, J.; Wang, D.; Xi, J.; Au, L.; Siekkinen, A.; Warsen, A.; Li, Z.-Y.; Zhang, H.; Xia, Y.; Li, X. *Nano Lett.* **2007**, *7*, 1318.

[13] Cho, E. C.; Xie, J.; Wurm, P. A.; Xia, Y. *Nano Lett.* **2009**, *9*, 1080.

[14] Alkilany, A. M.; Nagaria, P. K.; Hexel, C. R.; Shaw, T. J.; Murphy, C. J.; Wyatt, M. D. *Small* **2009**, *5*, 701.

[15] Lu, H.; Campbell, C.; Castner, D. *Langmuir* **2000**, *16*, 1711.

[16] Harris, J. M.; Martin, N. E.; Modi, M. *Clin. Pharmacokin.* **2001**, *40*, 539.

[17] Byrne, J. D.; Betancourt, T.; Brannon-Peppas, L. *Adv. Drug. Deliv. Rev.* **2008**, *60*, 1615.

[18] Yavuz, M. S.; Cheng, Y.; Chen, J.; Cobley, C. M.; Zhang, Q.; Rycenga, M.; Xie, J.; Kim, C.; Song, K. H.; Schwartz, A. G.; Wang, L. V.; Xia, Y. *Nat. Mater.* **2009**, *8*, 935.

[19] Paciotti, G.; Kingston, D.; Tamarkin, L. *Drug. Develop. Res.* **2006**, *67*, 47.

[20] Yguerabide, J.; Yguerabide, E. E. *Anal. Biochem.* **1998**, *262*, 157.

[21] Tong, L.; Wei, Q.; Wei, A.; Cheng, J.-X. *Photochem. Photobiol.* **2009**, *85*, 21.

[22] Yu, C.; Nakshatri, H.; Irudayaraj, J. *Nano Lett.* **2007**, *7*, 2300.

[23] Yang, X.; Skrabalak, S. E.; Li, Z.-Y.; Xia, Y.; Wang, L. V. *Nano Lett.* **2007**, *7*, 3798.

[24] Zhang, H. F.; Maslov, K.; Stoica, G.; Wang, L. V. *Nat. Biotechnol.* **2006**, *24*, 848.

[25] Song, K. H.; Wang, L. V. *J. Biomed. Opt.* **2007**, *12*, 060503.

[26] Tong, L.; Cobley, C. M.; Chen, J.; Xia, Y.; Cheng, J.-X. *Angew. Chem. Int. Ed.* **2010**, *49*, 3485.

[27] Au, L.; Zhang, Q.; Cobley, C. M.; Gidding, M.; Schwartz, A. G.; Chen, J.; Xia, Y. *ACS Nano* **2010**, *4*, 35.

[28] Skrabalak, S. E.; Chen, J.; Sun, Y.; Lu, X.; Au, L.; Cobley, C. M.; Xia, Y. *Acc. Chem. Res.* **2008**, *41*, 1587.

[29] Skrabalak, S. E.; Au, L.; Li, X.; Xia, Y. *Nature Protoc.* **2007**, *2*, 2182.

[30] Weissleder, R. *Nat. Biotechnol.* **2001**, *19*, 316.

[31] Hu, M.; Chen, J.; Li, Z.-Y.; Au, L.; Hartland, G. V.; Li, X.; Marquez, M.; Xia, Y. *Chem. Soc. Rev.* **2006**, *35*, 1084.

[32] Chen, J.; Wiley, B. J.; Li, Z.; Campbell, D.; Saeki, F.; Cang, H.; Au, L.; Lee, J.; Li, X.; Xia, Y. *Adv. Mater.* **2005**, *17*, 2255.

[33] Zhang, Q.; Li, W.; Moran, C.; Zeng, J.; Chen, J.; Wen, L.-P.; Xia, Y. *J. Am. Chem. Soc.* **2010**, *132*, 11372.

[34] Zhang, Q.; Li, W.; Wen, L.-P.; Chen, J.; Xia, Y. *Chem.--Eur. J.* **2010**, *16*, 10234.

[35] Zhang, Q.; Cobley, C.; Au, L.; McKiernan, M.; Schwartz, A.; Wen, L.-P.; Chen, J.; Xia, Y. *ACS Appl. Mater. Interfaces* **2009**, *1*, 2044.

[36] Im, S. H.; Lee, Y. T.; Wiley, B. J.; Xia, Y. *Angew. Chem. Int. Ed.* **2005**, *44*, 2154.

[37] Peer, D.; Karp, J. M.; Hong, S.; Farokhzad, O. C.; Margalit, R.; Langer, R. *Nature Nanotech.* **2007**, *2*, 751.

[38] Lewinski, N.; Colvin, V.; Drezek, R. *Small* **2008**, *4*, 26.

[39] Dobrovolskaia, M. A.; McNeil, S. E. *Nat. Nanotechnol.* **2007**, *2*, 469.

[40] Nel, A.; Xia, T.; Mädler, L.; Li, N. *Science* **2006**, *311*, 622.

[41] Cobley, C. M.; Chen, J.; Cho, E. C.; Wang, L. V.; Xia, Y. *Chem. Soc. Rev.* **2010**, ASAP.

[42] Pan, Y.; Leifert, A.; Ruau, D.; Neuss, S.; Bornemann, J.; Schmid, G.; Brandau, W.; Simon, U.; Jahnen-Dechent, W. *Small* **2009**, *5*, 2067.

[43] Paciotti, G. F.; Myer, L.; Weinreich, D.; Goia, D.; Pavel, N.; McLaughlin, R. E.;

Tamarkin, L. *Drug Delivery* **2004**, *11*, 169.

[44] Cytimmune Sciences, Inc. http://www.cytimmune.com/go.cfm?do=Page.View&pid=26

[45] Sherman, A. I.; Ter-Pogossian, M. *Cancer* **1953**, *6*, 1238.

[46] AshaRani, P. V.; Hande, M. P.; Valiyaveettil, S. *BMC Cell Biol.* **2009**, *10*, 65.

[47] Braydich-Stolle, L.; Hussain, S.; Schlager, J.; Hofmann, M. *Toxicol. Sci.* **2005**, *88*, 412.

[48] AshaRani, P. V.; Low Kah Mun, G.; Hande, M. P.; Valiyaveettil, S. *ACS Nano* **2009**, *3*, 279.

[49] Carlson, C.; Hussain, S. M.; Schrand, A. M.; Braydich-Stolle, L. K.; Hess, K. L.; Jones, R. L.; Schlager, J. J. *J. Phys. Chem. B* **2008**, *112*, 13608.

[50] Li, T.; Albee, B.; Alemayehu, M.; Diaz, R.; Ingham, L.; Kamal, S.; Rodriguez, M.; Bishnoi, S. W. *Anal. Bioanal. Chem.* **2010**, *398*, 689.

[51] Diehl, K.; Hull, R.; Morton, D.; Pfister, R.; Rabemampianina, Y.; Smith, D.; Vidal, J.; van de Vorstenbosch, C. *J. Appl. Toxicol.* **2001**, *21*, 15.

[52] International Commission on Radiation Units Measurements. *Photon, electron, proton, and neutron interaction data for body tissues*; International Commission on Radiation Units and Measurements, 1992.

[53] Goodman, C. M.; McCusker, C. D.; Yilmaz, T.; Rotello, V. M. *Bioconjug. Chem.* **2004**, *15*, 897.

[54] Lin, J.; Zhang, H.; Chen, Z.; Zheng, Y. *ACS Nano* **2010**, *4*, 5421.

[55] Cho, E. C.; Au, L.; Zhang, Q.; Xia, Y. *Small* **2010**, *6*, 517.

[56] Verma, A.; Stellacci, F. *Small* **2010**, *6*, 12.

[57] Kelly, K.; Coronado, E.; Zhao, L.; Schatz, G. C. *J. Phys. Chem. B* **2003**, *107*, 668.

[58] Willets, K. A.; Van Duyne, R. P. *Ann. Rev. Phys. Chem.* **2007**, *58*, 267.

[59] Halas, N. J. *MRS Bull.* **2005**, *30*, 362.

[60] Kittler, S.; Greulich, C.; Diendorf, J.; Köller, M.; Epple, M. *Chem. Mater.* **2010**, *22*, 4548.

[61] Helmchen, F.; Denk, W. *Nat. Methods* **2005**, *2*, 932.

[62] Park, J.; Estrada, A.; Sharp, K.; Sang, K.; Schwartz, J. A.; Smith, D. K.; Coleman, C.; Payne, J. D.; Korgel, B. A.; Dunn, A. K.; Tunnell, J. W. *Opt. Express* **2008**, *16*, 1590.

[63] Kim, C.; Cho, E. C.; Chen, J.; Song, K. H.; Au, L.; Favazza, C.; Zhang, Q.; Cobley, C. M.; Gao, F.; Xia, Y.; Wang, L. V. *ACS Nano* **2010**, *4*, 4559.

[64] Song, K. H.; Kim, C.; Cobley, C. M.; Xia, Y.; Wang, L. V. *Nano Lett.* **2009**, *9*, 183.

[65] Wang, L. V. *Med. Phys.* **2008**, *35*, 5758.

Chapter 5

Conclusion

In this work, I have demonstrated that plasmonic nanostructures made of Au, Ag, and alloys of these two noble metals can be engineered for applications in SERS and biomedical imaging through careful control of their morphologies, compositions, and surface coatings.

By controlling the amount of etching during a reaction, I have demonstrated routes to direct the growth of solid Ag nanocrystals into well-defined geometries, including both non-centrosymmetric shapes such as asymmetrically truncated octahedrons, and highly isotropic shapes such as spheres. The morphological changes occurring during these reactions led to interesting changes in the LSPR properties of the structures, in part due to the presence or absence of sharp features.

These morphologies were also useful for fundamental SERS studies, as they made it possible to probe the effect of symmetry and rounding on the SERS enhancement. By comparing the SERS enhancement of asymmetrically truncated octahedrons and standard octahedrons, I found that the asymmetrical shape had a minimal effect on the SERS enhancement. Fellow group members have also recently taken advantage of the large nanospheres produced using the etching method presented in this work to study the SERS enhancements of single nanospheres and nanosphere dimers. It would be interesting in

future work to investigate how the influence of sharp features on LSPR-based properties affects other phenomena that don't have the E^4 dependence of SERS, such as photoacoustic imaging with a E^1 dependence and two-photon luminescence with a E^2 dependence.

Furthermore, by harnessing other corrosive forces such as galvanic replacement, it is possible to create nanostructures with tunable LSPR resonances, compositions, and morphologies. I have shown in this work that the packing of atoms on the surface, the electrochemical potentials of the precursor, and the order multiple precursors are added are added can all have strong influences on the final product.

Finally, plasmonic nanostructures also have many interesting biomedical applications. In the first part of my work in this area, I examined the cytotoxicity of Ag, Au and Au-Ag nanostructures with different Au:Ag ratios and found that only a small amount of Au needed to be incorporated to induce a significant decrease in the cytotoxicity compared to pure Ag nanostructures. I also found that the cell viability could be improved by coating the nanostructures with PEG and that the observed cytotoxicity of Ag nanocubes was in line with what would be expected from Ag^+ dissolution. However, it would be interesting to also examine other potential sources of cytotoxicity, such as increased ROS production, and see if any of the nanostructures studied have less immediately visible, but still damaging effects such as genotoxicity. Next, I looked at two ways that Au-Ag nanocages can enhance biomedical imaging: as *in vitro* probes through 3PL, and as contrast agents for *in vivo* photoacoustic imaging of sentinel lymph nodes. Both these studies used non-targeted nanocages, but to make these

techniques even more powerful it would be interesting to add targeting groups to the surface. This general concept has already been demonstrated for 2PL imaging and photoacoustic imaging of melanomas with nanocages, however in future work it would be interesting to use targeted nanocages for sentinel lymph node mapping. Targeting would be especially interesting for this application if the appropriately modified nanocages could provide enough of an increase in contrast compared to non-targeted nanocages to determine if cancer had spread to the lymph nodes without taking a sample for biopsy.